Politecnico di Milano
Dipartimento di Matematica

Ph.D. programme in
Mathematical Models and Methods in Engineering

Topology Optimization: Advanced Techniques for New Challenges

Candidate:
Nicola Ferro

Advisors:
Prof. Stefano Micheletti
Prof. Simona Perotto

Chair of The Doctoral Program:
Prof. Irene Sabadini

XXXI cycle

Contents

List of Figures

List of Tables

Abstract

In this work, some advanced numerical techniques are employed to address the topology optimization problem from both a modeling and an algorithmic perspective. In both cases, we exploit a recent algorithm, which couples a standard density-based topology optimization formulation with an anisotropic mesh adaptation procedure, named SIMPATY.
Concerning modeling, the goal pursued is to enhance standard methods for the optimization of structures at both the macro- and micro-scales. At the macro-scale, we propose an innovative structural optimization method whose strong point is the sequential combination of shape and topology optimization. The first optimization is a standard geometric shape optimization, whereas the topology optimization resorts to the SIMPATY algorithm. The resulting layouts are characterized by smooth and sharp void/material interfaces besides exhibiting good mechanical performances, namely lightness and stiffness. Additionally, anisotropic mesh adaptation allows us to design structures intrinsically exhibiting free-form features. The same topology optimization strategy is then employed to devise optimal microstructures enjoying extremal macroscopic mechanical properties. The mathematical setting adopted in such context is the inverse homogenization method based on topology optimization.
From an algorithmic viewpoint, we focus on the reduction of the computational burden typical of topology optimization. The offline/online paradigm of a POD approach is exploited to reach this goal. In particular, the POD procedure predicts a layout successively corrected with SIMPATY algorithm, following a predictor/corrector approach. This device reduces the iterations demanded to converge, while guaranteeing the desired mechanical performances.

Keywords: Finite Elements, Topology Optimization, Shape Optimization, Homogenization, Anisotropic Mesh Adaptation, Proper Orthogonal Decomposition.

Sommario

In questo lavoro, vengono presentate tecniche numeriche avanzate nell'ambito dell'ottimizzazione topologica, sia da un punto di vista modellistico che computazionale. In entrambi i casi, si ricorre all'algoritmo SIMPATY, di recente implementazione, che accoppia una formulazione standard per l'ottimizzazione topologica con una tecnica di adattazione anisotropa di mesh. Riguardo gli aspetti modellistici, ci si è proposti di migliorare i metodi comunemente impiegati per l'ottimizzazione strutturale sia alla macro- che alla micro-scala. Alla macro-scala, è stato proposto un algoritmo che combina sequenzialmente ottimizzazione di forma e topologica. Nel caso dell'ottimizzazione di forma, si è utilizzata una formulazione classica, mentre, per l'ottimizzazione della topologia della struttura, ci si è serviti dell'algoritmo SIMPATY. Le strutture risultanti sono caratterizzate da interfacce vuoto/materiale ben definite e dalle prestazioni meccaniche attese, quali la leggerezza e la rigidezza. Inoltre, l'adattazione anisotropa di mesh favorisce il design di strutture intrinsecamente *free-form*. La medesima strategia di ottimizzazione topologica è stata inoltre impiegata per la progettazione di microstrutture ottimali, caratterizzate da proprietà meccaniche macroscopiche d'interesse. In tale ambito viene sfruttato il metodo di omogeneizzazione inversa in un contesto di ottimizzazione topologica standard.
Da un punto di vista computazionale, si è cercato di abbattere l'onere computazionale tipico delle tecniche standard di ottimizzazione topologica. A tal fine si è utilizzato un approccio di tipo POD al fine di progettare una struttura dal design ottimizzato, ad un costo computazionale ridotto. In particolare, si è riusciti a contenere il numero delle iterazioni richieste per la convergenza dell'ottimizzazione, pur preservando le proprietà meccaniche richieste.

Introduction

Structural optimization is a research field of large interest and great impact in the community that relies on mathematical methods for the optimal design of structures. Following a standard classification, we distinguish structural optimization in size, shape, and topology optimization. Such techniques have been gaining momentum due to their massive employment for the design by means of new, sophisticated tools, as 3D printing and additive manufacturing (AM). Several fields of application are involved by these new production processes. For instance, automotive and aerospace companies are investing in 3D printing and AM for different design purposes (e.g., design of lightweight and performant components). Other areas of application include architecture, design, fashion and jewelry which are exploring 3D printing and AM to customize and manufacture original and unique pieces. Moreover, 3D printing is currently one of the cheapest techniques employed for rapid prototyping. In fact, due to the velocity characterizing the process and the contained cost of certain materials (e.g., plastics), it is possible to test several different designs and quickly verify how they perform when manufactured.

In practice, unlike subtractive methods, additive manufacturing consists in the assembly of structures by the deposition (or the melting) of material layer by layer. Additive techniques impact also on the design phase, since they allow to manufacture free-form structures, characterized by weaker geometric constraints with respect to the ones typical of subtractive procedures. Virtually all the shapes, even the most complex, can be manufactured, blazing the trail for a novel, free-form design paradigm. Nevertheless, 3D printing and AM are not immune from some issues, e.g., the choice of the optimal orientation for the printing process, the use of supports in the production phase, the presence of inhomogeneities in the printed material derived by the incomplete melting of the powder (as in a laser-based process), just to name a few. These issues are beyond the goals of this thesis and we focus on

the reduction of the computational effort demanded in the design phase as well as on the enhancement of mechanical properties and geometric features.

In particular, we will address the optimal design problem by means of shape optimization and topology optimization. Shape optimization allows to modify the shape of a given structure to meet prescribed constraints, and to minimize/maximize an objective function related to a mechanical performance, such as the structure compliance or the maximum frequency of vibration. Topology optimization seeks the optimal distribution of material inside an initial design domain by changing the topology, without moving the outer structure boundary. The original contributions of this thesis are collected in Chapters $2-4$ from scientific papers and are currently published in or submitted to international peer-reviewed journals.

In **Chapter 1**, the mathematical background used throughout the thesis is presented and discussed. In particular, we introduce the standard topology optimization techniques and the advanced mathematical methods used to enhance the classical formulation.

Chapter 2 deals with the coupling of a shape optimization procedure with an adaptive algorithm for topology optimization (SIMPATY) enriched with anisotropic mesh adaptation.

Chapter 3 addresses the application of SIMPATY algorithm to the optimal design of microstructures constituting the elementary cell of a metamaterial, resorting to an inverse homogenization technique.

Chapter 4 presents a model order reduction technique, specifically the Proper Orthogonal Decomposition, to contain the computational burden related to standard structural topology optimization.

Finally, we draw some conclusions of this work and we highlight some possible future perspectives in a last section.

1 The skeleton

1.1 New challenges

The development of new manufacturing techniques and the enhancement of existing ones have been encouraging a new interest in the design and redesign of structures, with a view to their improvement [17, 36, 75]. The challenges that we want to tackle with the proposal of some advanced mathematical techniques are related to applications that have arisen from industrial and academic partners. In particular, the proposed methods address different issues in the structural optimization framework. Our aim is to handle realistic configurations, characterized by complex setting and load conditions, in a reliable, efficient, and performant way. This means that the final outcome of structural optimization should be reliable from a mechanical viewpoint, and possibly delivered in a short time.

The collaboration with Thales Alenia Space The industrial research stems from the collaboration established during the 3-year Ph.D. program between Politecnico di Milano and Thales Alenia Space Italia (TAS in short), a space company in Italy, with the goal to optimize satellite components. The specific problem that they proposed was challenging: i) the geometry is a 3D realistic configuration; ii) a large number of design constraints is needed to enforce the manufacturabilty of the optimized component; and

iii) the applied loads modeling the physical system simulate the load condition in the launch event. Such problem can be of course studied with simulation tools already present in the market, but they require expertise and high performing computers, along with some trust, since commercial software usually works as a black box. In this context, we refer to one of the most commonly adopted software, namely Altair Hyperworks, a suite for multiphysics simulations endowed with an automatic tool for topology optimization (https://altairhyperworks.com/hw2017/). This software makes the setting of a complex problem rather easy, but the numerical simulations require a large computational power. Figure 1.1 shows the setting of the problem and the output of the topology optimization of a satellite component. The design domain presents a T-shaped structure which is intended to accommodate 3 gyroscopes on the external surfaces. The 8 red parallelepipeds are clamped and they do not undergo any optimization, while an equivalent load is applied to the barycenter of the structure. The simulation is run with the commercial software Altair Hyperworks using a common laptop.

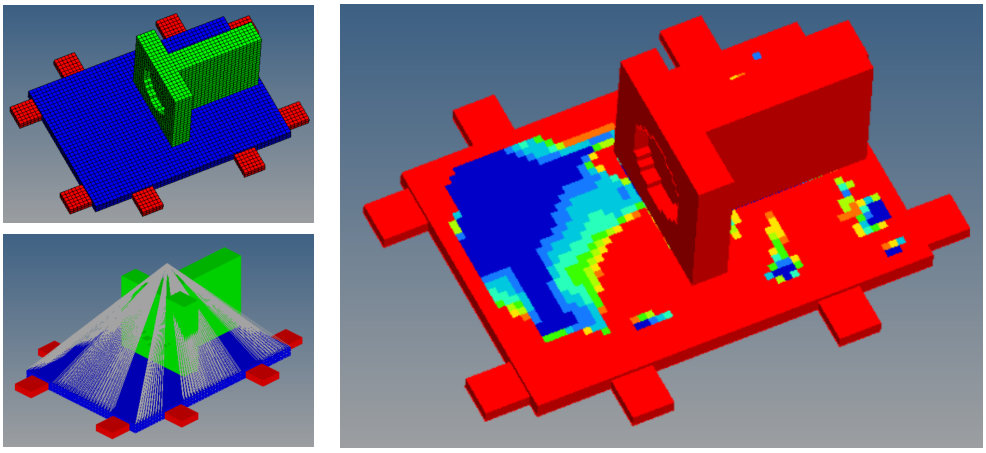

Figure 1.1: The satellite component under investigation with Altair Hyperworks: the geometry (top-left), the loads with the application point (bottom-left), and the optimized result (right).

It is evident that the result needs a massive post-processing before the final structure is sent to the production phase. For this reason, TAS asked for a comparison between the output provided by the commercial software

and the one obtained with the innovative techniques developed in this thesis. We refer to Section 1.4 to show the innovative solutions that we have devised.

The METAMAT laboratory The creation of an interdisciplinary laboratory at Politecnico di Milano, the METAMAT Lab on metamaterials, prompted a new research line. In particular, mechanical and chemistry engineer partners raised the need of designing new microstructures to be exploited in different fields. Several dedicated works are present in the literature (see e.g., [41, 45]) and concern the study of microstructures extensively employed in applications (see Figure 1.2).

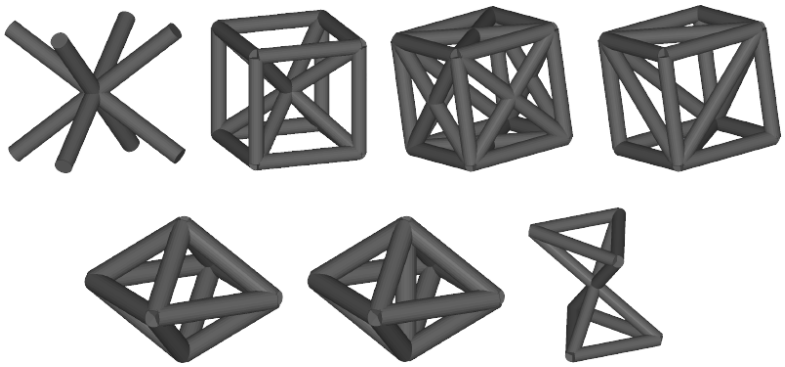

Figure 1.2: Some geometries for structures currently employed and studied in the literature: BCC cell, f2-BCC cell, f2-FCC cell, f2-FCC-L cell (top, left-right); pyramidal cell, pyramidal-Z cell, Kagomè cell (bottom, left-right). Courtesy of E. Marranchino.

The new approach that we suggested was to employ advanced mathematical techniques to address the design of new and original optimized microstructures able to guarantee prescribed properties. The ultimate purpose is to theoretically investigate the performances of these microcells under a mechanical viewpoint and employ them for the design and the production phases.

The roadmap The original contributions presented in the thesis consist in the application of different mathematical models and techniques to structural optimization. We first provide the classic mathematical background for topology optimization. In particular, Section 1.2 is devoted to the SIMP

method and the minimum compliance problem. Section 1.3 introduces the advanced techniques that will be used for enhancing the standard approaches. Section 1.3.1 deals with the mesh adaptation technique with details on the error estimation procedure and the anisotropic framework. Successively, in Section 1.3.2, the homogenization theory is presented and the background for the topology optimization problem at the microscale is set. Section 1.3.3 is extensively dedicated to the Proper Orthogonal Decomposition method for model order reduction, and, finally, the last section collects the results obtained for the industrial and academic challenges introduced so far.

1.2 Standard techniques for topology optimization

We refer to topology optimization (TO) as the technique dealing with the optimal allocation of material in a design domain, so that a certain quantity of interest characterizing a physical system is optimized subject to prescribed requirements. The constraints are related to design specifications (e.g., the volume fraction in the final configuration, a local control over the maximum/minimum displacement or stress) and are usually expressed as equalities or inequalities, whereas a PDE models the underlying physical system. Concerning the quantity of interest, typical examples are the minimization of the compliance and the maximization of the fundamental vibration frequency.

From a mathematical viewpoint, the arrangement of void and solid should be represented by a two-valued function which determines if a certain point of the design domain is occupied by material or by void [14]. Nevertheless, this kind of binary formulation is very demanding in view of numerical simulations and the optimization problem that arises can be classified as a mixed-integer programming problem which is not computationally affordable for realistic configurations. For these reasons, the integer form of topology optimization has been relaxed and different techniques relying on a continuous variable have been employed, although mimicking a binary allocation of material [66, 74]. Such variable is generally referred to as the design variable and takes a different meaning according to the selected method. The first methods introduced in the literature exploit the homogenization theory [2, 6, 13, 29, 51, 52, 53, 55, 63, 64]. As an alternative, many authors consider the

SIMP (Solid Isotropic Material with Penalization) method as the reference method for TO. According to this approach, the design variable is the density ρ that takes value between 0 and 1, where 0 is associated with void and 1 with the material [11, 12, 14, 15]. Similarly, the phase field formulation exploits a density variable taking value in $[0, 1]$ whose intermediate values are penalized via an integral term (e.g., see [19, 24, 79, 80]). The level set method introduces a signed distance function, in order to track the contour of the interface between void and solid regions in the design domain. The evolution of this variable is guided by a time dependent equation with a driving force represented by the topological derivative of the objective functional [3, 5, 7, 22, 23, 26]. All these mathematical models have been largely investigated and sometimes enriched in order to deal with non-standard numerical discretizations. For instance, XFEM and CutFEM have been used to enhance the resolution of the void-material interface [25, 37, 61, 78].

Independently of the model chosen for topology optimization, the general form of a TO problem can be cast in the following framework

find $\chi \in X(\Omega)$ such that

$$\min_{\chi \in X(\Omega)} \mathcal{J}(w(\chi)) \ : \begin{cases} \mathcal{S}(w(\chi)) = 0 \quad w \in S \\ + \\ \text{design constraints,} \end{cases} \tag{1.1}$$

where χ is the generic design variable chosen in a suitable function space $X(\Omega)$, $\mathcal{J}$ is the objective functional to be minimized, $w \in S$ is the state variable, and $\mathcal{S}$ represents the PDE state equation modeling the physical system.

1.2.1 The minimum compliance problem for structural optimization

Throughout this thesis, we will focus on the topology optimization problem modeled via the SIMP method [15]. In particular, major attention will be devoted to the minimum compliance problem in the linear elastic setting, so as to find the stiffest structure that meets the imposed constraints. Such problem has been extensively investigated in the literature and for the practical implications is considered of great impact also for industrial applications [4, 15, 76, 81]. In more detail, we seek the optimal structure, inside the design domain $\Omega \subset \mathbb{R}^d, d = 2, 3$, minimizing the static compliance under assigned

constraints and loads. A traction $\mathbf{f} : \Gamma_N \to \mathbb{R}^d$ is applied to a portion Γ_N of the boundary, $\partial\Omega$, of the structure. Hence, the compliance is given by

$$\mathcal{G}(\mathbf{u}) = \int_{\Gamma_N} \mathbf{f} \cdot \mathbf{u}\, d\gamma,$$

where $\mathbf{u} = (u_1, \ldots, u_d)^T : \Omega \to \mathbb{R}^d$ is the displacement field. The compliance $\mathcal{G}$ coincides with the work done by the traction and the minimization of such quantity is equivalent to the maximization of the stiffness of the structure.

The state equation is represented by the linear elasticity equation [43]

$$\begin{cases} -\nabla \cdot \sigma(\mathbf{u}) = \mathbf{0} & \text{in } \Omega \\ \mathbf{u} = \mathbf{0} & \text{on } \Gamma_D \\ \sigma(\mathbf{u})\mathbf{n} = \mathbf{f} & \text{on } \Gamma_N \\ \sigma(\mathbf{u})\mathbf{n} = \mathbf{0} & \text{on } \Gamma_F, \end{cases} \tag{1.2}$$

where $\sigma(\mathbf{u}) = 2\mu\varepsilon(\mathbf{u}) + \lambda I : \varepsilon(\mathbf{u})$ represents the Hooke's law relating displacement and stress tensor for an isotropic material, with $\varepsilon(\mathbf{u}) = \left(\nabla\mathbf{u} + (\nabla\mathbf{u})^T\right)/2$ the small displacement strain tensor, where

$$\lambda = \frac{E\nu}{(1+\nu)(1-2\nu)}, \quad \mu = \frac{E}{2(1+\nu)}$$

are the Lamé coefficients, with E the Young modulus, ν the Poisson ratio of the material, I is the identity tensor, $\mathbf{n}$ is the unit outward normal vector to $\partial\Omega$, Γ_D is the portion of the boundary where homogeneous Dirichlet conditions are imposed (i.e., where Ω is clamped), and Γ_F is the normal stress-free boundary, so that $\Gamma_D \cup \Gamma_N \cup \Gamma_F = \partial\Omega$.

With a view to numerical simulations, we consider the weak form of system (1.2),

find $\mathbf{u} \in U = \{\mathbf{v} \in [H^1(\Omega)]^d \ : \ \mathbf{v} = \mathbf{0} \text{ on } \Gamma_D\}$, such that

$$a(\mathbf{u}, \mathbf{v}) = \mathcal{G}(\mathbf{v}) \quad \forall \mathbf{v} \in U, \tag{1.3}$$

with

$$a(\mathbf{u}, \mathbf{v}) = \int_\Omega \sigma(\mathbf{u}) : \varepsilon(\mathbf{v})\, d\Omega, \quad \mathcal{G}(\mathbf{v}) = \int_{\Gamma_N} \mathbf{f} \cdot \mathbf{v}\, d\gamma.$$

SIMP method employs the density variable ρ to identify the material distribution in the design domain Ω. Specifically, the design function $\rho \in$

$L^\infty(\Omega,[0,1])$ determines the optimal topology by means of the extremal values, namely $\rho = 0$ corresponding to void, and $\rho = 1$ for the full material. To avoid intermediate values in $[0,1]$, a power law penalization function ρ^p, with $p \geq \max\left\{2/(1-\nu), 4/(1+\nu)\right\}$ is introduced [8, 15].

In the minimum compliance framework, the state equation (1.3) is properly modified by replacing the Lamé coefficients λ and μ with $\rho^p\lambda$ and $\rho^p\mu$, respectively. Thus, the weak form of the state equation for the SIMP formulation is

find $\mathbf{u} \in U$ such that

$$a_\rho(\mathbf{u},\mathbf{v}) = \mathcal{G}(\mathbf{v}) \quad \forall \mathbf{v} \in U, \tag{1.4}$$

with

$$a_\rho(\mathbf{u},\mathbf{v}) = \int_\Omega \sigma_\rho(\mathbf{u}) : \varepsilon(\mathbf{v})\, d\Omega,$$

$\sigma_\rho(\mathbf{u}) = \rho^p\left[2\mu\varepsilon(\mathbf{u}) + \lambda I : \varepsilon(\mathbf{u})\right]$ being a modification of Hooke's law.
The SIMP method is thus defined

find $\rho \in L^\infty(\Omega)$ such that

$$\min_{\rho\in L^\infty(\Omega)} \mathcal{G}(\mathbf{u}(\rho)) \ : \begin{cases} a_\rho(\mathbf{u}(\rho),\mathbf{v}) = \mathcal{G}(\mathbf{v}) \ \forall \mathbf{v} \in U \\ \int_\Omega \rho\, d\Omega \leq \alpha|\Omega| \\ \rho_{\min} \leq \rho \leq 1, \end{cases} \tag{1.5}$$

where $0 < \alpha < 1$ denotes the maximum volume fraction of the optimized configuration; $0 < \rho_{\min} < 1$ is a lower bound for the density employed to guarantee the well-posedness of the state equation, now depending on ρ.

A common practice to numerically solve (1.5) consists in resorting to a standard finite element discretization. In particular, we introduce V_h^r the space of the finite elements of degree r associated with a conforming tessellation $\mathcal{T}_h = \{K\}$ of Ω, K being the generic element, and h the grid spacing [21]. The optimization problem (1.5) in a discrete setting is

find $\rho_h \in V_h^r$ such that

$$\min_{\rho_h\in V_h^r} \mathcal{G}(\mathbf{u}_h(\rho_h)) \ : \begin{cases} a_\rho(\mathbf{u}_h(\rho_h),\mathbf{v}_h) = \mathcal{G}(\mathbf{v}_h) \ \forall \mathbf{v}_h \in U_h^s \\ \int_\Omega \rho_h\, d\Omega \leq \alpha|\Omega| \\ \rho_{\min} \leq \rho_h \leq 1, \end{cases} \tag{1.6}$$

with $\mathbf{u}_h(\rho_h) \in U_h^s$ the finite element approximation for the displacement, U_h^s being the finite element space of vector-valued functions of degree s.

We remark that structural optimization problems and especially the TO model presented are non-convex problems and may be characterized by multiple local minima. For this reason, we refer to the results with the adjective *optimized* in contrast with *optimal*, which should be used only when the global optimum is reached. As a consequence, problem (1.6) also suffers from numerical issues. Namely, the problem is mesh dependent, meaning that different configurations arise from the choice of different spatial discretizations. Moreover, the final result can be characterized by non-manufacturable components where the material regions are poorly connected; such phenomenon is known as checkerboard effect [15, 28, 71]. Several remedies have been proposed to contain these drawbacks, mainly related to the use of filtering techniques to smooth, sharpen, or connect the density arrangement [20, 44, 46, 54, 70]. Concerning the checkerboard effect, it has also been suggested to employ different polynomial degrees for the discretization of ρ_h and $\mathbf{u}_h$, i.e., $s \geq r$ [71].

The usual way to address the numerical optimization problem is to employ gradient-based routines. In this case, one should supply the chosen algorithm with the derivative of the objective functional $\mathcal{G}(\mathbf{u}(\rho))$ with respect to the design variable ρ. For this purpose, we resort to a standard Lagrangian approach [16]. According to this procedure, we define the Lagrangian functional that considers the objective functional $\mathcal{G}$ together with the state equation constraining the physical system

$$\mathcal{L} = \mathcal{L}(\mathbf{u}, \mathbf{z}, \rho) = \mathcal{G}(\mathbf{u}) + a_\rho(\mathbf{u}, \mathbf{z}) - \mathcal{G}(\mathbf{z}),$$

where $\mathbf{z} \in U$ is the Lagrange multiplier, also referred to as the dual or adjoint variable. Finally, the gradient of the compliance $\nabla_\rho \mathcal{G}(\rho)$ is defined as

$$\nabla_\rho \mathcal{G}(\mathbf{u}(\rho)) = \nabla_\rho \mathcal{L}\big|_{\mathbf{u}(\rho),\mathbf{z}(\rho),\rho},$$

where $\mathbf{u}(\rho)$ is the solution to the primal problem obtained via the Gâteaux differentiation of $\mathcal{L}$ with respect to $\mathbf{z}$. In the same way, by employing the Gâteaux derivative of $\mathcal{L}$ with respect to $\mathbf{u}$, we obtain the equation for $\mathbf{z}(\rho)$. It is easy to verify that the primal problem coincides with (1.4), and the adjoint problem reads

find $\mathbf{z} \in U$ such that

$$a_\rho(\mathbf{v}, \mathbf{z}) = -\mathcal{G}(\mathbf{v}) \quad \forall \mathbf{v} \in U. \tag{1.7}$$

Thanks to the self-adjointness of the bilinear form $a_\rho(\cdot,\cdot)$, we infer that $\mathbf{z} = -\mathbf{u}$. The computation of $\nabla_\rho \mathcal{G}(\mathbf{u}(\rho))$ requires the Gâteaux derivative of $\mathcal{L}$ with respect to ρ along the direction $\psi \in U$ to obtain

$$\langle \nabla_\rho \mathcal{G}, \psi \rangle = \int_\Omega p\, \rho^{p-1} \sigma(\mathbf{u}) : \varepsilon(\mathbf{z}) \psi \, d\Omega,$$

implying

$$\nabla_\rho \mathcal{G}(\mathbf{u}(\rho)) = -p\, \rho^{p-1} \sigma(\mathbf{u}(\rho)) : \varepsilon(\mathbf{u}(\rho)), \tag{1.8}$$

where the relation between $\mathbf{z}$ and $\mathbf{u}$ has been exploited.

The gradient thus computed can be employed to drive a gradient-descent algorithm to solve problem (1.5) [39, 40]. In particular, several available software libraries for optimization efficiently employ this kind of algorithm. Nevertheless, these methods manage to find local minima and do not guarantee any global optimum property. Thus, other methods are employed, such as non-gradient approaches [60, 73] or continuation methods, even though they present other drawbacks.

1.2.2 The minimum total power problem for fluid dynamics

Formulation (1.1) is completely general so that it allows us to address the topology optimization problem in a different context, by properly modifying function $\mathcal{J}$ and the state equation $\mathcal{S}$. In particular, we focused on the optimal allocation of a solid structure in a creeping flow of a Newtonian fluid. Namely, we cast the optimization problem in the setting of a generalized Stokes system. Thus, the state problem coincides with the weak form

find $(\mathbf{u}, p) \in V \times Q$ such that

$$\begin{cases} \int_\Omega \mu \nabla \mathbf{u} : \nabla \mathbf{v} d\Omega + \int_\Omega \alpha \mathbf{u} \cdot \mathbf{v} d\Omega - \int_\Omega p\, \mathrm{div} \mathbf{v} d\Omega = \int_\Omega \mathbf{f} \cdot \mathbf{v} d\Omega \quad \forall \mathbf{v} \in V \\ -\int_\Omega q\, \mathrm{div} \mathbf{u}\, d\Omega = 0 \quad \forall q \in Q, \end{cases} \tag{1.9}$$

with $\mathbf{u}$ and p the velocity and the pressure of the fluid, respectively, and where $\mu \in \mathbb{R}^+$ is the fluid viscosity, $\alpha \in \mathbb{R}^+$ is the inverse permeability, and $\mathbf{f} \in [L^2(\Omega)]^2$ is the forcing term. The function spaces involved in the formulation (1.9) are the standard Sobolev space for the velocity $V = [H^1_{\Gamma_D}(\Omega)]^2$, with $\Gamma_D \subset \partial\Omega$, and $Q = L^2(\Omega)$. We identify by $a_\rho(\cdot,\cdot) : V \times V \to \mathbb{R}$ the bilinear form

$$a_\rho(\mathbf{u},\mathbf{v}) = \int_\Omega \mu \nabla \mathbf{u} : \nabla \mathbf{v} d\Omega + \int_\Omega \alpha \mathbf{u} \cdot \mathbf{v} d\Omega,$$

while the form $b_\rho(\cdot,\cdot) : V \times Q \to \mathbb{R}$ is

$$b_\rho(\mathbf{v},p) - \int_\Omega p \, \mathrm{div}\mathbf{v} d\Omega,$$

and the linear term is referred to as $c(\cdot) : V \to \mathbb{R}$ and coincides with

$$c(\mathbf{v}) = \int_\Omega \mathbf{f} \cdot \mathbf{v} d\Omega.$$

The topology optimization problem using the SIMP approach requires a proper penalization model in order to drive the allocation of fluid and material, without any intermediate behaviour represented by intermediate densities. To this end, the design variable ρ is used to indicate the presence of fluid where $\rho = 1$ and of solid for $\rho = 0$, and the inverse permeability $\alpha = \alpha(\rho)$ is modified accordingly with the introduction of a convex, decreasing, and nonnegative function, e.g. $\alpha(\rho) = \rho^{-1} - 1$ [30]. As in [18], we decide to model α to attain low values in correspondence with the fluid and high values for the solid, so that

$$\alpha(\rho) = \bar{\alpha} + (\underline{\alpha} - \bar{\alpha})\rho \frac{1+t}{\rho + t},$$

where $\underline{\alpha}$ and $\bar{\alpha}$ are the minimum and maximum value for the inverse permeability, respectively, and the parameter t penalizes the intermediate densities, playing the role of the penalization exponent in the minimum compliance problem. In particular, $t > 0$ and large values of this parameter discourage intermediate values for ρ. Moreover, notice that the function $\alpha(\rho)$ attains the minimum value $\underline{\alpha}$ for $\rho = 1$, i.e., that the permeability of the fluid is $\underline{\alpha}^{-1}$, whereas the maximum value $\bar{\alpha}$ is reached in correspondence with the solid for $\rho = 0$. Thus, the final problem for the optimal design in the framework of Stokes flow reads as

$$\min_{\rho \in L^\infty(\Omega)} \mathcal{J}(\mathbf{u}(\rho)) \; : \begin{cases} a_\rho(\mathbf{u}(\rho),\mathbf{v}) + b - \rho(\mathbf{v},p) = c(\mathbf{v}) \quad \forall \mathbf{v} \in V \\ b_\rho(\mathbf{u}(\rho),q) = 0 \quad \forall q \in Q \\ \int_\Omega \rho \, d\Omega \leq \beta |\Omega| \\ 0 \leq \rho \leq 1, \end{cases} \tag{1.10}$$

where β is the volume fraction, and the objective functional $\mathcal{J}$ coincides with the total potential power defined as

$$\mathcal{J}(\mathbf{u}(\rho)) = \frac{1}{2}a_\rho(\mathbf{u}(\rho), \mathbf{u}(\rho)) - c(\mathbf{u}(\rho)),$$

which amounts to minimizing the dissipated power in the fluid, while maximizing the flow velocity in correspondence with the forcing term.

The numerical discretization is straightforward with the same setting as in the linear elastic case. In particular, we choose linear finite elements for the pressure and the design variable ρ, and quadratic finite elements for the velocity field $\mathbf{u}$.

We remark that for the minimum total power problem, the solution is unique and smooth and the penalization model guarantees a clear alternation of fluid and solid areas. Hence, neither regularization nor other advanced techniques are required to avoid undesirable numerical issues, such as mesh dependence and checkerboard patterns.

Here we report a test case from [18], where a diffuser and a curved pipe are modeled. Concerning the diffuser test case, the domain Ω is the unitary square. At the inlet boundary $\Gamma_1 = \{(x, y) \in \partial\Omega : x = 0\}$ a parabolic Dirichlet condition with maximum flow velocity $\mathbf{u}_{max}^{\Gamma_1} = [1, 0]^T$ is imposed, whereas at the outflow $\Gamma_2 = \{(x, y) \in \partial\Omega : x = 1, y \in [1/3, 2/3]\}$ we impose a parabolic profile with maximum value $\mathbf{u}_{max}^{\Gamma_2} = [3, 0]^T$. Homogeneous Dirichlet conditions are imposed on $\partial\Omega \setminus (\Gamma_1 \cup \Gamma_2)$. The diffusivity is $\mu = 1$, the forcing term $\mathbf{f} = \mathbf{0}$, the volume fraction $\beta = 0.5$, $t = 0.1$, $\underline{\alpha} = 2.5\mu/100^2$ and $\bar{\alpha} = 2.5\mu/0.01^2$. The cardinality of the mesh employed for the discretization is 3779.

For the curved pipe test case, the domain Ω is the unitary square. At the inlet boundary $\Gamma_1 = \{(x, y) \in \partial\Omega : x = 0, y \in [7/12, 3/4]\}$ a parabolic Dirichlet condition with maximum flow velocity $\mathbf{u}_{max}^{\Gamma_1} = [1, 0]^T$ is imposed, whereas at the outflow $\Gamma_2 = \{(x, y) \in \partial\Omega : x = 1, y \in [7/12, 3/4]\}$ we impose a parabolic profile with maximum value $\mathbf{u}_{max}^{\Gamma_2} = [1, 0]^T$. Homogeneous Dirichlet conditions are imposed on $\partial\Omega \setminus (\Gamma_1 \cup \Gamma_2)$. The forcing term is $\mathbf{f} = [f_x, 0]^T$, with $f_x = 562.5/|\Omega_f|\chi_{\Omega_f}$, and χ_{Ω_f} the characteristic function of the set $\Omega_f = \{(x, y) \in \Omega : (x - 1/2)^2 + (y - 1/3)^2 \leq (1/12)^2\}$ .The diffusivity is $\mu = 1$ the volume fraction $\beta = 0.25$, $t = 0.1$, $\underline{\alpha} = 2.5\mu/100^2$ and $\bar{\alpha} = 2.5\mu/0.01^2$. The computing mesh consists of 6714 elements.

The results in Figure 1.3 are obtained resorting to a standard finite element discretization.

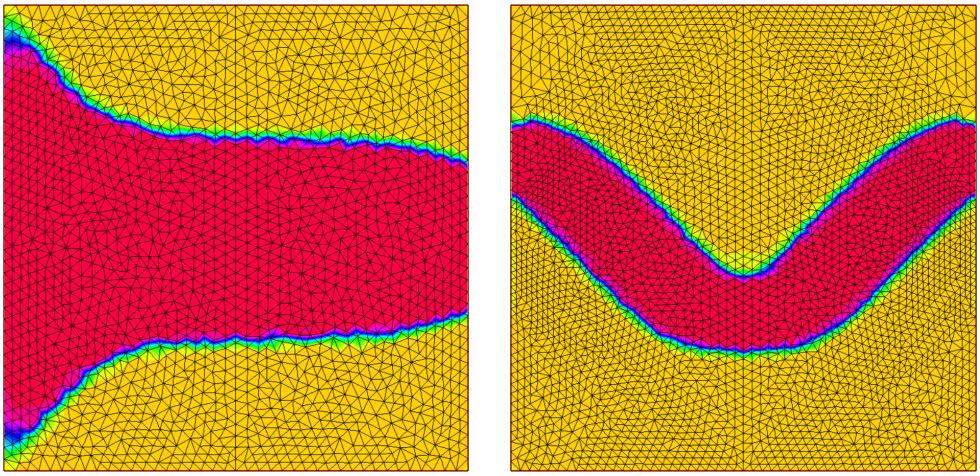

Figure 1.3: Numerical results for the topology optimization of a diffuser (left), and of a curved pipe (right) with the use of standard finite elements techniques.

1.3 Advanced techniques for topology optimization

Topology optimization can be enhanced from both a modeling and a numerical viewpoint, with an *ad-hoc* combination of TO with cutting-edge techniques. Specifically, we propose new methods that aim at containing some of the issues related to the SIMP method. In particular, we want to improve the overall quality of the optimized structure in terms of sharpness of the material/void interface and computation time. Additionally, with a view to the design of new metamaterials, we will also deal with the so-called inverse topology optimization.

To this aim, three techniques will be exploited, namely an anisotropic mesh adaptation procedure, the homogenization theory, and the Proper Orthogonal Decomposition.

1.3.1 Mesh adaptation

The mesh adaptation technique is an automatic procedure to suitably modify the spatial computational mesh $\mathcal{T}_h$ employed for the discretization of a PDE.

In particular, the purpose is to adapt the allocation of the elements of the grid so that the discretization error, e_h, or a functional of the error, $Y(e_h)$, can be controlled. This procedure leads to local refinement or coarsening operations according to the information provided by e_h or $Y(e_h)$, i.e., the mesh is expected to be finer in correspondence with the source of errors (e.g., boundary layers, shocks) and coarser where the error is less relevant. Mesh adaptation can be carried out by modifying the size of the elements only, thus resulting in an isotropic mesh, or the size, the shape, and the orientation of the elements in an anisotropic setting.

In this work, we will address mesh adaptation in an anisotropic framework which turns out to be particularly useful when the phenomena under investigation present preferential directions.

The error recovery procedure

In order to drive the mesh adaptation procedure, it is necessary to extract the required information out of e_h or some other sources related to the error. We focus on the mesh adaption procedure driven by the H^1-seminorm of the discretization error, $|e_h|_{H^1(\Omega)} = ||\nabla u - \nabla u_h||_{L^2(\Omega)}$, where u is unknown and represents the main quantity of the problem at hand, while u_h is the discrete approximation to u. In the case of practical problems, when the exact solution is not known *a priori*, the error e_h has to be estimated. The definition of the error estimator can be undertaken with the choice from a vast production [9, 33, 49, 62].

The approach that we investigate in this work is the one proposed by O.C. Zienkiewicz and J.Z. Zhu in [82, 83, 84], where the error is recovered in terms of the discrete solution. Specifically, the H^1-seminorm of the error is estimated using the recovery operator P for the gradient such that

$$|e_h|_{H^1(\Omega)} \simeq ||P(\nabla u_h) - \nabla u_h||_{L^2(\Omega)} = \eta. \tag{1.11}$$

The estimator η is thus fully computable in the spirit of an *a posteriori* error analysis.

Among the available recipes for the recovered gradient $P(\nabla u_h)$, we adopt the one provided in [57] defined over the patch of the element $\Delta_K = \{T \in \mathcal{T}_h : T \cap K \neq \emptyset\}$, namely the set of elements sharing at least one vertex with K. Operator P is such that

$$\int_{\Delta_K} (\nabla u_h - P(\nabla u_h)) \cdot \mathbf{v}\, d\mathbf{x} = 0 \quad \mathbf{v} \in \mathbb{P}^r,$$

and $\mathbb{P}(\nabla u_h)$ is a polynomial of degree r as well. In the following we consider only the case $r = 0$, i.e., a piecewise constant reconstruction of the gradient over the patch Δ_K,

$$P(\nabla u_h) = \frac{1}{|\Delta_K|} \sum_{T \in \Delta_K} |T| \nabla u_h|_T, \tag{1.12}$$

where $|\cdot|$ is the Euclidean measure. Although this procedure is simple and may lack of richness, it turns out to be very handy from an implementative viewpoint. Unlike other common recovery gradient recipes, this technique is not characterized by a high polynomial degree, i.e., it is not improving the information carried by the discrete gradient ∇u_h. However, this drawback is balanced by the non-local average operation involving all the elements in the patch Δ_K.

The isotropic setting

The adaptation procedure in an isotropic setting has been extensively investigated in the literature [1, 10, 48, 65, 77]. The idea is to predict the optimal element size h_K, to generate a mesh able to capture the phenomenon at hand to within a desired threshold on the (estimated) error. The estimator η in (1.11) can be written in terms of the local contributions, η_K, such that

$$\eta^2 = \sum_{K \in \mathcal{T}_h} \eta_K^2.$$

The quantity $\tilde{\eta}_K^2 = |K|^{-1} \eta_K^2$ is the scaled version of the local estimator η_K and can be exploited to retrieve the optimal grid space. In particular, we remark that the equality $|K| = h_K^2 |\hat{K}|/3$ relates the areas of the reference element, $\hat{K}$, and of the generic triangle K, when the reference element is the equilateral triangle inscribed into the unit circle. To proceed with the computation of the optimal grid, we fix two criteria: i) $\eta \leq \texttt{MTOL}$, with MTOL a user-defined quantity ; ii) the error is equidistributed over all the elements of the mesh, namely

$$\text{i) } \eta \leq \texttt{MTOL}; \quad \text{ii) } \eta_K^2 = \frac{\texttt{MTOL}^2}{\#\mathcal{T}_h}.$$

Using the second criterion and the scaled version of the estimator, we get

$$\frac{h_K^2|\hat{K}|\tilde{\eta}_K^2}{3} = \frac{\texttt{MTOL}^2}{\#\mathcal{T}_h},$$

implying the formula for the optimal size of the element K

$$h_K = \left[\frac{\texttt{MTOL}^2}{3\,\#\mathcal{T}_h|\hat{K}|\tilde{\eta}_K^2}\right]^{1/2}.$$

The anisotropic setting

In an anisotropic setting, as in [27, 31, 34, 35, 57], the geometric properties of an element K are extracted from the spectral properties of the affine transformation T_K, which maps the reference element $\widehat{K}$ inscribed in the unit circle in 2D and in the unit sphere in 3D into K, such that

$$\mathbf{x} = T_K(\hat{\mathbf{x}}) = M_K\hat{\mathbf{x}} + \mathbf{t}_K,$$

with $\mathbf{x} \in K$, $\hat{\mathbf{x}} \in \widehat{K}$, $M_K \in \mathbb{R}^{d\times d}$, $\mathbf{t}_K \in \mathbb{R}^d$, $d = 2, 3$. In particular, the map T_K transforms the unit circle into an ellipse circumscribing the 2-dimensional element K and the unit sphere into an ellipsoid circumscribing the tetrahedron K (see Figure 1.4).

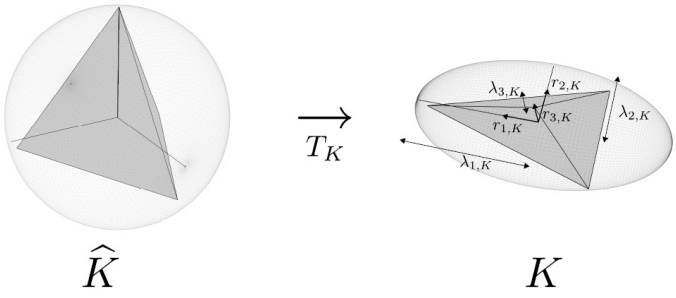

Figure 1.4: The affine map T_K in 3D.

By means of the polar decomposition, the Jacobian M_K is factorized as the product $B_K Z_K$, with $B_K \in \mathbb{R}^{d\times d}$ a symmetric positive definite matrix performing a deformation of the element K, and $Z_K \in \mathbb{R}^{d\times d}$ an orthogonal matrix applying a rigid rotation to K. Matrix B_K can be decomposed in terms of the associated eigenvalues and eigenvectors, namely

$B_K = R_K^T \Lambda_K R_K$, with $R_K^T = [\mathbf{r}_{1,K}, \dots, \mathbf{r}_{d,K}]$ and $\Lambda_K = \mathrm{diag}(\lambda_{1,K}, \dots, \lambda_{d,K})$, with $\lambda_{1,K} \geq \cdots \geq \lambda_{d,K}$, $d = 2, 3$.
We remark that R_K^T and Λ_K collect the geometric properties of the element K, the eigenvectors $\mathbf{r}_{i,K}$ identifying the directions of the semi-axes of the ellipsoid circumscribed to K, for $i = 1, 2, 3$ (in the 2D case $\mathbf{r}_{i,K}$, with $i = 1, 2$ are the directions of the semi-axes of the circumscribing ellipse), and the eigenvalues $\lambda_{i,K}$ representing the length of such semi-axes. In the following, we focus on the 3-dimensional case, only stating the main results in the 2D case.

We introduce the aspect ratios of the tetrahedron K,

$$s_{i,K} = \left(\frac{\lambda_{i,K}^2}{\prod_{j \neq i} \lambda_{j,K}} \right)^{2/3}, \quad i = 1, 2, 3,$$

which provide a measure of the distortion of the element in the i-th direction. In particular, it is straigthforward to verify that $s_{1,K} \geq s_{2,K} \geq s_{3,K}$, and $s_{1,K} s_{2,K} s_{3,K} = 1$, with the isotropic case being recovered with the choice $s_{1,K} = s_{2,K} = s_{3,K} = 1$.

As in the isotropic case, the error estimator is decomposed in terms of the local contributions, i.e.,

$$\eta^2 = \sum_{K \in \mathcal{T}_h} \eta_K^2, \tag{1.13}$$

where the local estimator η_K is obtained via projection of the recovered error on the principal directions of the element K, as initially proposed in a 2D setting in [56], such that

$$\eta_K^2 = \frac{1}{(\lambda_{1,K} \lambda_{2,K} \lambda_{3,K})^{2/3}} \sum_{i=1}^{3} \lambda_{i,K}^2 \left(\mathbf{r}_{i,K}^T \, G_{\Delta_K}\big(E_\nabla\big) \mathbf{r}_{i,K} \right), \tag{1.14}$$

with $E_\nabla = \big[P(\nabla u_h) - \nabla u_h\big]_{\Delta_K}$ the recovered error, and $G_{\Delta_K}(\cdot) \in \mathbb{R}^{3\times 3}$ is the symmetric positive semidefinite matrix with entries

$$[G_{\Delta_K}(\mathbf{w})]_{i,j} = \sum_{T \in \Delta_K} \int_T w_i \, w_j \, dT \quad \text{with } i, j = 1, 2, 3, \tag{1.15}$$

for any vector-valued function $\mathbf{w} = (w_1, w_2, w_3)^T \in [L^2(\Omega)]^3$. The isotropic case is a special case of (1.14) for the choice $\lambda_{1,K} = \lambda_{2,K} = \lambda_{3,K}$.

This estimator is prompted by the anisotropic error estimate for the Clément quasi interpolant, I_h^1, proposed in [31].

Lemma 1.3.1 *Let $v \in H^1(\Omega)$. If $\#\Delta_K \leq C_1$ and $diam(\hat{\Delta}_K) \leq C_2$, there exists a constant $C = C(C_1, C_2)$ such that*

$$||v - I_h^1(v)||_{L^2(K)} \leq C \sum_{i=1}^{3} \lambda_{i,K}^2 \left(\mathbf{r}_{i,K}^T \, G_{\Delta_K}(\nabla v) \mathbf{r}_{i,K} \right)^{1/2} \quad \forall K \in \mathcal{T}_h,$$

where $\#\Delta_K$ identifies the cardinality of the patch associated with K and $diam(\hat{\Delta}_K)$ is the diameter of the pullback of Δ_K via the map T_K, i.e., $\hat{\Delta}_K = T_K^{-1}(\Delta_K)$.

The adaptive procedure The mesh adaptation procedure exploits the estimator (1.14) in a predictive way, resorting to a metric-based setting [38]. In more detail, a metric, $\mathcal{M} : \Omega \to \mathbb{R}^{3\times 3}$, is a symmetric positive definite tensor field which contains all the geometric information related to a certain mesh. In a finite element setting, we approximate $\mathcal{M}$ by a piecewise constant function, $\mathcal{M}_{\mathcal{T}_h}$, associated with the actual grid $\mathcal{T}_h$, such that $\mathcal{M}_{\mathcal{T}_h}\big|_K = R_K^T \Lambda_K^{-2} R_K$, consistently with the notation introduced above.

The ultimate goal of the adaptation procedure is to define a new metric tensor guided by η_K. This goal is reached via an iterative procedure which, eventually, yields an optimal adapted grid satisfying two criteria: i) the number of elements is minimized under the accuracy constraint, $\eta \leq \texttt{MTOL}$, with MTOL a user-defined tolerance; ii) the error is equidistributed among all the elements of the actual grid, namely, $\eta_K^2 = \texttt{MTOL}^2/\#\mathcal{T}_h$, with $\#\mathcal{T}_h$ the mesh cardinality.

The procedure adopted for the prediction of the metric entails a local optimization problem, as in [31, 57]. The local estimator η_K is firstly rewritten by collecting the size information of the patch in a single factor, $|\Delta_K|$, as

$$\eta_K^2 = |\Delta_K| \underbrace{\sum_{i=1}^{3} s_{i,K} \left(\mathbf{r}_{i,K}^T \, \widehat{G}_{\Delta_K}(E_\nabla) \, \mathbf{r}_{i,K} \right)}_{\mathcal{F}_3(\{s_{i,K}, \mathbf{r}_{i,K}\}_{i=1,2,3})},$$

where $\widehat{G}_{\Delta_K}(\cdot)$ is the scaled matrix $G_{\Delta_K}(\cdot)/|\Delta_K|$, and $|\Delta_K| = \lambda_{1,K}\lambda_{2,K}\lambda_{3,K}\,|\widehat{\Delta}_K|$, with $\widehat{\Delta}_K = T_K^{-1}(\Delta_K)$. Notice that $|\Delta_K|$ is a quantity related to the volume

of the tetrahedra in the patch Δ_K, whereas the other terms keep track of the orientation and of the stretching of K.

Minimizing the cardinality of the mesh is equivalent to maximizing the size of the patch, so that we are led to solve the local constrained minimization problem

$$\min_{s_{i,K},\mathbf{r}_{i,K}} \mathcal{F}_3(\{s_{i,K},\mathbf{r}_{i,K}\}_{i=1,2,3}) \; : \begin{cases} \mathbf{r}_{i,K}\cdot\mathbf{r}_{j,K} = \delta_{ij} \\ s_{1,K} \geq s_{2,K} \geq s_{3,K} \\ s_{1,K}s_{2,K}s_{3,K} = 1, \end{cases} \tag{1.16}$$

with δ_{ij} the Kronecker symbol and $i,j = 1,2,3$. This problem has a solution in a closed formula provided in [31, 57] as stated in the following

Proposition 1.3.1 *Let $\{g_i,\mathbf{g}_i\}_{i=1,2,3}$ be the eigenpairs associated with $\widehat{G}_{\Delta_K}(E_\nabla)$, with $g_1 \geq g_2 \geq g_3 > 0$ and $\{\mathbf{g}_i\}_{i=1,2,3}$ orthonormal. Then, $\mathcal{F}_3(\cdot)$ is minimized when*

$$s_{1,K} = \frac{\sqrt[3]{\Pi_{i=1}^3 g_i}}{g_3}, \quad s_{2,K} = \frac{\sqrt[3]{\Pi_{i=1}^3 g_i}}{g_2}, \quad s_{3,K} = \frac{\sqrt[3]{\Pi_{i=1}^3 g_i}}{g_1},$$
$$\mathbf{r}_{1,K} = \mathbf{g}_3, \quad \mathbf{r}_{2,K} = \mathbf{g}_2, \quad \mathbf{r}_{3,K} = \mathbf{g}_1.$$

Next, by employing the equidistribution criterion, the optimal values for the lengths $\lambda_{i,K}$ can be computed as

$$\lambda_{1,K} = g_3^{-1/2}\left(\frac{\texttt{MTOL}^2}{3\,\#\mathcal{T}_h|\widehat{\Delta}_K|}\right)^{1/3}\Big(\prod_{i=1}^3 g_i\Big)^{1/18},$$
$$\lambda_{2,K} = g_2^{-1/2}\left(\frac{\texttt{MTOL}^2}{3\,\#\mathcal{T}_h|\widehat{\Delta}_K|}\right)^{1/3}\Big(\prod_{i=1}^3 g_i\Big)^{1/18},$$
$$\lambda_{3,K} = g_1^{-1/2}\left(\frac{\texttt{MTOL}^2}{3\,\#\mathcal{T}_h|\widehat{\Delta}_K|}\right)^{1/3}\Big(\prod_{i=1}^3 g_i\Big)^{1/18}.$$

The 2D case can be obtained by properly modifying the indices in the estimator and the scaling factors used for the factorization of η_K. In more detail, the local estimator is

$$\eta_K^2 = |\Delta_K| \underbrace{\sum_{i=1}^2 s_{i,K}\left(\mathbf{r}_{i,K}^T\,\widehat{G}_{\Delta_K}(E_\nabla)\,\mathbf{r}_{i,K}\right)}_{\mathcal{F}_2(\{s_{i,K},\mathbf{r}_{i,K}\}_{i=1,2})},$$

and the local optimization problem reads as

$$\min_{s_K,\mathbf{r}_{i,K}} \mathcal{F}_2(\{s_K,\mathbf{r}_{i,K}\}_{i=1,2}) \ : \begin{cases} \mathbf{r}_{i,K}\cdot\mathbf{r}_{j,K}=\delta_{ij} \\ s_K \geq 1, \end{cases} \tag{1.17}$$

where $i,j=1,2$, and here the aspect ratio is defined as $s_K=\lambda_{1,K}/\lambda_{2,K}$.

Proposition 1.3.2 *Let $\{g_i,\mathbf{g}_i\}_{i=1,2}$ be the eigenpairs associated with $\widehat{G}_{\Delta_K}(E_\nabla)$, with $g_1 \geq g_2 > 0$ and $\{\mathbf{g}_i\}_{i=1,2}$ orthonormal. Then, $\mathcal{F}_2(\cdot)$ is minimized when*

$$s_K=\sqrt{g_1/g_2}, \quad \mathbf{r}_{1,K}=\mathbf{g}_2, \quad \mathbf{r}_{2,K}=\mathbf{g}_1.$$

The optimal values for the lengths $\lambda_{i,K}, i=1,2$ are

$$\lambda_{1,K}=g_2^{-1/2}\left(\frac{\texttt{MTOL}^2}{2\#\mathcal{T}_h\,|\widehat{\Delta}_K|}\right)^{1/2}, \quad \lambda_{2,K}=g_1^{-1/2}\left(\frac{\texttt{MTOL}^2}{2\#\mathcal{T}_h\,|\widehat{\Delta}_K|}\right)^{1/2}, \tag{1.18}$$

with $|\widehat{\Delta}_K|=|\Delta_K|/(\lambda_{1,K}\lambda_{2,K})$.

Numerical results Here we employ anisotropic mesh adaptation to discretize the same test cases already analyzed in Section 1.2.2, where a diffuser and a curved pipe are modeled. For the two test cases, $\texttt{MTOL}=0.1$. Figure 1.5 shows the optimized results.

For the diffuser and the curved pipe, the anisotropic grids are characterized by 1636 elements and $\max s_K = 19.85$, and 2746 elements and $\max s_K = 15.72$, respectively. The quality of the solution (compare Figure 1.3 with Figure 1.5) is enhanced with the use of an anisotropic grid, but it presents the same topology as in the isotropic case. This makes the fluid setting somewhat less interesting than the structural framework, where the impact of anisotropic meshes will be more relevant (see Chapters $2-4$).

1.3.2 The homogenization theory

The term homogenization is used to indicate a class of procedures developed to study the macroscopic behaviour of a structure characterized by periodic inhomogeneities at the microscale level. Such periodic media are very common (e.g., bones, metamaterials, honeycomb patterns). The study of such

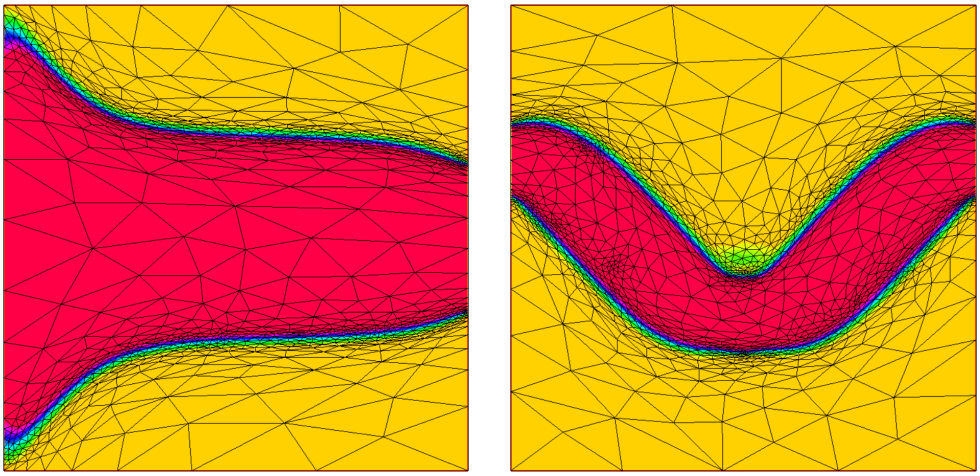

Figure 1.5: Numerical results for the topology optimization of a diffuser (left), and of a curved pipe (right) with the employment of anisotropically adapted meshes.

materials requires an analysis of both the macro- and the micro-scales, thus entailing a considerable computational cost. Homogenization is a smart way to avoid dealing simultaneosuly with both scales, since it allows one to describe the effective properties of a medium at the macroscale taking into account the effects of the micro-scale [68, 69].

Consider a bounded domain $\Omega \subset \mathbb{R}^3$ obtained by repeating domain $Y \subset \mathbb{R}^3$ periodically. The microscale and the macroscale coordinates, $\mathbf{y}$ and $\mathbf{x}$, respectively, can be related by means of a small parameter η, such that $\mathbf{y} = \mathbf{x}/\eta$. The properties of the system Ω is assumed to be modeled by an elliptic equation whose coefficients C_{ij} depend on the coordinate $\mathbf{y}$ and are Y-periodic, i.e.,

$$C_{ij} = C_{ij}(\mathbf{y}), \quad C_{ij}(\mathbf{y}) = C_{ij}(\mathbf{y} + N\mathbf{p}),$$

where N is a diagonal matrix and $\mathbf{p}$ is a vector identifying the period (see Figure 1.6).

The differential problem under investigation is

$$\begin{cases} \mathcal{C}^\eta u^\eta = f & \text{in } \Omega \\ u^\eta = 0 & \text{on } \partial\Omega, \end{cases} \tag{1.19}$$

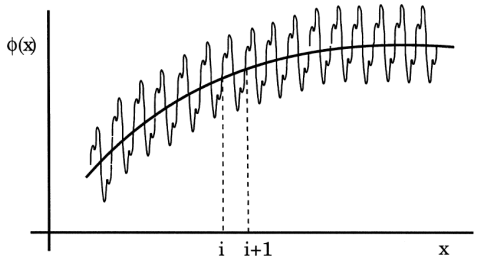

Figure 1.6: A Y-periodic function ϕ. The local oscillations are superimposed to the average. Figure extracted from [47].

where the right-hand side f is chosen so that the problem is well-posed, and we assume the elliptic operator to be

$$\mathcal{C}^\eta = -\sum_{i,j=1}^{3} \frac{\partial}{\partial x_i}\left(C_{ij}(\mathbf{y})\frac{\partial}{\partial x_j}\right).$$

By adopting the asymptotic expansion of u^η with respect to the parameter η, the solution u^η is expressed as

$$u^\eta(\mathbf{x}) = u^0(\mathbf{x},\mathbf{y}) + \eta u^1(\mathbf{x},\mathbf{y}) + \eta^2 u^2(x,\mathbf{y})\ldots \quad \mathbf{y} = \mathbf{x}/\eta, \tag{1.20}$$

all the functions u^i being Y-periodic.

The chain rule for the total derivative

$$\frac{\partial}{\partial x_i} = \frac{\partial}{\partial x_i} + \eta^{-1}\frac{\partial}{\partial y_i},$$

leads to the decomposition of the elliptic operator as

$$\mathcal{C}^\eta = \eta^{-2}\mathcal{C}^1 + \eta^{-1}\mathcal{C}^2 + \mathcal{C}^3, \tag{1.21}$$

where the three operators $\mathcal{C}^i, i = 1, 2, 3$ are defined as

$$\begin{cases} \mathcal{C}^1 = -\sum_{i,j=1}^{3} \frac{\partial}{\partial y_i}\left(C_{ij}(\mathbf{y})\frac{\partial}{\partial y_j}\right), \\ \mathcal{C}^2 = -\sum_{i,j=1}^{3} \left[\frac{\partial}{\partial y_i}\left(C_{ij}(\mathbf{y})\frac{\partial}{\partial x_j}\right) + \frac{\partial}{\partial x_i}\left(C_{ij}(\mathbf{y})\frac{\partial}{\partial y_j}\right)\right], \\ \mathcal{C}^3 = -\sum_{i,j=1}^{3} \frac{\partial}{\partial x_i}\left(C_{ij}(\mathbf{y})\frac{\partial}{\partial x_j}\right). \end{cases}$$

Using the expansion of the operator (1.21) and of the solution (1.20), the differential problem in (1.19) becomes

$$(\eta^{-2}\mathcal{C}^1 + \eta^{-1}\mathcal{C}^2 + \mathcal{C}^3)(u^0(\mathbf{x},\mathbf{y}) + \eta u^1(\mathbf{x},\mathbf{y}) + \eta^2 u^2(x,\mathbf{y})\dots) = f.$$

By collecting the terms with the same power of η and neglecting the terms involving positive power of η, we get the system

$$\begin{cases} \mathcal{C}^1 u^0 = 0, \\ \mathcal{C}^1 u^1 + \mathcal{C}^2 u^0 = 0, \\ \mathcal{C}^1 u^2 + \mathcal{C}^2 u^1 + \mathcal{C}^3 u^0 = f. \end{cases} \tag{1.22}$$

The first equation in (1.22) admits a unique solution, and since $\mathcal{C}^1$ contains only derivatives with respect to the microscale coordinates, we find that $u^0 = u^0(\mathbf{x})$ depends only on the macroscale and is not affected by the microscopic fluctuations. The second equation in (1.22) now reads

$$\mathcal{C}^1 u^1 = -\mathcal{C}^2 u^0 = \sum_{i,j=1}^{3} \left[\frac{\partial}{\partial y_i}\left(C_{ij}(\mathbf{y})\frac{\partial}{\partial x_j}\right) + \frac{\partial}{\partial x_i}\left(C_{ij}(\mathbf{y})\frac{\partial}{\partial y_j}\right)\right] u^0(\mathbf{x}),$$

which reduces to

$$\mathcal{C}^1 u^1 = \sum_{i,j=1}^{3} \frac{\partial C_{ij}(\mathbf{y})}{\partial y_i}\frac{\partial u^0(\mathbf{x})}{\partial x_j}. \tag{1.23}$$

Equation (1.23) has a solution of the form

$$u^1(\mathbf{x},\mathbf{y}) = \sum_{j=1}^{3} S^j(\mathbf{y})\frac{\partial u^0(\mathbf{x})}{\partial x_j} + s(\mathbf{x}),$$

because the operator $\mathcal{C}^1$ only entails derivatives in $\mathbf{y}$. Here $S^j(\mathbf{y}), j = 1, 2, 3$ derive from the integration of the equation in Y and $s(\mathbf{x})$ plays the role of the integration constant.

The equation $\mathcal{C}^1 w = g$ in Y has a unique solution if the average over Y of the right-hand side g is 0. Hence, the last equation of system (1.22) has a unique solution if

$$-\frac{1}{|Y|}\int_Y (\mathcal{C}^2 u^1 + \mathcal{C}^3 u^0) d\mathbf{y} + f = 0. \tag{1.24}$$

Equation (1.24) combined with the definition of $u^1(\mathbf{x}, \mathbf{y})$ and the periodicity assumption on the coefficients $C_{ij}(\mathbf{y})$, yields the following equations for $u^0(\mathbf{x})$

$$-C_{ij}^H \frac{\partial^2 u^0}{\partial x_i \partial x_j}(\mathbf{x}) = f \quad \text{in } \Omega,$$

where the coefficients C_{ij}^H characterize the homogenized differential operator and are given by

$$C_{ij}^H = \frac{1}{|Y|}\int_Y \left(C_{ij}(\mathbf{y}) + \sum_{k=1}^{3} C_{ik}(\mathbf{y}) \frac{\partial S(\mathbf{y})}{\partial y_k} \right) d\mathbf{y}.$$

The elastic case

In this section, we will focus on the homogenization problem in the elastic case. We indicate by E_{ijkl} the stiffness tensor entering Hooke's law, such that

$$\sigma_{ij} = E_{ijkl}\varepsilon_{kl},$$

where σ_{ij} is (i, j)-th component of the stress tensor, $i, j = 1, 2, 3$, and

$$\varepsilon_{kl} = \frac{1}{2}\left(\frac{\partial u_k}{\partial x_l} + \frac{\partial u_l}{\partial x_k} \right),$$

is the (k, l)-th component of the strain tensor, $k, l = 1, 2, 3$. Einstein notation has been adopted and we assume that the tensor E_{ijkl} is symmetric and coercive [47, 69].

The goal of the homogenization procedure is to compute the effective elastic properties of a periodic body, namely E_{ijkl}^H. For this purpose, let us

consider the microscopic reference cell $Y \subset \mathbb{R}^3$ constituting the periodic pattern of the macroscopic medium $\Omega \subset \mathbb{R}^3$. The general setting (1.19) can be exploited in the linear elastic framework. Under these assumptions, the field u defined over the macroscopic domain Ω can be expressed using expansion (1.20) where u is now the displacement, and the differential equation is [43]

$$-\frac{\partial \sigma_{ij}}{\partial x_j} = -\frac{\partial}{\partial x_j} E_{ijkl}\varepsilon_{kl} = f_i \quad \text{in } \Omega,$$

where f_i is the i-th component of the forcing term, and ε_{kl} contains the derivatives of the displacement.

By repeating the general framework introduced above and considering only the first two terms in (1.20), the homogenized tensor is given by

$$E^H_{ijkl} = \frac{1}{|Y|}\int_Y E_{ijpq}\left(\varepsilon^{0,(kl)}_{pq} - \varepsilon^{*,(kl)}_{pq}\right) d\mathbf{y},$$

where $\varepsilon^{0,(kl)}_{pq}$ is one of 9 linearly independent unit prestrain fields, with $p, q, k, l = 1, 2, 3$ [72]. The periodic microscale fluctuation $\varepsilon^{*,(kl)}_{pq}$ is defined by a differential problem

find $\varepsilon^{*,(kl)}_{pq} \in E$ such that

$$\int_Y E_{ijpq}\varepsilon_{ij}(\mathbf{v})\varepsilon^{*,(kl)}_{pq} d\mathbf{y} = \int_Y E_{ijpq}\varepsilon_{ij}(\mathbf{v})\varepsilon^{0,(kl)}_{pq} d\mathbf{y} \quad \forall \mathbf{v} \in E,$$

where E is a Y-periodic Sobolev space.

For further details, we refer to [47, 69]. In [72], this procedure is referred to as direct homogenization in contrast with inverse homogenization, dealing with the optimal design of periodic media whose homogenized tensor is prescribed (see Chapter 3).

1.3.3 Proper Orthogonal Decomposition

The Proper Orthogonal Decomposition is a method to address the model order reduction of a problem of interest, referred to as full-size problem, so that the dimension of the new problem (reduced problem) is considerably lower with respect to the dimension of the full model. It is extremely suited for parametric differential problems and allows one to quickly compute the solution corresponding to new user-defined parameters. This is made possible

by exploiting some high fidelity pre-computed solutions associated with a certain sampling of the set of parameters.

In particular, the technique consists of two steps, namely the offline and the online phases [50, 67]. The offline phase deals with the collection of the solutions to the full-size problem, called snapshots, for the choice of a sufficiently large set of parameters. The snapshots are collected in the so-called response matrix. Then, the singular value decomposition (SVD) is used to extract a basis out of the snapshots.

We exemplify the POD on the generic weak form of an elliptic PDE, depending on a single parameter $\mu \in \mathbb{R}$,

find $q^\mu \in W$ such that

$$c^\mu(q^\mu, r) = b(r) \quad \forall r \in W, \tag{1.25}$$

where $c^\mu(\cdot,\cdot) : W \times W \to \mathbb{R}$ and $b(\cdot) : W \to \mathbb{R}$ are the bilinear and linear forms, respectively, $W \subset H^1(\Omega)$ is the Hilbert space where the differential problem is set and Ω is the computational domain. For a given value of the parameter $\bar{\mu}$, the solution to (1.25) is indicated by $q^{\bar{\mu}}$ to highlight the dependence on the parameter.

The numerical discretization of (1.25) in a finite element setting, characterized by the step size h, is straightforward by means of Galerkin projections onto the discrete space $W_h \subset W$ whose dimension is N. In more detail, the algebraic version of the discrete equation in (1.25) is

$$C^\mu \mathbf{q}_h^\mu = \mathbf{b}, \tag{1.26}$$

where matrix C^μ represents the stiffness, $\mathbf{q}_h^\mu$ is the vector containing the degrees of freedom of the unknown q_h^μ, and $\mathbf{b}$ is the right-hand side.

We denote by $\{\mu_i\}_{i=1}^M$ the collection of M parameters used to generate the snapshot matrix

$$\mathcal{S} = [\mathbf{q}_h^{\mu_1}, \mathbf{q}_h^{\mu_2}, ..., \mathbf{q}_h^{\mu_M}] \in \mathbb{R}^{N \times M}.$$

The POD method extracts the main features of the considered scenarios via the SVD of matrix $\mathcal{S}$ [42],

$$\mathcal{S} = V \Sigma \Phi^T,$$

with $V \in \mathbb{R}^{N \times N}$ and $\Phi \in \mathbb{R}^{M \times M}$ orthogonal matrices containing the left and right singular vectors of $\mathcal{S}$, respectively, while $\Sigma \in \mathbb{R}^{N \times M}$ is a pseudo-diagonal matrix containing the singular values of the response matrix. The

columns of matrix V provide a basis for the reduced space. Following different criteria [50, 67], one can choose to truncate the size of the reduced basis to tune the richness of the reduced space. In particular, choosing an integer $0 < l \leq M$, we define the POD space as $V_{POD} = \text{span}\{\mathbf{V}_i : i = 1, ..., l\}$, where $\mathbf{V}_i$ is the $i-$th left singular vector of $\mathcal{S}$.

In the online phase, the user picks a new value, μ^*, for the parameter with the goal of building an approximation to the solution $\mathbf{q}_h^{\mu^*}$. For this purpose, we project (1.26) onto V_{POD}. This yields the reduced system

$$\tilde{C}^{\mu^*} \mathbf{q}_h^{\mu^*,POD} = \tilde{\mathbf{b}}, \tag{1.27}$$

where $\tilde{C}^{\mu^*} = \mathcal{V}^T C^{\mu^*} \mathcal{V} \in \mathbb{R}^{l \times l}$ is the reduced stiffness matrix, $\tilde{\mathbf{b}} = \mathcal{V}^T \mathbf{b} \in \mathbb{R}^{\mathbf{l}}$ is the corresponding right-hand side, $\mathbf{q}_h^{\mu^*,POD} \in \mathbb{R}^l$ is the vector of the POD coefficients, and $\mathcal{V} = [\mathbf{V}_1, \ldots, \mathbf{V}_l]$ is the matrix collecting the basis vectors. Finally, it is possible to retrieve the solution on the finite element space by the back-projection

$$\mathbf{q}_h^{\mu^*} \approx \mathcal{V} \mathbf{q}_h^{\mu^*,POD} = \sum_{i=1}^{l} [\mathbf{q}_h^{\mu^*,POD}]_i \mathbf{V}_i,$$

with $[\mathbf{q}_h^{\mu^*,POD}]_i$ the $i-$th component of the POD solution.

1.4 Advanced solutions for the new challenges

In Figure 1.7 the optimized structure obtained by enriching SIMP method with an anisotropic mesh adaptation (see SIMAPATY algorithm in Chapter 2, [58, 59]) for the satellite component is shown. The new layout is characterized by boundaries sharply detected by the mesh adaptation procedure. Unlike in the output of Altair (see Figure 1.1), the alternation of solid and void is clear-cut and the structure does not demand a massive post-processing. A more quantitative comparison between the two structures in terms of mechanical performances is carried out in [32]. After some modifications, the structure has been printed (see Figure 1.8).

As far as the metamaterial application is concerned, the optimization of a microcell in 3D is performed by means of the anisotropic adaptive algorithm starting from a design domain 1 [m] $\times$1 [m] $\times$1 [m] cube, loaded with a compressive traction of magnitude 0.5 [N] located at the centers of the 6 faces, for a volume fraction $\alpha = 0.15$, and with material properties $E = 1$

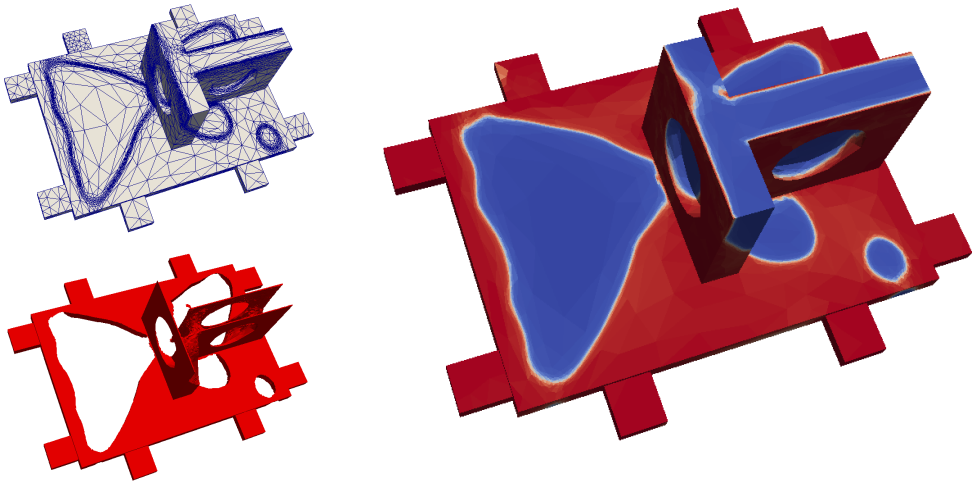

Figure 1.7: Outcome of the SIMPATY algorithm for the satellite component. Adapted anisotropic mesh (top-left), final strucure (bottom-left), and the density variable ρ.

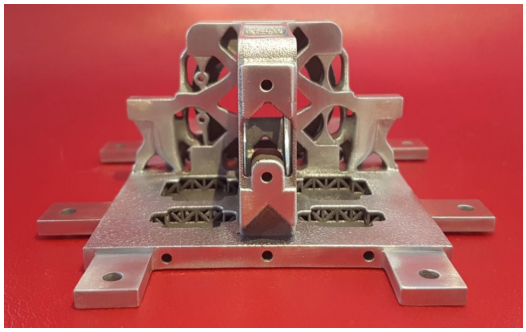

Figure 1.8: 3D printed satellite component.

[Pa] and $\nu = 1/3$. The resulting layout is shown in Figure 1.9 and exhibits sharp boundaries. These results are preliminary and will be developed with a view to a successive 3D-printing of the specimen.

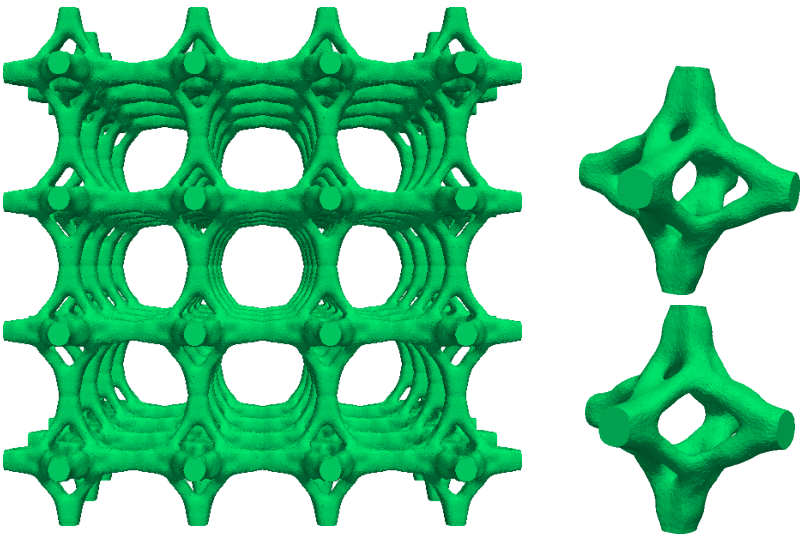

Figure 1.9: Optimized microstructures: 4×4 pattern (left), and close-ups of the reference cell (right).

Bibliography

[1] M. Ainsworth and J. T. Oden. *A Posteriori Error Estimation in Finite Element Analysis*. John Wiley & Sons, New York, 2000.

[2] G. Allaire and G. A. Francfort. "A numerical algorithm for topology and shape optimization". In: *Topology design of structures (Sesimbra, 1992)*. Vol. 227. NATO Adv. Sci. Inst. Ser. E Appl. Sci. Kluwer Acad. Publ., Dordrecht, 1993, pp. 239–248.

[3] G. Allaire, F. Jouve, and A. Toader. "Structural optimization using sensitivity analysis and level set-method". In: *J. Comput. Phys.* 194 (2004), pp. 363–393.

[4] G. Allaire and R. V. Kohn. "Optimal design for minimum weight and compliance in plane stress using extremal microstructures". In: *European J. Mech. A Solids* 12.6 (1993), pp. 839–878.

[5] G. Allaire and O. Pantz. "Structural optimization with FreeFem++". In: *Struct. Multidiscip. Optim.* 32.3 (2006), pp. 173–181.

[6] G. Allaire. *Shape Optimization by the Homogenization Method*. Vol. 146. Applied Mathematical Sciences. Springer-Verlag, New York, 2002.

[7] G. Allaire, F. Jouve, and A.-M. Toader. "A level-set method for shape optimization". In: *C. R. Math. Acad. Sci. Paris* 334.12 (2002), pp. 1125–1130.

[8] S. Amstutz. "Connections between topological sensitivity analysis and material interpolation schemes in topology optimization". In: *Struct. Multidiscip. Optim.* 43.6 (2011), pp. 755–765.

[9] I. Babuška and W. C. Rheinboldt. "Reliable error estimation and mesh adaptation for the finite element method". In: *Computational methods in nonlinear mechanics (Proc. Second Internat. Conf., Univ. Texas, Austin, Tex., 1979)*. North-Holland, Amsterdam-New York, 1980, pp. 67–108.

[10] R. Becker and R. Rannacher. "An optimal control approach to a posteriori error estimation in finite element methods". In: *Acta Numer.* 10 (2001), pp. 1–102.

[11] M. P. Bendsøe. "Optimal shape design as a material distribution problem". In: *Struct. Optimization* 1.4 (1989), pp. 193–202.

[12] M. P. Bendsøe. *Optimization of Structural Topology, Shape, and Material*. Springer-Verlag, Berlin, 1995, pp. xii+271.

[13] M. P. Bendsøe and N. Kikuchi. "Generating optimal topologies in structural design using a homogenization method". In: *Comput. Methods Appl. Mech. Engrg.* 71.2 (1988), pp. 197–224.

[14] M. P. Bendsøe and O. Sigmund. "Material interpolation schemes in topology optimization". In: *Arch. Appl. Mech.* 69.9 (1999), pp. 635–654.

[15] M. P. Bendsøe and O. Sigmund. *Topology Optimization: Theory, Methods and Applications*. Springer-Verlag, Berlin Heidelberg, 2003.

[16] D. P. Bertsekas. *Constrained optimization and Lagrange multiplier methods*. Computer Science and Applied Mathematics. Academic Press, Inc., New York-London, 1982, pp. xiii+395.

[17] C. Beyer. "Strategic implications of current trends in additive manufacturing". In: *Journal of Manufacturing Science and Engineering* 136.6 (2014).

[18] T. Borrvall and J. Petersson. "Topology optimization of fluids in Stokes flow". In: *Internat. J. Numer. Methods Fluids* 41.1 (2003), pp. 77–107.

[19] B. Bourdin and A. Chambolle. "Design-dependent loads in topology optimization". In: *ESAIM Control. Optim. Calc. Var.* 9 (2003), pp. 19–48.

[20] B. Bourdin. "Filters in topology optimization". In: *Internat. J. Numer. Methods Engrg.* 50.9 (2001), pp. 2143–2158.

[21] S. C. Brenner and L. R. Scott. *The mathematical theory of finite element methods*. Second. Vol. 15. Texts in Applied Mathematics. Springer-Verlag, New York, 2002, pp. xvi+361.

[22] M. Burger, B. Hackl, and W. Ring. "Incorporating topological derivatives into level set methods". In: *J. Comput. Phys.* 194.1 (2004), pp. 344–362.

[23] M. Burger and S. J. Osher. "A survey on level set methods for inverse problems and optimal design". In: *European J. Appl. Math.* 16.2 (2005), pp. 263–301.

[24] M. Burger and R. Stainko. "Phase-field relaxation of topology optimization with local stress constraints". In: *SIAM J. Control Optim.* 45.4 (2006), pp. 1447–1466.

[25] E. Burman et al. "Shape optimization using the cut finite element method". In: *Comput. Methods Appl. Mech. Engrg.* 328 (2018), pp. 242–261.

[26] V. J. Challis and J. K. Guest. "Level set topology optimization of fluids in Stokes flow". In: *Internat. J. Numer. Methods Engrg.* 79.10 (2009), pp. 1284–1308.

[27] L. Dedè, S. Micheletti, and S. Perotto. "Anisotropic error control for environmental applications". In: *Appl. Numer. Math.* 58.9 (2008), pp. 1320–1339.

[28] A. Díaz and O. Sigmund. "Checkerboard patterns in layout optimization". In: *Struct. Multidiscip. Optim.* 19 (1995), pp. 89–92.

[29] A. R. Díaz and M. P. Bendsøe. "Shape optimization of structures for multiple loading conditions using a homogenization method". In: *Struct. Optim.* 4.1 (1992), pp. 17–22.

[30] A. Evgrafov. "Topology optimization of slightly compressible fluids". In: *ZAMM Z. Angew. Math. Mech.* 86.1 (2006), pp. 46–62.

[31] P. E. Farrell, S. Micheletti, and S. Perotto. "An anisotropic Zienkiewicz-Zhu-type error estimator for 3D applications". In: *Int. J. Numer. Meth. Engng* 85.6 (2011), pp. 671–692.

[32] N. Ferro, S. Micheletti, and S. Perotto. *Studio, Design, Ottimizzazione Topologica ALM di Applicazione Spaziale con Metodi Matematici Innovativi Basati su Adattazione Anisotropa di Mesh*. Tech. rep. Politecnico di Milano, research contract with Thales Alenia Space, 2017.

[33] K. J. Fidkowski and D. L. Darmofal. "Review of output-based error estimation and mesh adaptation in computational fluid dynamics". In: *AIAA journal* 49.4 (2011), pp. 673–694.

[34] L. Formaggia, S. Micheletti, and S. Perotto. "Anisotropic mesh adaption with application to CFD problems". In: *Proceedings of WCCM V, Fifth World Congress on Computational Mechanics*. Ed. by H. Mang, F. Rammerstorfer, and J. Eberhardsteiner. 2002, pp. 1481–1493.

[35] L. Formaggia and S. Perotto. "New anisotropic a priori error estimates". In: *Numer. Math.* 89.4 (2001), pp. 641–667.

[36] J. Gardan. "Additive manufacturing technologies: state of the art and trends". In: *International Journal of Production Research* 54.10 (2016), pp. 3118–3132.

[37] M. J. Geiss and K. Maute. "Topology Optimization of Active Structures using a Higher-Order Level-Set-XFEM-Density Approach". In: *2018 Multidisciplinary Analysis and Optimization Conference*. 2018, p. 4053.

[38] P.-L. George and H. Borouchaki. *Delaunay Triangulation and Meshing. Application to Finite Elements*. Editions Hermès, Paris, 1998.

[39] M. Giacomini. "An equilibrated fluxes approach to the certified descent algorithm for shape optimization using conforming finite element and discontinuous Galerkin discretizations". In: *J. Sci. Comput.* 75.1 (2018), pp. 560–595.

[40] M. Giacomini, O. Pantz, and K. Trabelsi. "Certified descent algorithm for shape optimization driven by fully-computable *a posteriori* error estimators". In: *ESAIM Control Optim. Calc. Var.* 23.3 (2017), pp. 977–1001.

[41] L. J. Gibson and M. F. Ashby. *Cellular solids: structure and properties*. Cambridge university press, 1999.

[42] G. H. Golub and C. F. Van Loan. *Matrix computations*. Fourth. Johns Hopkins Studies in the Mathematical Sciences. Johns Hopkins University Press, Baltimore, MD, 2013.

[43] P. L. Gould. *Introduction to Linear Elasticity*. Springer–Verlag, New York, 1994.

[44] J. K Guest, J. H. Prevost, and T. Belytschko. "Achieving minimum length scale in topology optimization using nodal design variables and projection functions". In: *Int. J. Numer. Methods Engng* 61.2 (2004), pp. 238–254.

[45] R. Gümrük, R. Mines, and S. Karadeniz. "Static mechanical behaviours of stainless steel micro-lattice structures under different loading conditions". In: *Materials Science and Engineering: A* 586 (2013), pp. 392–406.

[46] L. Hägg and E. Wadbro. "Nonlinear filters in topology optimization: existence of solutions and efficient implementation for minimum compliance problems". In: *Struct. Multidiscip. Optim.* 55.3 (2017), pp. 1017–1028.

[47] B. Hassani and E. Hinton. "A review of homogenization and topology optimization Ihomogenization theory for media with periodic structure". In: *Computers & Structures* 69.6 (1998), pp. 707–717.

[48] W. Huang. "Variational mesh adaptation: isotropy and equidistribution". In: *J. Comput. Phys.* 174.2 (2001), pp. 903–924.

[49] W. Huang and W. Sun. "Variational mesh adaptation. II. Error estimates and monitor functions". In: *J. Comput. Phys.* 184.2 (2003), pp. 619–648.

[50] M. Kahlbacher and S. Volkwein. "Galerkin proper orthogonal decomposition methods for parameter dependent elliptic systems". In: *Discuss. Math. Differ. Incl. Control Optim.* 27.1 (2007), pp. 95–117.

[51] R. V. Kohn and G. Strang. "Optimal design and relaxation of variational problems. I". In: *Comm. Pure Appl. Math.* 39.1 (1986), pp. 113–137.

[52] R. V. Kohn and G. Strang. "Optimal design and relaxation of variational problems. II". In: *Comm. Pure Appl. Math.* 39.2 (1986), pp. 139–182.

[53] R. V. Kohn and G. Strang. "Optimal design and relaxation of variational problems. III". In: *Comm. Pure Appl. Math.* 39.3 (1986), pp. 353–377.

[54] B. S. Lazarov and O. Sigmund. "Filters in topology optimization based on Helmholtz-type differential equations". In: *Int. J. Numer. Meth. Engng* 86.6 (2011), pp. 765–781.

[55] K. A. Lurie and A. V. Cherkaev. "Effective characteristics of composite materials and the optimal design of structural elements [partial translation of MR0885713 (88e:73019)]". In: *Topics in the mathematical modelling of composite materials*. Vol. 31. Progr. Nonlinear Differential Equations Appl. Birkhäuser Boston, Boston, MA, 1997, pp. 175–258.

[56] S. Micheletti and S. Perotto. "Anisotropic adaptation via a Zienkiewicz-Zhu error estimator for 2D elliptic problems". In: *Numerical Mathematics and Advanced Applications*. Ed. by G. Kreiss et al. Springer-Verlag Berlin Heidelberg. 2010, pp. 645–653.

[57] S. Micheletti, S. Perotto, and P. E. Farrell. "A recovery-based error estimator for anisotropic mesh adaptation in CFD". In: *Bol. Soc. Esp. Mat. Apl. SeMA* 50 (2010), pp. 115–137.

[58] S. Micheletti, S. Perotto, and L. Soli. *Ottimizzazione topologica adattativa per la fabbricazione stratificata additiva*. Italian patent application No. 102016000118131, filed on November 22, 2016 (extended as *Adaptive topology optimization for additive layer manufacturing*, International patent application PCT No. PCT/IB2017/057323). 2017.

[59] S. Micheletti, S. Perotto, and L. Soli. "Topology optimization driven by anisotropic mesh adaptation: towards free-form design". Submitted.

[60] D. J. Munk, G. A. Vio, and G. P. Steven. "Topology and shape optimization methods using evolutionary algorithms: a review". In: *Struct. Multidiscip. Optim.* 52.3 (2015), pp. 613–631.

[61] L. Noël and P. Duysinx. "Shape optimization of microstructural designs subject to local stress constraints within an XFEM-level set framework". In: *Struct. Multidiscip. Optim.* 55.6 (2017), pp. 2323–2338.

[62] J. T. Oden and S. Prudhomme. "Goal-oriented error estimation and adaptivity for the finite element method". In: *Comput. Math. Appl.* 41.5-6 (2001), pp. 735–756.

[63] O. Pantz and K. Trabelsi. "A post-treatment of the homogenization method for shape optimization". In: *SIAM J. Control Optim.* 47.3 (2008), pp. 1380–1398.

[64] O. Pantz and K. Trabelsi. "Simultaneous shape, topology, and homogenized properties optimization". In: *Struct. Multidiscip. Optim.* 34.4 (2007), pp. 361–365.

[65] S. Prudhomme and J. T. Oden. "On goal-oriented error estimation for elliptic problems: application to the control of pointwise errors". In: *Comput. Methods Appl. Mech. Engrg.* 176.1-4 (1999). New advances in computational methods (Cachan, 1997), pp. 313–331.

[66] G. I. N. Rozvany. "A critical review of established methods of structural topology optimization". In: *Struct. Multidiscip. Optim.* 37 (2009), pp. 217–237.

[67] E. W. Sachs and S. Volkwein. "POD-Galerkin approximations in PDE-constrained optimization". In: *GAMM-Mitt.* 33.2 (2010), pp. 194–208.

[68] E. Sánchez-Palencia. "Homogenization in mechanics. A survey of solved and open problems". In: *Rend. Sem. Mat. Univ. Politec. Torino* 44.1 (1986), pp. 1–45.

[69] E. Sánchez-Palencia. "Homogenization method for the study of composite media". In: *Asymptotic analysis, II*. Vol. 985. Lecture Notes in Math. Springer, Berlin-New York, 1983, pp. 192–214.

[70] O. Sigmund. "Morphology-based black and white filters for topology optimization". In: *Struct. Multidiscip. Optim.* 33 (2007), pp. 401–424.

[71] O. Sigmund and J. Petersson. "Numerical instabilities in topology optimization: a survey on procedures dealing with checkerboards, mesh-dependencies and local minima". In: *Struct. Optim.* 16.1 (1998), pp. 68–75.

[72] O. Sigmund. "Materials with prescribed constitutive parameters: an inverse homogenization problem". In: *Internat. J. Solids Structures* 31.17 (1994), pp. 2313–2329.

[73] O. Sigmund. "On the usefulness of non-gradient approaches in topology optimization". In: *Struct. Multidiscip. Optim.* 43.5 (2011), pp. 589–596.

[74] O. Sigmund and K. Maute. "Topology optimization approaches, A comparative review". In: *Struct. Multidiscip. Optim.* 48.6 (2013), pp. 1031–1055.

[75] M. K. Thompson et al. "Design for Additive Manufacturing: Trends, opportunities, considerations, and constraints". In: *CIRP annals* 65.2 (2016), pp. 737–760.

[76] S. I. Valdez et al. "Topology optimization benchmarks in 2D: results for minimum compliance and minimum volume in planar stress problems". In: *Arch. Comput. Methods Eng.* 24.4 (2017), pp. 803–839.

[77] R. Verfürth. "A posteriori error estimation and adaptive mesh-refinement techniques". In: *Proceedings of the Fifth International Congress on Computational and Applied Mathematics (Leuven, 1992)*. Vol. 50. 1-3. 1994, pp. 67–83.

[78] C. H. Villanueva and K. Maute. "CutFEM topology optimization of 3D laminar incompressible flow problems". In: *Comput. Methods Appl. Mech. Engrg.* 320 (2017), pp. 444–473.

[79] M. Wallin, M. Ristinmaa, and H. Askfelt. "Optimal topologies derived from a phase-field method". In: *Struct. Multidiscip. Optim.* 45.2 (2012), pp. 171–183.

[80] M. Y. Wang and S. Zhou. "Phase field: a variational method for structural topology optimization". In: *CMES Comput. Model. Eng. Sci.* 6.6 (2004), pp. 547–566.

[81] J. Wu, A. Clausen, and O. Sigmund. "Minimum compliance topology optimization of shell-infill composites for additive manufacturing". In: *Comput. Methods Appl. Mech. Engrg.* 326 (2017), pp. 358–375.

[82] O. C. Zienkiewicz and J. Z. Zhu. "A simple error estimator and adaptive procedure for practical engineering analysis". In: *Int. J. Numer. Meth. Engng* 24 (1987), pp. 337–357.

[83] O. C. Zienkiewicz and J. Z. Zhu. "The superconvergent patch recovery and a posteriori error estimates. I: The recovery technique". In: *Int. J. Numer. Meth. Engng* 33 (1992), pp. 1331–1364.

[84] O. C. Zienkiewicz and J. Z. Zhu. "The superconvergent patch recovery and a posteriori error estimates. II: Error estimates and adaptivity". In: *Int. J. Numer. Meth. Engng* 33 (1992), pp. 1365–1382.

2

A sequential coupling of shape and topology optimization for structural design

N. Ferro, S. Micheletti, S. Perotto
Submitted to Finite Elements in Analysis and Design (under review)

2.1 Introduction

The spreading of new manufacturing technologies has prompted new paradigms for designing structures. In particular, Additive Layer Manufacturing (ALM) has allowed the production of objects without many of the geometrical and manufacturability constraints imposed by traditional technologies, such as material removal, forming and tooling. Both traditional and innovative technologies can be driven by trial-and-error or more rigorous optimization procedures which aim at identifying an optimal material distribution within a given design domain, according to prescribed requirements. This paper focuses on sophisticated mathematical methods, namely Shape Optimization and Topology Optimization (see, e.g., [3, 13, 18, 46, 48, 58, 59, 62, 63, 77]). A third possible technique is represented by Size Optimization which is,

however, not considered here, being less effective with respect to the others.

Shape and topology optimization pursue the common goal of minimizing a certain cost functional, under given constraints on mass, stiffness or other physical quantities of interest related to the application at hand. However, they work in a complementary way. Shape optimization modifies the design domain by changing its boundary, while preserving the topology; on the contrary, topology optimization allows one to change the topology of the final structure, preserving the outer boundary of the original domain but enforcing a given reduction of the mass. Thus, the final structure may have a completely different layout with respect to the starting one, including regions of void of arbitrary shape, according to a free-form design [22, 72].

In this paper, we tackle the minimum compliance problem in the linear elastic case (see, e.g., [5, 18, 65, 73]). In more detail, we seek the optimal structure, $\Omega \subset \mathbb{R}^3$, minimizing the static compliance under assigned design constraints and loads. We assume that a load, $\mathbf{f} : \Gamma_N \to \mathbb{R}^3$, is applied on a portion Γ_N of the boundary, $\partial\Omega$, of the structure. Then, the compliance is given by

$$\mathcal{G}(\mathbf{u}) = \int_{\Gamma_N} \mathbf{f} \cdot \mathbf{u}\, d\gamma,$$

with $\mathbf{u} = (u_1, u_2, u_3)^T : \Omega \to \mathbb{R}^3$ the induced displacement field. From a physical viewpoint, $\mathcal{G}$ corresponds to the work done by the external forces. The minimization of this work is equivalent to the maximization of the structure stiffness.

The linear elasticity problem represents the mathematical model underlying the structure deformation [40], and is given by

$$\begin{cases} -\nabla \cdot \sigma(\mathbf{u}) = \mathbf{0} & \text{in } \Omega \\ \mathbf{u} = \mathbf{0} & \text{on } \Gamma_D \\ \sigma(\mathbf{u})\mathbf{n} = \mathbf{f} & \text{on } \Gamma_N \\ \sigma(\mathbf{u})\mathbf{n} = \mathbf{0} & \text{on } \Gamma_F, \end{cases} \tag{2.1}$$

where $\sigma(\mathbf{u}) = 2\mu\varepsilon(\mathbf{u}) + \lambda I : \varepsilon(\mathbf{u})$ is the stress tensor for an isotropic material, with $\varepsilon(\mathbf{u}) = \big(\nabla\mathbf{u} + (\nabla\mathbf{u})^T\big)/2$ the small displacement strain tensor,

$$\lambda = \frac{E\nu}{(1+\nu)(1-2\nu)}, \quad \mu = \frac{E}{2(1+\nu)}$$

are the Lamé coefficients, with E the Young modulus, ν the Poisson ratio and I the identity tensor, $\mathbf{n}$ is the unit outward normal vector to $\partial\Omega$, Γ_D

is the portion of the boundary where homogeneous Dirichlet conditions are imposed (i.e., where the structure is clamped), and Γ_F is the normal stress-free boundary, such that $\Gamma_D \cup \Gamma_N \cup \Gamma_F = \partial\Omega$.

From a numerical viewpoint, the discretization is performed via a standard finite element technique. Hence, we derive the weak form of system (2.1),

find $\mathbf{u} \in U = \{\mathbf{v} \in [H^1(\Omega)]^3 \ : \ \mathbf{v} = \mathbf{0} \text{ on } \Gamma_D\}$, such that

$$a(\mathbf{u}, \mathbf{v}) = \mathcal{G}(\mathbf{v}) \quad \forall \mathbf{v} \in U, \tag{2.2}$$

with

$$a(\mathbf{u}, \mathbf{v}) = \int_\Omega \sigma(\mathbf{u}) : \varepsilon(\mathbf{v}) \, d\Omega, \quad \mathcal{G}(\mathbf{v}) = \int_{\Gamma_N} \mathbf{f} \cdot \mathbf{v} \, d\gamma.$$

In this work, we numerically address the structural optimization problem by means of both shape and topology optimization, highlighting pros and cons of the two techniques. In particular, in order to increase the performances of standard topology optimization algorithms, we enrich a classical density-based approach with an anisotropic mesh adaptation procedure [51, 52]. In addition to the separate analysis of the two optimization techniques, we couple them sequentially, aiming at taking advantage of their specific features (see, e.g., [28, 41, 44, 57, 71]).

The paper is organized as follows. In Section 2.2, we provide some basic elements of shape optimization, with particular attention to the definition of shape derivative and to some implementation issues. Section 2.3 is devoted to topology optimization. A standard density-based approach is presented and combined with an anisotropic mesh adaptation procedure. Then, in Section 2.4, the shape and topology optimization algorithms are combined and numerically assessed. Finally, we draw some conclusions and highlight possible future developments.

2.2 Shape optimization

Shape optimization (SO) pursues the minimization of a functional of interest, $\mathcal{J}$, through a change in the shape of the domain alone, without modifying the topology nor the volume of the initial configuration, Ω^0. Thus, the SO problem is

find $\Omega^{OPT} \in \mathcal{U}_{ad}$ such that

$$\mathcal{J}(\Omega^{OPT}) = \min_{\Omega \in \mathcal{U}_{ad}} \mathcal{J}(\Omega),$$

where $\mathcal{U}_{ad}$ is the set of all the admissible domains $\Omega \subset \mathbb{R}^3$.

We distinguish shape optimization into two categories, according to the method employed to modify the boundaries of the domain [3, 25, 56]. In particular, it is possible to express the shape in terms of a small number, N, of parameters. Hence, any modification of Ω can be represented by the variations of such parameters. In this case, we refer to the method as *parametrized shape optimization*. Although this method is easy to implement and essentially relies on solving N equations, it turns out to be little handy due to the few possible choices in varying the shape. On the contrary, *geometric shape optimization* allows more freedom since it does not restrict a priori the set of possible deformations. Following this approach, $\partial\Omega$ has to be considered as the design variable. Due to its higher flexibility, we focus on the geometric technique.

2.2.1 The shape derivative

In order to derive the SO algorithm, we briefly examine the gradient method in a Hilbert space, X, [24, 55]. In the context of the minimization of a functional, $\mathcal{J}$, the gradient method consists in updating the current design variable, $\mathbf{x}^k$, along a descent direction, $\mathbf{d}^k$, so that

$$\mathbf{x}^{k+1} = \mathbf{x}^k - \ell^k \mathbf{d}^k, \tag{2.3}$$

where $\ell^k \in \mathbb{R}^+$ properly tunes the length of the descent step. Vector $\mathbf{d}^k$ identifies the best direction to minimize the functional, and it is related to the gradient, $\mathcal{J}'$, of $\mathcal{J}$, by

$$(\mathbf{d}^k, \theta)_X = {}_{X^*}\!<\mathcal{J}', \theta>_X \quad \forall \theta \in X, \tag{2.4}$$

$(\cdot,\cdot)_X$ being the inner product in X and ${}_{X^*}\!<\cdot,\cdot>_X$ the duality pairing between X and its dual, X^*. As a result, for a suitably small step size ℓ^k, $\mathbf{d}^k$ is a descent direction and $\mathcal{J}(\mathbf{x}^{k+1}) < \mathcal{J}(\mathbf{x}^k)$.
Additionally, in the case of a functional $\mathcal{J}$ strongly convex, it holds that

$$\mathbf{x}^k \xrightarrow[k\to+\infty]{} \mathbf{x}^* = \arg\min_{\mathbf{x}\in X} \mathcal{J}(\mathbf{x}).$$

With reference to the shape optimization problem, we employ the Hadamard boundary variation method to account for modifications of the domain Ω [2, 6, 42, 63], and we endow $\mathcal{U}_{ad} \subset \mathbb{R}^3$ with a differentiable structure.
Given a vector field $\theta : \Omega \subset \mathbb{R}^3 \to \mathbb{R}^3$, $\theta \in W^{1,\infty}(\mathbb{R}^3, \mathbb{R}^3)$, a generic variation of Ω can be indicated as

$$\Omega(\theta) = (I + \theta)\Omega = \{\mathbf{x} + \theta(\mathbf{x}) | \mathbf{x} \in \Omega\}.$$

It holds

Lemma 2.2.1 *For $\theta \in W^{1,\infty}(\mathbb{R}^3, \mathbb{R}^3)$ such that $||\theta||_{W^{1,\infty}(\mathbb{R}^3,\mathbb{R}^3)} < 1$, the map $(I + \theta)$ is a Lipschitz diffeomorphism.*

A scalar function $\Omega \mapsto \mathcal{J}(\Omega) \in \mathbb{R}$ is shape differentiable at Ω if the function $\mathcal{J}_\Omega : \theta \mapsto \mathcal{J}(\Omega(\theta))$ is Fréchet-differentiable at 0, provided that $\theta \in W^{1,\infty}(\mathbb{R}^3, \mathbb{R}^3)$ and Ω is a smooth domain. In particular,

$$\mathcal{J}(\Omega(\theta)) = \mathcal{J}(\Omega) + \mathcal{J}'(\Omega)(\theta) + o(||\theta||_{W^{1,\infty}(\mathbb{R}^3,\mathbb{R}^3)}).$$

We refer to the linear mapping $\theta \mapsto \mathcal{J}'(\Omega)(\theta)$ as to the *shape derivative* of $\mathcal{J}$ at Ω [2, 6, 42, 63]. Then, the descent direction, $\mathbf{d}$, is the function in $[H^1(\Omega)]^3$ corresponding to the gradient $\mathcal{J}'$ and is computed by solving (2.4) with $X = [H^1(\Omega)]^3$ endowed with the standard scalar product [6]. Consequently, the descent direction $\mathbf{d}$ is the unique solution to the following boundary value problem,

find $\mathbf{d} \in [H^1(\Omega)]^3$ such that

$$\int_\Omega (\nabla \mathbf{d} \cdot \nabla \theta + \mathbf{d} \cdot \theta) d\Omega = {}_{X^*}\!<\mathcal{J}', \theta>_X \quad \forall \theta \in [H^1(\Omega)]^3,$$

$(\cdot, \cdot)$ being the standard inner product in $[H^1(\Omega)]^3$.

The shape derivative in the minimum compliance problem

We define $\mathcal{U}_{ad} = \{A \subset \mathbb{R}^3 \,|\, \Gamma_N \cup \Gamma_D \subset \partial A, |A| = V_0\}$, with $|\cdot|$ the measure of an open set and V_0 a prescribed volume for the admissible shape.
Thus, the definition of shape derivative for the minimum compliance problem can be formulated.

Proposition 2.2.1 *Let Ω be a smooth bounded open set in $\mathbb{R}^3$ and $\theta \in [H^1(\Omega)]^3$ and assume that the solution to (2.1) belongs to $[H^2(\Omega)]^3$. Then, the shape derivative of $\mathcal{G}(\Omega)$ is*

$$_{X^*} < \mathcal{G}'(\Omega), \theta >_X = -\int_{\Gamma_F} \left[2\mu\|\epsilon(\boldsymbol{u})\|^2 + \lambda[\nabla \cdot \boldsymbol{u}]^2\right](\theta \cdot \boldsymbol{n})d\gamma,$$

where Γ_F is the portion of the boundary allowed to change and $\|\cdot\|$ denotes the tensor norm.

We define the set $\mathcal{D} = \{\delta \in [H^1(\Omega)]^3 |\ \delta = 0 \text{ on } \Gamma_D \cup \Gamma_N\}$ of the possible descent directions [4, 6]. Then, the optimal descent direction for the gradient method solves the problem

find $\mathbf{d} \in \mathcal{D}$ such that

$$\begin{aligned}&\int_\Omega (\nabla \mathbf{d} \cdot \nabla\theta + \mathbf{d} \cdot \theta)d\Omega = \\ &-\int_{\Gamma_F} \left[(2\mu\|\epsilon(\mathbf{u})\|^2) + \lambda[\nabla \cdot \mathbf{u}]^2\right](\theta \cdot \mathbf{n})d\gamma \quad \forall\theta \in \mathcal{D}.\end{aligned} \tag{2.5}$$

2.2.2 Numerical implementation

For numerical purposes, the SO algorithm is implemented in a finite element code. The discretization is performed on a mesh, $\mathcal{T}_h$, composed by regular tetrahedra and we employ Lagrangian finite elements [26]. Via Galerkin projection, equations (2.2) and (2.5) are discretized, yielding

find $\mathbf{u}_h \in U_h^s$, such that

$$a(\mathbf{u}_h, \mathbf{v}_h) = \mathcal{G}(\mathbf{v}_h) \quad \forall \mathbf{v}_h \in U_h^s, \tag{2.6}$$

for the linear elasticity equation, and

find $\mathbf{d}_h \in \mathcal{D}_h^m$ such that

$$\begin{aligned}&\int_\Omega (\nabla \mathbf{d}_h \cdot \nabla\theta_h + \mathbf{d}_h \cdot \theta_h)d\Omega = \\ &-\int_{\Gamma_F} \left[(2\mu\|\epsilon(\mathbf{u}_h)\|^2) + \lambda[\nabla \cdot \mathbf{u}_h]^2\right](\theta_h \cdot \mathbf{n})d\gamma \quad \forall\theta_h \in \mathcal{D}_h^m,\end{aligned} \tag{2.7}$$

for the descent direction computation, where U_h^s and $\mathcal{D}_h^m$ denotes the finite element subspace of U and $\mathcal{D}$ and of degree s and m, respectively. In particular, in the numerical assessment in Section 2.2.3, we choose $s = m = 1$.

The constraint for the volume is enforced using a Lagrangian approach [6, 8]. We require that the volume, V_0, of the initial domain Ω^0 is preserved in the optimization iterations. To this end, we introduce a positive Lagrange multiplier, ϕ, so that the Lagrangian is

$$\tilde{\mathcal{G}}(\Omega) = \mathcal{G}(\Omega) + \phi\,(V(\Omega) - V_0)\,,$$

where $V(\Omega)$ denotes the volume of the current shape Ω, while ϕ enforces the constraint in a weak sense, and it is changed at each iteration by considering the optimality condition, $\mathcal{G}'(\Omega)+\bar{\phi}V'(\Omega) = 0$, understood in an average sense on the boundary of Ω, solved for $\bar{\phi}$. Following [6], at the k-th iteration, ϕ^{k+1} is thus updated as

$$\phi^{k+1} = \frac{\phi^k + \bar{\phi}}{2} + \varepsilon_\phi \frac{V(\Omega) - V_0}{V_0}, \tag{2.8}$$

where ε_ϕ is a positive real number, set to 2 in the simulations below.

As far as the update of the computational domain is concerned, we employ rule (2.3) after identifying the vector $\mathbf{x}^k$ with the vector collecting all of the coordinates of mesh vertices and picking ℓ^k so that functional $\mathcal{G}$ is minimized and no element inversion occurs [58]. We enrich these criteria with the following additional strategy: if $(\mathbf{d}_h^{k+1}, \mathbf{d}_h^k) > 0$, namely two consecutive descent directions are, in some sense, close, we are allowed to choose $\ell^{k+1} > \ell^k$, without compromising the procedure. Conversely, if $(\mathbf{d}_h^{k+1}, \mathbf{d}_h^k) < 0$, the step size is reduced to avoid oscillations in the convergence history. Eventually, a regularization loop over the elements completes the whole process.

The complete procedure is provided in Algorithm 1.

The input parameters to the algorithm are: `kmax` for the maximum number of iterations allowed for the gradient method, Δ_{BEST} a safety factor used to reasonably ensuring convergence to a minimum, $\mathcal{T}_h^0$ the initial mesh, and V_0 for the volume constraint. In lines 6 and 9, `movemesh` is the routine employed to update the current mesh, whereas `regularize` in line 10 performs the tetrahedra regularization. Algorithm 1 has been implemented in the FreeFem++ environment [43].

2.2.3 Numerical assessment for SO

We carry out three test cases, i.e., the bridge, the cantilever beam, and the dome. In Figures 2.1, 2.3, 2.5, the domain Ω^0 and the load are sketched. In

Algorithm 1 Shape Optimization (SO)

Input : $\texttt{kmax}$, Δ_{BEST}, $\mathcal{T}_h^0$, V_0

1: Set: $\texttt{k} = 0$, $\texttt{k}_{BEST} = 0$, $\mathcal{T}_{BEST} = \mathcal{T}_h^0$, $\mathcal{G}_{BEST} = \mathcal{G}(\Omega^0)$;
2: **while** $\texttt{k} - \texttt{k}_{BEST} < \Delta_{BEST}$ & $\texttt{k} < \texttt{kmax}$ **do**
3: Solve (2.6);
4: Solve (2.7);
5: Compute $\phi^{\texttt{k}}$, $\ell^{\texttt{k}}$;
6: $\mathcal{T}_h^{\texttt{k}+1} = \texttt{movemesh}(\mathcal{T}_h^{\texttt{k}}, \mathbf{d}_h^{\texttt{k}}, \ell^{\texttt{k}})$;
7: **while** $\mathcal{T}_h^{\texttt{k}+1}$ has degenerate elements **do**
8: Reduce $\ell^{\texttt{k}}$;
9: $\mathcal{T}_h^{\texttt{k}+1} = \texttt{movemesh}(\mathcal{T}_h^{\texttt{k}}, \mathbf{d}_h^{\texttt{k}}, \ell^{\texttt{k}})$;
10: $\mathcal{T}_h^{\texttt{k}+1} = \texttt{regularize}(\mathcal{T}_h^{\texttt{k}+1})$;
11: Compute $\mathcal{G}(\Omega)$;
12: **if** $\mathcal{G}(\Omega) < \mathcal{G}_{BEST}$ **then**
13: $\mathcal{G}_{BEST} = \mathcal{G}(\Omega)$;
14: $\texttt{k}_{BEST} = \texttt{k} + 1$;
15: $\mathcal{T}_{BEST} = \mathcal{T}_h^{\texttt{k}+1}$;
16: $\texttt{k} = \texttt{k} + 1$;

particular, we mark with a triangle the portions of surface corresponding to Γ_D, while Γ_N is enclosed within the white boxes. The red arrows indicate the directions of the applied load. In Table 2.1, we collect the physical parameters used to describe the homogeneous employed materials.

Test case	E [GPa]	ν [-]
Bridge	15	1/3
Cantilever beam	1.0	1/3
Dome	1.0	1/3

Table 2.1: Physical parameters employed in the SO simulations.

Concerning parameters $\texttt{kmax}$ and Δ_{BEST} of Algorithm 1, we set $\texttt{kmax} = 300$ and $\Delta_{BEST} = 5$ in all the test cases.

The bridge test case

We consider the optimization of a simplified bridge, modeled starting from a parallelepiped 6 [m] $\times 1$ [m] $\times 1$ [m] clamped in four portions of the bottom surface of size 0.01 [m] $\times 0.01$ [m] each (see Figure 2.1, right). The surface load $\mathbf{f} = [0, 0, -1]^T$ is applied onto the rectangular surface 1 [m] $\times 0.1$ [m] located at the center of the upper face (see Figure 2.1, center). The domain Ω^0 is discretized using a tetrahedral mesh composed by 25869 elements.

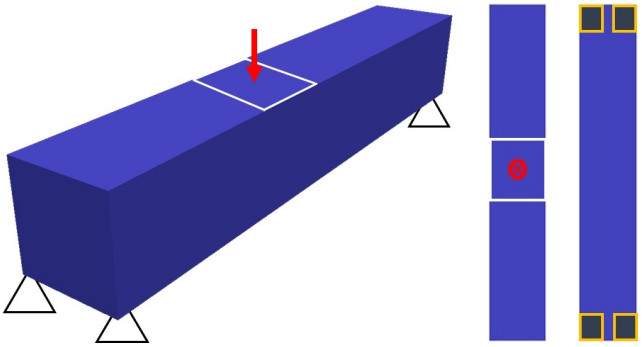

Figure 2.1: The bridge test case (SO): geometry and boundary conditions (left); details of the top surface, with highlighted Γ_N (white box) and the direction of the load (red marker) (center); details of the bottom surface with highlighted Γ_D (yellow boxes) (right).

In Figure 2.2, the output of the Algorithm 1 is shown at the convergence iteration $\mathtt{k} = 33$. The optimized structure preserves the portions Γ_N and Γ_D, as expected and the symmetry of the original configuration.

In Table 2.2, we collect the value of the compliance for the initial domain and for the optimal structure, and the decreasing percentage of $\mathcal{G}$. The same comparison is carried out on the volume, to assess its conservation. We observe a remarkable reduction of $\mathcal{G}$ and an almost exact volume conservation.

The cantilever beam test case

We deal with the optimization of a cantilever beam starting from the parallelepiped 2 [m] $\times 1$ [m] $\times 0.5$ [m] in Figure 2.3. The entire back face corresponds to Γ_D, Γ_N is a square of side 0.1 [m] centered at the centroid of the

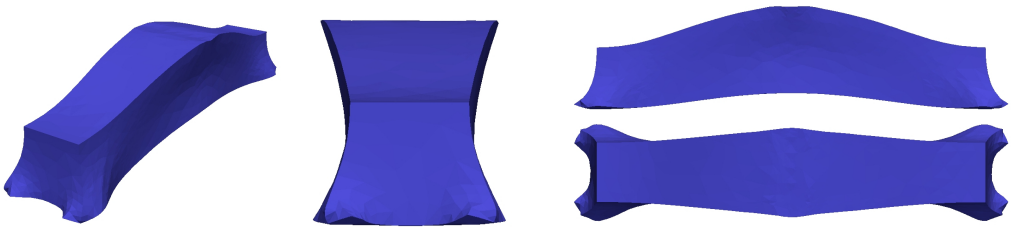

Figure 2.2: The bridge test case (SO): optimized structure (left), lateral (center), frontal (top-right) and top (bottom-right) views of the optimized structure.

Compliance		
$\mathcal{G}$ before SO	0.0933	[J]
$\mathcal{G}$ after SO	0.0796	[J]
$\Delta_{\%}\mathcal{G}$	-14.68%	[-]

Volume		
V_0	6.000	[m^3]
V after SO	5.999	[m^3]
$\Delta_{\%}V$	-0.017%	[-]

Table 2.2: The bridge test case (SO): compliance and volume before and after SO.

frontal face, and the load $\mathbf{f} = [0, 0, -1]^T$ is tangential to the frontal face. The initial mesh consists of 5870 tetrahedra.

The result of the optimization is shown in Figure 2.4 after 113 iterations of Algorithm 1. The shape of the new structure is quite different with respect to Ω^0, being more slender in correspondence with the frontal face with respect to the clamped surface. The symmetry is still preserved. From a quantitative viewpoint, Table 2.3 summarizes the compliance and the volume before and after the optimization. In this case, the stiffness of the structure improves strongly, the compliance being reduced of 2/3. Additionaly, also the volume constraint is ensured.

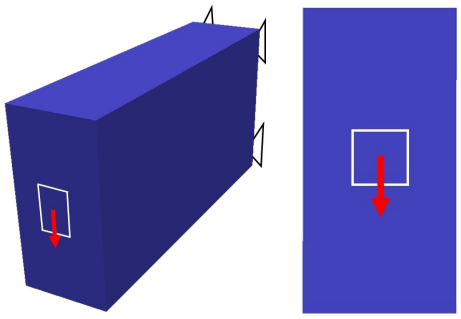

Figure 2.3: The cantilever beam test case (SO): geometry and boundary conditions (left) and frontal surface (right), with highlighted Γ_N (white box) and the direction of the load (red arrow); the triangles identify Γ_D.

Figure 2.4: The cantilever test case (SO): optimized structure (left), lateral (center), frontal (top-right) and top (bottom-right) views of the optimized structure.

The dome test case

The geometry in Figure 2.5 is the result of the intersection between a hemispheric shell of radius 1.25 [m], thickness 0.02 [m] and clamped at the bottom, with a circular cylinder of radius 0.25 [m]. Boundary Γ_N is a portion of the upper surface, concentric to the hole, with radius $0.25 + 0.0314$ [m], and the load is $\mathbf{f} = [0, 0, -1]^T$. The initial spatial discretizion is based on a mesh with 83428 elements.

We run Algorithm 1 which stops after 198 iterations. The resulting optimized structure is shown in Figure 2.6. Notice that the initial shape has

Compliance		
$\mathcal{G}$ before SO	0.0309	[J]
$\mathcal{G}$ after SO	0.0104	[J]
$\Delta_{\%}\mathcal{G}$	-66.34%	[-]

Volume		
V_0	1.000	[m^3]
V after SO	1.000	[m^3]
$\Delta_{\%}V$	0.0%	[-]

Table 2.3: The cantilever beam test case (SO): compliance and volume before and after SO.

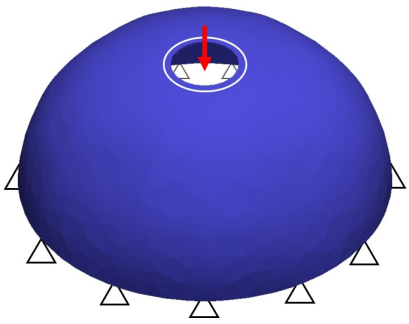

Figure 2.5: The dome test case (SO): geometry and boundary conditions, with highlighted Γ_N (white circular box) and the direction of the load (red arrow); the triangles identify Γ_D.

undergone a sort of squeezing in the vertical direction.

Table 2.4 collects the values obtained for the compliance and the volume, confirming an enhancement of the mechanical performance of the optimized structure with respect to the original shape.

2.3 Topology optimization and the SIMP method

One of the most employed mathematical models for topology optimization (TO) is the SIMP (Solid Isotropic Material with Penalization) [10, 14, 15, 17, 18]. Other approaches exploit level set methods (see, e.g., [8, 21, 23, 70]),

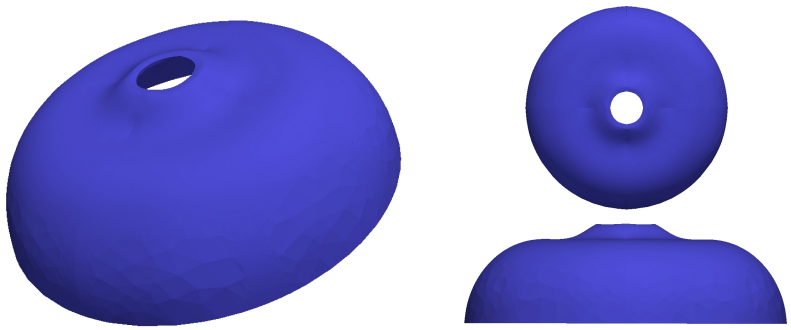

Figure 2.6: The dome test case (SO): lateral (left), top (top-right) and frontal (bottom-right) views of the optimized structure.

Compliance		
$\mathcal{G}$ before SO	7.1654	[J]
$\mathcal{G}$ after SO	3.2433	[J]
$\Delta_{\%}\mathcal{G}$	-54.74%	[-]

Volume		
V_0	0.05256	[m^3]
V after SO	0.05231	[m^3]
$\Delta_{\%}V$	-0.478%	[-]

Table 2.4: The dome test case (SO): compliance and volume before and after SO.

homogeneization (see, e.g., [7, 16, 32]), a phase field formulation (see, e.g., [19, 29, 36]), gradient-free methods (see, e.g., [54, 61]), high order discretizations (see, e.g., [39, 60]), cutFEM (see, e.g., [67]) and volumetric expressions of the shape gradient (see, e.g., [38]).

SIMP method is based on an auxiliary variable, ρ, which models the material distribution in the original design domain. In particular, the density function, $\rho \in L^\infty(\Omega)$, takes values in $[0, 1]$, where $\rho = 0$ corresponds to the void, whereas $\rho = 1$ identifies the presence of full material. Nevertheless, all the intermediate values in the interval $[0, 1]$ are allowed and for this reason a suitable penalization has to be introduced to push the density to the extremal values, 0 and 1. Thus, the stiffest material and the void are

favoured, consistently with the maximization of the structure stiffness. To this end, we employ the standard power law penalization function ρ^p, with $p \geq \max\left\{2/(1-\nu), 4/(1+\nu)\right\}$ [10, 18].

In the minimum compliance framework, model (2.1) represents the state equation for the optimization problem, after taking into account the material density. In particular, according to the SIMP approach, we solve model (2.1) with a modified Hooke law with $\rho^p\lambda$ and $\rho^p\mu$ replacing λ and μ, respectively. Thus, the weak form of the SIMP-linear elasticity equation is

find $\mathbf{u} \in U$ such that

$$a_\rho(\mathbf{u}, \mathbf{v}) = \mathcal{G}(\mathbf{v}) \quad \forall \mathbf{v} \in U, \tag{2.9}$$

with

$$a_\rho(\mathbf{u}, \mathbf{v}) = \int_\Omega \sigma_\rho(\mathbf{u}) : \varepsilon(\mathbf{v})\, d\Omega,$$

and $\sigma_\rho(\mathbf{u}) = \rho^p\big[2\mu\varepsilon(\mathbf{u}) + \lambda I : \varepsilon(\mathbf{u})\big]$. Notice that $\mathcal{G}(\mathbf{u}) = a_\rho(\mathbf{u}, \mathbf{u})$ still represents the static compliance, i.e., the functional to be minimized.
The topology optimization problem finally becomes

find $\rho \in L^\infty(\Omega)$ such that

$$\min_{\rho \in L^\infty(\Omega)} \mathcal{G}(\mathbf{u}(\rho)) \ : \begin{cases} a_\rho(\mathbf{u}(\rho), \mathbf{v}) = \mathcal{G}(\mathbf{v}) \ \forall \mathbf{v} \in U \\ \int_\Omega \rho\, d\Omega \leq \alpha|\Omega| \\ \rho_{\min} \leq \rho \leq 1, \end{cases} \tag{2.10}$$

where $0 < \alpha < 1$ denotes the maximum allowable volume fraction and $0 < \rho_{\min} < 1$ is a lower bound for the density, which ensures the elasticity system to be well-defined.

Problem (2.10) is numerically tackled via a standard finite element discretization. The discrete counterpart of (2.10) becomes

find $\rho_h \in V_h^r$ such that

$$\min_{\rho_h \in V_h^r} \mathcal{G}(\mathbf{u}_h(\rho_h)) \ : \begin{cases} a_\rho(\mathbf{u}_h(\rho_h), \mathbf{v}_h) = \mathcal{G}(\mathbf{v}_h) \ \forall \mathbf{v}_h \in U_h^s \\ \int_\Omega \rho_h\, d\Omega \leq \alpha|\Omega| \\ \rho_{\min} \leq \rho_h \leq 1, \end{cases} \tag{2.11}$$

where it is understood that $\mathbf{u}_h(\rho_h) \in U_h^s$ and V_h^r is the finite element space of scalar functions of degree r.

Formulation (2.11) suffers from two numerical issues, namely the dependence of the final topology on the mesh and the checkerboard effect [18, 31,

60]. The former is linked to the non-uniqueness of the solution to problems (2.10) and (2.11). To this end, it is possible to consider additional constraints, for instance a limitation on the perimeter of the structure [9]. The checkerboard effect strongly depends on the discretization pair adopted for the density-displacement formulation. Some combinations of finite elements might be unstable, as in the case of the two-field pressure-velocity formulation of the Stokes problem. It may result in material/void alternation as in a checkerboard, leading to non-manufacturable designs (for additional comments see [52]).

A partial remedy to both mesh dependence and checkerboard effect is to filter the density ρ, with smoothing techniques. Alternatively, it is possible to use higher order finite elements for the displacement with respect to the density ($s \geq r$ in (2.11)) to tackle the checkerboard issue. However, high order finite elements require a bigger computational effort and this choice may be unaffordable for three dimensional simulations.

As an alternative to these remedies, since the optimized density obtained by the SIMP method exhibits strong gradients in correspondence with the boundaries of the structure (i.e., along the void-material interface), it has been proposed an enrichment of the standard SIMP algorithm with a mesh adaptation strategy in [52]. Among the benefits characterizing this new approach, we mention the possibility to use low degree finite element spaces for both ρ_h and $\mathbf{u}_h$ (i.e., $s = r = 1$) and to avoid a massive employment of filtering, thus containing the computational cost and the post-processing. In particular, we limit the filtering to the very first optimization iteration, when a low-pass filter based on the diffusion kernel is adopted. For this purpose, we replace the density ρ_h with its filtered version, ρ_f, solution to the Helmholtz-type problem

$$\begin{cases} -\tau^2 \Delta \rho_f + \rho_f = \rho_h & \text{in } \Omega \\ \tau^2 \nabla \rho_f \cdot \mathbf{n} = 0 & \text{on } \partial\Omega, \end{cases} \tag{2.12}$$

with τ a real parameter that measures the characteristic length of the smoothed density [47].

The algorithm merging the SIMP method with the Helmholtz filter for the density is provided in Algorithm 2 [52].

Algorithm 2 SIMP algorithm on a fixed grid

Input : `CTOL`, `kmax`, $\rho_{\min}$

1: Set: $\rho_h^0 = 1$, $\mathtt{k} = 0$, errG = 1+`CTOL`
2: **while** errG > `CTOL` & k < `kmax` **do**
3: $\quad \rho_h^{\mathtt{k}+1} = \mathtt{optimize}(\rho_h^{\mathtt{k}}, \mathtt{Mit}, \mathtt{TOPT}, \nabla_\rho \mathcal{G}, ...)$;
4: $\quad \rho_h^{\mathtt{k}+1} = \rho_f(\rho_h^{\mathtt{k}+1})$;
5: $\quad \text{errG} = \|\rho_h^{\mathtt{k}+1} - \rho_h^{\mathtt{k}}\|_\infty$;
6: $\quad \mathtt{k} = \mathtt{k} + 1$;

Some comments are in order. The main input parameters are the lower value, $\rho_{\min}$, for the density, the maximum number, `kmax`, of iterations and the tolerance `CTOL` for the stopping criterion. In line 3, problem (2.11) is solved via an optimization routine, i.e., `optimize`. In particular, we employ the Interior Point OPTimizer (IPOPT) package [69], but other options are viable, such as the MMA algorithm [64]. IPOPT is a common large-scale nonlinear optimization tool based on the interior point algorithm [68]. Both equality and inequality constraints can be tackled via suitable slack variables. Constraints may involve both the control variables (for example, the density ρ) as well as functions of these (for instance, the total volume of the structure, $\int_\Omega \rho d\Omega$). Among the input parameters of `optimize`, `Mit` identifies the maximum number of iterations allowed and `TOPT` is the tolerance for the adopted stopping criterion. The computation of the gradient, $\nabla_\rho \mathcal{G}$, of the compliance with respect to the density has to be provided as well. With this aim, we introduce the Lagrangian functional

$$\mathcal{L} = \mathcal{L}(\mathbf{u}, \mathbf{z}, \rho) = \mathcal{G}(\mathbf{u}) + a_\rho(\mathbf{u}, \mathbf{z}) - \mathcal{G}(\mathbf{z}),$$

where $\mathbf{z} \in U$ is the Lagrange multiplier. It is well known that

$$\nabla_\rho \mathcal{G}(\rho) = \nabla_\rho \mathcal{L}\big|_{\mathbf{u}(\rho),\mathbf{z}(\rho),\rho},$$

where $\mathbf{u}(\rho)$ and $\mathbf{z}(\rho)$ are the solutions to the primal and adjoint problem associated with the Gâteaux derivative of $\mathcal{L}$ with respect to $\mathbf{z}$ and $\mathbf{u}$, respectively. In particular, the primal problem coincides with (2.9), whereas the adjoint problem is

find $\mathbf{z} \in U$ such that

$$a_\rho(\mathbf{v}, \mathbf{z}) = -\mathcal{G}(\mathbf{v}) \quad \forall \mathbf{v} \in U. \tag{2.13}$$

On comparing (2.13) with (2.9) and due to the self-adjointness of $a_\rho(\cdot,\cdot)$, we infer that $\mathbf{z} = -\mathbf{u}$, that is we have a cost-free adjoint solution. Finally, the Gâteaux derivative of $\mathcal{L}$ with respect to ρ along the direction $\psi \in U$ is

$$\int_\Omega p\,\rho^{p-1}\sigma(\mathbf{u}) : \varepsilon(\mathbf{z})\psi\, d\Omega = \langle \nabla_\rho \mathcal{G}, \psi \rangle,$$

implying

$$\nabla_\rho \mathcal{G}(\rho) = -p\,\rho^{p-1}\sigma(\mathbf{u}(\rho)) : \varepsilon(\mathbf{u}(\rho)). \tag{2.14}$$

Thus, each evaluation of the gradient of the compliance requires only a primal solve and the computation of (2.14).

The output density $\rho_h^{\mathtt{k+1}}$ from `optimize` is then filtered in line 4 by approximating (2.12) via linear finite elements. The global convergence check in line 5 is based on the difference between two successive iterations of the density with respect to the $L^\infty(\Omega)$-norm.

Other strategies can be adopted as an alternative to Algorithm 2, for example procedures where a more frequent use of the filters inside the optimization routine occurs and/or where $\nabla_\rho \mathcal{G}$ is smoothed as well [20, 45].

2.3.1 SIMP enriched with anisotropy

To manufacture smooth structures, a sufficiently fine mesh or a heavy density filtering are usually adopted. However, both these choices are often very demanding in terms of computational cost. In [52], the authors propose combining the SIMP procedure with an anisotropic adaptation of the mesh as a computationally efficient alternative. In fact, anisotropic mesh adaptation allows us to reduce the employment of a filter, the optimized structure being intrinsically smooth. This goal is reached by resorting to a rigorous mathematical tool, i.e., an a posteriori error estimator used to generate the anisotropic adapted mesh.

The anisotropic framework

We refer to the setting in [30, 33, 35, 50], where the geometric properties of a generic tetrahedron K are extracted from the spectral properties of the standard affine transformation T_K, which maps the reference element $\widehat{K}$ inscribed in the unit sphere into K, such that

$$\mathbf{x} = T_K(\hat{\mathbf{x}}) = M_K\hat{\mathbf{x}} + \mathbf{t}_K,$$

with $\mathbf{x} \in K$, $\hat{\mathbf{x}} \in \widehat{K}$, $M_K \in \mathbb{R}^{3\times 3}$, $\mathbf{t}_K \in \mathbb{R}^3$. Through T_K, the unit sphere is transformed into an ellipsoid circumscribing K. By means of the polar decomposition, M_K is factorized as the product $B_K Z_K$, with $B_K \in \mathbb{R}^{3\times 3}$ a symmetric positive definite matrix taking into account the deformation of the element K, and $Z_K \in \mathbb{R}^{3\times 3}$ an orthogonal matrix rigidly rotating K. Matrix B_K can be decomposed in terms of the corresponding eigenvalues and eigenvectors, leading to $B_K = R_K^T \Lambda_K R_K$, with $R_K^T = [\mathbf{r}_{1,K}, \mathbf{r}_{2,K}, \mathbf{r}_{3,K}]$ and $\Lambda_K = \mathrm{diag}(\lambda_{1,K}, \lambda_{2,K}, \lambda_{3,K})$, with $\lambda_{1,K} \geq \lambda_{2,K} \geq \lambda_{3,K}$. Matrices R_K^T and Λ_K collect all the geometric features of element K. In particular, the eigenvectors $\mathbf{r}_{1,K}$, $\mathbf{r}_{2,K}$ and $\mathbf{r}_{3,K}$ represent the directions of the semi-axes of the ellipsoid circumscribed to K, while the eigenvalues $\lambda_{1,K}$, $\lambda_{2,K}$ and $\lambda_{3,K}$ measure the length of the semi-axes. It is possible to introduce the aspect ratios of the element K,

$$s_{i,K} = \left(\frac{\lambda_{i,K}^2}{\prod_{j\neq i} \lambda_{j,K}} \right)^{2/3}, \quad i = 1, 2, 3,$$

which quantify the anisotropic features of K. Notice that $s_{1,K} \geq s_{2,K} \geq s_{3,K}$ and $s_{1,K} s_{2,K} s_{3,K} = 1$, the isotropic case coinciding with $s_{1,K} = s_{2,K} = s_{3,K} = 1$.

The error estimator

Among the possible a posteriori error estimators available in the literature [1, 12, 66], we resort to a recovery-based analysis [74, 75, 76] which consists of two steps, i.e., the computation of the recovered gradient and the successive definition of the estimator. In [49, 50], an extension of this approach to an anisotropic setting has been proposed for the first time. The recipe adopted for the recovered gradient is

$$P(\nabla u_h)\big|_{\Delta_K} = \frac{1}{|\Delta_K|} \sum_{T\in\Delta_K} |T|\, \nabla u_h|_T,$$

where $\Delta_K = \{T \in \mathcal{T}_h : T \cap K \neq \emptyset\}$ is the patch of elements associated with K. We remark that $P(\nabla u_h)$ is piecewise constant on $\mathcal{T}_h$, differently from the piecewise linear gradient reconstruction adopted in the papers by

O.C. Zienkiewicz and J.Z. Zhu. A generalization of $P(\nabla u_h)$ to higher degree reconstructions can be found in [49, 50].

Then, the anisotropic a posteriori error estimator is

$$\eta^2 = \sum_{K\in\mathcal{T}_h} \eta_K^2, \tag{2.15}$$

where the local contribution η_K is

$$\eta_K^2 = \frac{1}{\left(\lambda_{1,K}\lambda_{2,K}\lambda_{3,K}\right)^{2/3}} \sum_{i=1}^{3} \lambda_{i,K}^2 \left(\mathbf{r}_{i,K}^T\, G_{\Delta_K}\big(E_\nabla\big)\mathbf{r}_{i,K}\right), \tag{2.16}$$

where $E_\nabla = \big[P(\nabla u_h) - \nabla u_h\big]_{\Delta_K}$ is the recovered error, and $G_{\Delta_K}(\cdot) \in \mathbb{R}^{3\times 3}$ is the symmetric positive semidefinite matrix with entries

$$[G_{\Delta_K}(\mathbf{w})]_{i,j} = \sum_{T\in\Delta_K} \int_T w_i\, w_j\, dT \quad \text{with } i,j = 1,2,3, \tag{2.17}$$

for any vector-valued function $\mathbf{w} = (w_1, w_2, w_3)^T \in [L^2(\Omega)]^3$. The scaling factor $\left(\lambda_{1,K}\lambda_{2,K}\lambda_{3,K}\right)^{-2/3}$ in (2.16) ensures the consistency with respect to the isotropic case (i.e., for $\lambda_{1,K} = \lambda_{2,K} = \lambda_{3,K}$).

The SIMPATY algorithm

We resort to a metric-based approach to generate the adapted mesh, by exploting the information contained in η. In more detail, a metric, $\mathcal{M} : \Omega \to \mathbb{R}^{3\times 3}$, is a symmetric positive definite tensor field which contains all the geometric information related to a certain mesh [37]. In a finite element setting, we approximate $\mathcal{M}$ by a piecewise constant function, $\mathcal{M}_{\mathcal{T}_h}$, associated with the actual grid $\mathcal{T}_h$, such that $\mathcal{M}_{\mathcal{T}_h}\big|_K = R_K^T \Lambda_K^{-2} R_K$, consistently with the notation introduced in Section 2.3.1.

We use the local estimator η_K in a predictive way to define a new metric field. This goal is reached via an iterative procedure which, eventually, yields an optimal adapted grid satisfying the two criteria: i) minimization of the number of elements under the accuracy constraint, $\eta \leq \texttt{MTOL}$, with MTOL a user-defined tolerance; ii) error equidistribution, namely, $\eta_K^2 = \texttt{MTOL}^2/\#\mathcal{T}_h$, with $\#\mathcal{T}_h$ the mesh cardinality.

Now, we sketch the procedure adopted for the prediction of the metric out of the estimator, while referring to, e.g., [33, 50] for more details.

With reference to the generic k-th iteration of Algorithm 2, we rewrite estimator η_K by collecting the size information of the patch in a single factor, $|\Delta_K|$, as

$$\eta_K^2 = |\Delta_K| \underbrace{\sum_{i=1}^{3} s_{i,K} \left(\mathbf{r}_{i,K}^T \, \widehat{G}_{\Delta_K}(E_\nabla) \, \mathbf{r}_{i,K} \right)}_{\mathcal{F}(\{s_{i,K}, \mathbf{r}_{i,K}\}_{i=1,2,3})},$$

where $\widehat{G}_{\Delta_K}(\cdot)$ is the scaled matrix $G_{\Delta_K}(\cdot)/|\Delta_K|$, and $|\Delta_K| = \lambda_{1,K}\lambda_{2,K}\lambda_{3,K}\,|\widehat{\Delta}_K|$, with $\widehat{\Delta}_K = T_K^{-1}(\Delta_K)$. Notice that $|\Delta_K|$ is the main quantity related to the volume of the tetrahedra, the other terms keeping track of the orientation and of the stretching of K.

Minimizing the cardinality of the mesh is equivalent to maximizing the size of the patch, so that we are led to solve the constrained minimization problem

$$\min_{s_{i,K}, \mathbf{r}_{i,K}} \mathcal{F}(\{s_{i,K}, \mathbf{r}_{i,K}\}_{i=1,2,3}) \; : \begin{cases} \mathbf{r}_{i,K} \cdot \mathbf{r}_{j,K} = \delta_{ij} \\ s_{1,K} \geq s_{2,K} \geq s_{3,K} \\ s_{1,K} s_{2,K} s_{3,K} = 1, \end{cases} \tag{2.18}$$

with δ_{ij} the Kronecker symbol and $i, j = 1, 2, 3$. This problem has an explicit solution provided in [33, 50] and stated in the following

Proposition 2.3.1 *Let $\{g_i, \mathbf{g}_i\}_{i=1,2,3}$ be the eigenpairs associated with $\widehat{G}_{\Delta_K}(E_\nabla)$, with $g_1 \geq g_2 \geq g_3 > 0$ and $\{\mathbf{g}_i\}_{i=1,2,3}$ orthonormal. Then, $\mathcal{F}(\cdot)$ is minimized when*

$$s_{1,K} = \frac{\sqrt[3]{\Pi_{i=1}^3 g_i}}{g_3}, \quad s_{2,K} = \frac{\sqrt[3]{\Pi_{i=1}^3 g_i}}{g_2}, \quad s_{3,K} = \frac{\sqrt[3]{\Pi_{i=1}^3 g_i}}{g_1},$$
$$\mathbf{r}_{1,K} = \mathbf{g}_3, \quad \mathbf{r}_{2,K} = \mathbf{g}_2, \quad \mathbf{r}_{3,K} = \mathbf{g}_1.$$

Next, by employing the equidistribution criterion, the optimal values for length $\lambda_{i,K}$ can be computed as

$$\lambda_{1,K} = g_3^{-1/2} \left(\frac{\texttt{MTOL}^2}{3\,\#\mathcal{T}_h |\widehat{\Delta}_K|} \right)^{1/3} \Big(\prod_{i=1}^{3} g_i \Big)^{1/18},$$
$$\lambda_{2,K} = g_2^{-1/2} \left(\frac{\texttt{MTOL}^2}{3\,\#\mathcal{T}_h |\widehat{\Delta}_K|} \right)^{1/3} \Big(\prod_{i=1}^{3} g_i \Big)^{1/18},$$
$$\lambda_{3,K} = g_1^{-1/2} \left(\frac{\texttt{MTOL}^2}{3\,\#\mathcal{T}_h |\widehat{\Delta}_K|} \right)^{1/3} \Big(\prod_{i=1}^{3} g_i \Big)^{1/18}.$$

The optimal piecewise constant metric $\mathcal{M}_{\mathcal{T}_h}$ is thus obtained simply by collecting the optimal values $\{\mathbf{r}_{i,K}\}_{i=1}^{3}$ and $\{\lambda_{i,K}\}_{i=1}^{3}$, for each $K \in \mathcal{T}_h$. The optimal metric is finally provided to a metric-based mesh generator to build the adapted mesh. For this task, we employ `mmg3d`, a standalone application suited for grid adaptation [27]. The output file containing the adapted mesh is then read by `FreeFem++`, the environment used to code the whole procedure itemized in Algorithm 3 [51, 52].

Algorithm 3 SIMPATY: SIMP with AdaptiviTY

Input : `CTOL, MTOL, kmax`, $\rho_{\min}$, $\mathcal{T}_h^0$

1: Set: $\rho_h^0 = 1$, $\mathtt{k} = 0$, errM = 1+`CTOL`
2: **while** errM > `CTOL` & $\mathtt{k} <$ `kmax` **do**
3: $\quad \rho_h^{\mathtt{k}+1} =$ `optimize`$(\rho_h^{\mathtt{k}}$, `Mit, TOPT,` $\nabla_\rho \mathcal{G}$, ...);
4: $\quad \mathcal{T}_h^{\mathtt{k}+1} =$ `adapt`$(\mathcal{T}_h^{\mathtt{k}}$, $\rho_h^{\mathtt{k}+1}$, `MTOL`);
5: $\quad$ errM $= |\#\mathcal{T}_h^{\mathtt{k}+1} - \#\mathcal{T}_h^{\mathtt{k}}|/\#\mathcal{T}_h^{\mathtt{k}}$;
6: $\quad \mathtt{k} = \mathtt{k} + 1$;

The main difference with respect to Algorithm 2 is in line 4, where mesh adaptation is carried out, with a prescribed tolerance, `MTOL`, on the accuracy. For the stopping criterion, at line 5, we check the stagnation of the adapted meshes through the relative variation of the cardinality of the mesh elements to within `CTOL`.

2.3.2 Numerical assessment for TO

The same test cases analyzed in Section 2.2.3 are now tackled by TO.

We remark that `Mit` is usually updated (namely, we decrease `Mit` as `k` increases) within the external loop of Algorithm 3. This choice should allow the optimizer to get very close to the optimal solution on the initial mesh, whereas a less strict check is expected to suffice in the next iterations. Indeed, it is not reasonable to compute an accurate density function on a rough intermediate mesh which is not necessarily the final optimal one.

In order to reduce the computational burden required by TO, we simulate only a quarter of the geometry under investigation, by exploiting the symmetry planes. Precisely, we impose $\mathbf{u} \cdot \mathbf{n} = 0$ on the surfaces where symmetry occurs, and $\mathbf{u} \cdot \mathbf{t} = 0$, with $\mathbf{t}$ the unit tangent vector, on the surfaces where

antisymmetry occurs [45]. In Figure 2.7, the portions of the domain actually employed in the simulations are shown. Once convergence is reached, the complete structures are obtained using reflection tools, avalaible in post processing softwares used for visualization purposes (e.g., Paraview [11]).

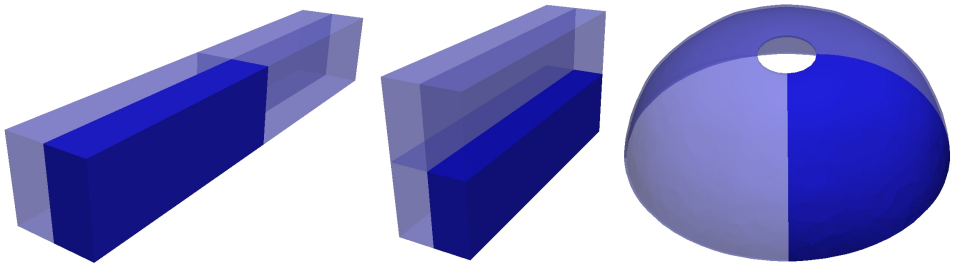

Figure 2.7: Portion of the domains actually simulated by SIMPATY algorithm.

The input parameters for SIMPATY algorithm are gathered in Table 2.5. We do not set any value for `TOPT` since we rely only on `Mit` as a stopping criterion for `optimize`.

Test case	`CTOL`	`MTOL`	`kmax`	$\rho_{\min}$
Bridge	1e-2	0.35	10	0.001
Cantilever beam	5e-3	0.09	10	0.001
Dome	5e-3	1.10	7	0.001

Table 2.5: Input data to SIMPATY algorithm.

The bridge test case

The topology optimization of the bridge is carried out with SIMPATY by setting a volume fraction $\alpha = 0.4$, `Mit` $= 100$ for the first iteration, 50 for the second, and 25 for the subsequent ones, and selecting an initial mesh of 52556 elements.

The resulting function ρ in Figure 2.8, left is characterized by a sharp alternation of void and full material and by very thin layers. The corresponding structure (Figure 2.8, center), obtained by a truncation procedure which keeps only the elements of the mesh where $\rho|_K \geq 0.5$, exhibits very

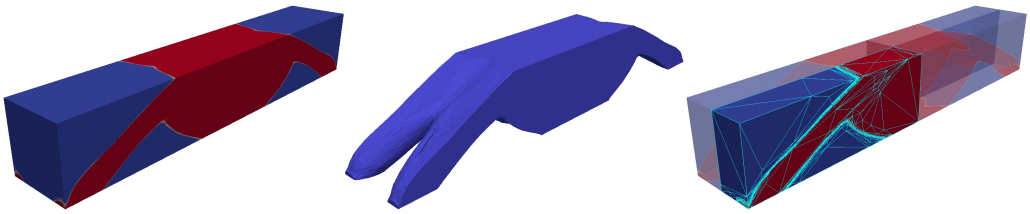

Figure 2.8: The bridge test case (TO): density field (left), final structure (center), and a quarter of the domain with both density and adapted mesh (right) as delivered by SIMPATY.

smooth boundaries and it is almost ready for the printing process. Figure 2.8, right, shows the domain actually employed in the simulations, with the final adapted mesh superposed to the density. In particular, the adapted mesh sharply detects the void/material interface with very stretched tetrahedra. This is more evident in Figure 2.9, which focuses on the external faces from three different view angles. The elements are highly stretched along the boundaries of the structure and they massively concentrate in these portions of the domain. Instead, where the design variable is smooth, the mesh is coarse, reducing the computational burden of the simulation.

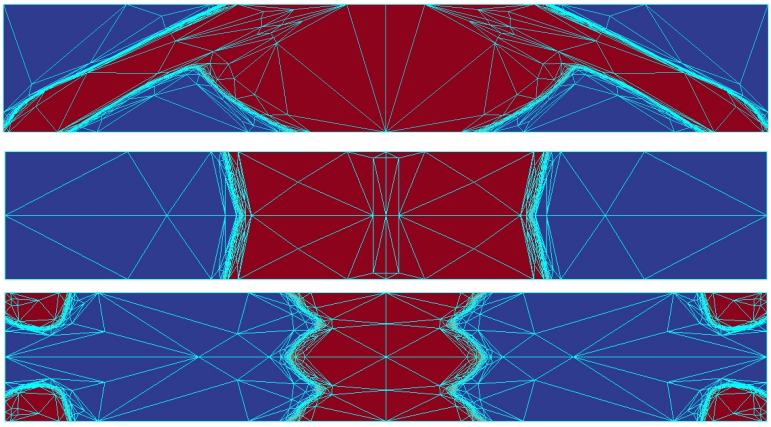

Figure 2.9: The bridge test case (TO): frontal (top), top (center), and bottom (bottom) views of the density superposed to the adapted mesh.

The resulting structure, seen from different angles, is shown in Figure 2.10.

We can appreciate the smoothness of the boundary surfaces, which is made possible by the optimal shape, size and orientation of the mesh elements. In particular, from the bottom view, some complex features of the structure are evident, as further highligthed in the slice-plot shown in Figure 2.11.

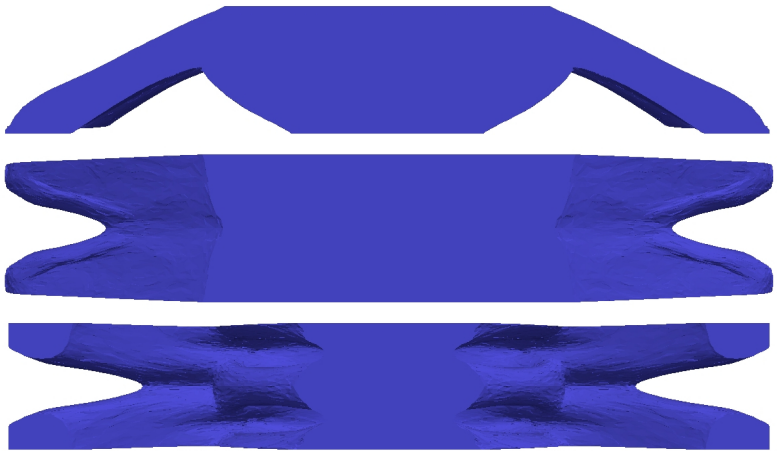

Figure 2.10: The bridge test case (TO): frontal (top), top (center), and bottom (bottom) views of the structure returned by SIMPATY.

In Table 2.6, some quantitative results are provided. As expected, the mass reduction is responsible for a slight increase of the compliance.

$\mathcal{G}$ before TO	0.0933	[J]
$\mathcal{G}$ after TO	0.1009	[J]
$\Delta_{\%}\mathcal{G}$	+8.15%	[-]
$\#\mathcal{T}_h$	95482	[-]

Table 2.6: The bridge test case (TO): compliance before and after TO, percentage variation of the compliance, cardinality of the final adapted mesh.

The cantilever test case

Results for the topology optimized cantilever beam are shown in Figure 2.12. We pick $\alpha = 0.5$, `Mit` $= 75$ for the first iteration, 50 for the following ones, and $\mathcal{T}_h^0$ a uniform mesh consisting of 35280 tetrahedra.

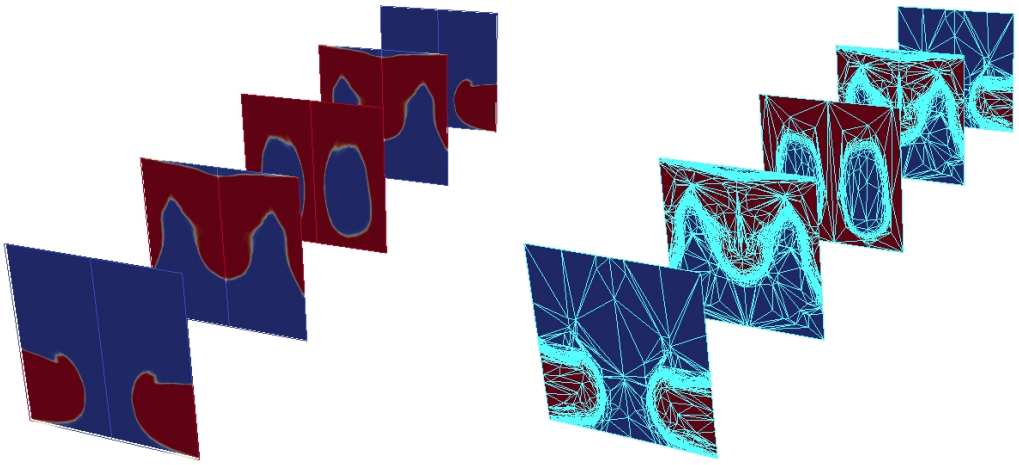

Figure 2.11: The bridge test case (TO): slices of the density (left) and of the adapted mesh (right).

The final structure is very smooth (see Figures 2.12-2.14). Despite the apparent massive external shell, an internal cavity is generated by SIMPATY to lighten the optimized structure as it is also evident from the slice plot in Figure 2.15. The anisotropic features of the adapted mesh are able to sharply capture the interface between material and void, considerably coarsening the mesh in the areas inside and outside the structure.

Concerning the quantitative data in Table 2.7, we have that the reduction of half the mass of the cantilever leads to a considerable increment of the compliance, which almost triplicates with respect to the initial value. Despite the contained number of tetrahedra, the final structure generated by SIMPATY is almost ready to print with a reasonable mechanical response.

$\mathcal{G}$ before TO	0.0309	[J]
$\mathcal{G}$ after TO	0.0867	[J]
$\Delta_{\%}\mathcal{G}$	180%	[-]
$\#\mathcal{T}_h$	96038	[-]

Table 2.7: The cantilever test case (TO): compliance before and after TO, percentage variation of the compliance, cardinality of the final adapted mesh.

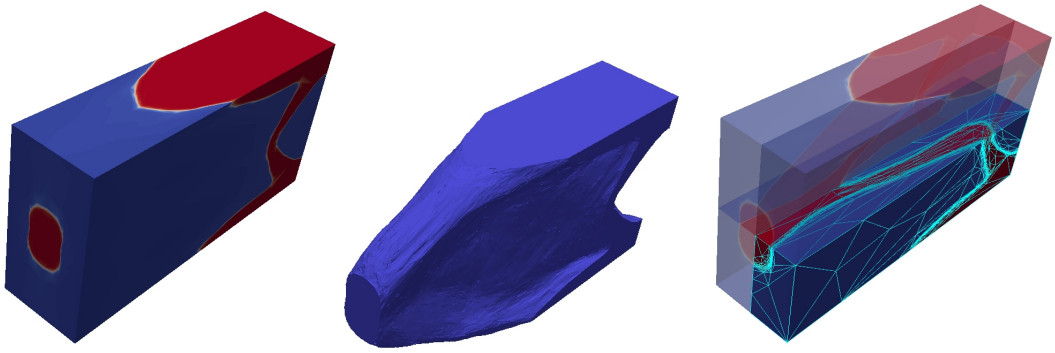

Figure 2.12: The cantilever test case (TO): density field (left), final structure (center), and a quarter of the domain with both density and adapted mesh (right) as delivered by SIMPATY.

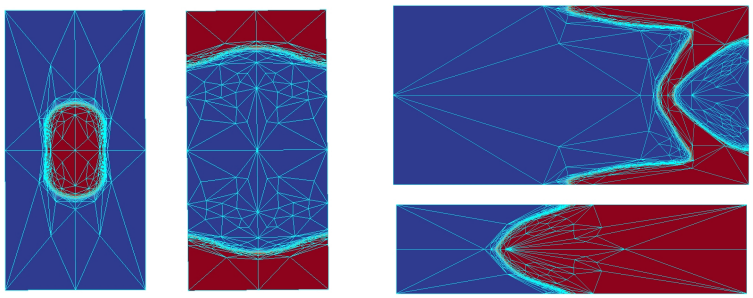

Figure 2.13: The cantilever test case (TO): frontal (top), rear (center), lateral (right-top), and top (right-bottom) views of the density superposed to the adapted mesh.

The dome test case

For the dome test case, we set $\alpha = 0.2$, `Mit` $= 120$ for the first iteration, 60 for the second, and 20 for the subsequent ones, and we employ an initial grid of 20857 elements.

The final layout for the optimized dome is shown in Figure 2.16, where the smooth final density, left is shown along with a close-up of the quarter of domain actually employed, right. In addition, three views of the obtained structure are provided in Figure 2.17. SIMPATY algorithm turns out to be

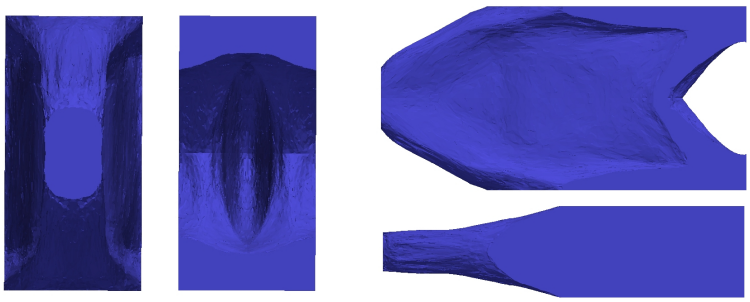

Figure 2.14: The cantilever test case (TO): frontal (left), rear (center), lateral (right-top), and top (right-bottom) views of the structure returned by SIMPATY.

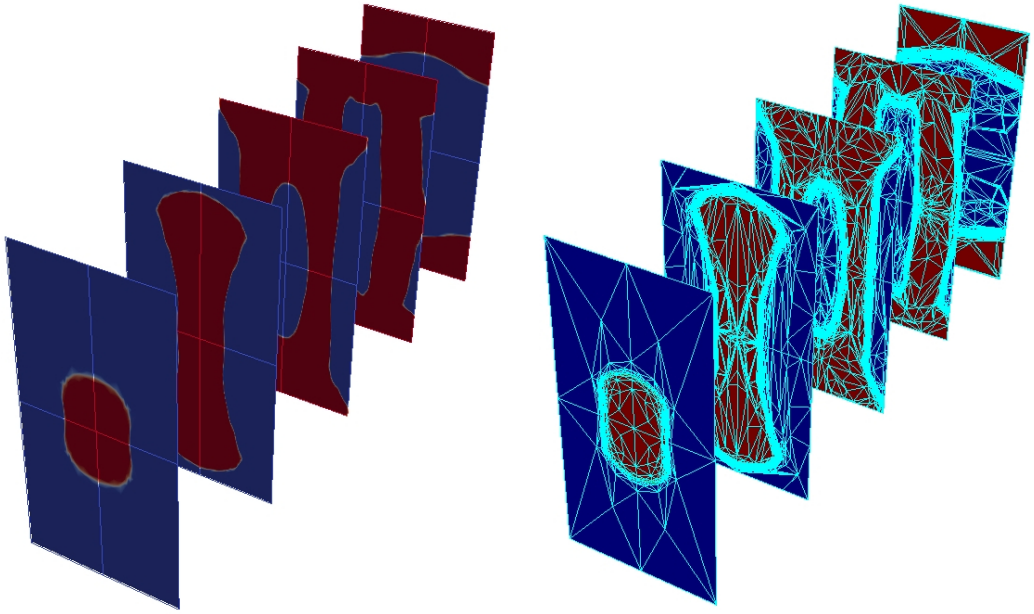

Figure 2.15: The cantilever test case (TO): slices of the density (left) and of the adapted mesh (right).

effective also in the case of a thin shell domain. In some way, the obtained layout can be identified with a macro-grid, in the spirit of a Michell structure [53]. Finally, Figure 2.18 shows how the anisotropic mesh closely follows

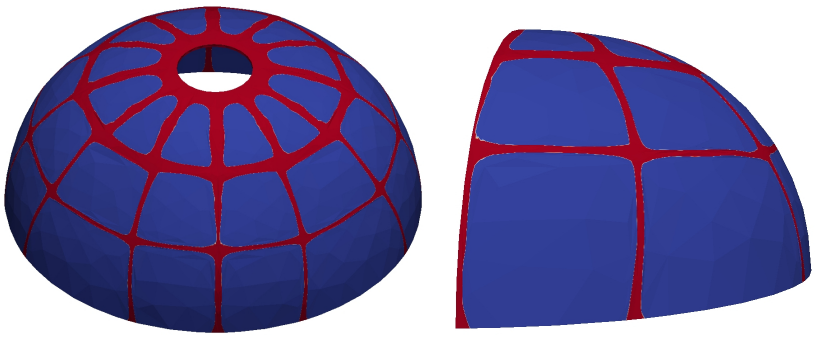

Figure 2.16: The dome test case (TO): density (left), and a quarter of the domain close-up (right) as delivered by SIMPATY.

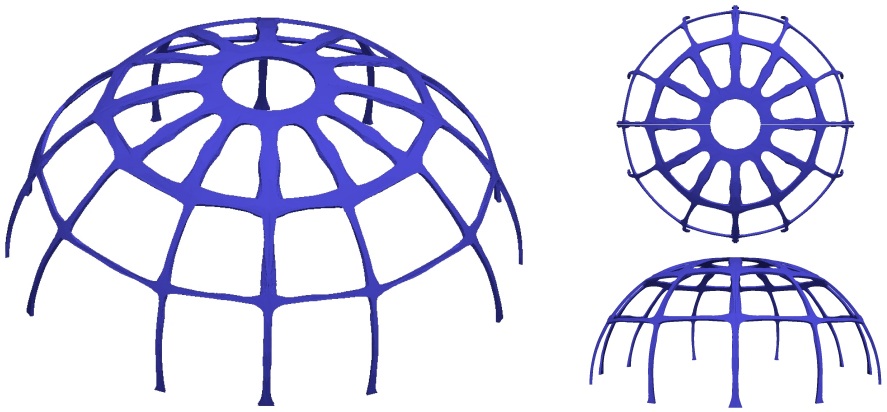

Figure 2.17: The dome test case (TO): frontal (left), top (right-top), and lateral (right-bottom) views of the structure returned by SIMPATY.

the distribution of the material despite the very thready components of the optimized dome.

The values collected in Table 2.8 show that a considerable reduction of the mass of the final configuration leads to a slight increase in the compliance. The number of elements in the final configuration is rather high likely due to the curvature of the geometry. The software `mmg3d` includes options to control the geometric features of the domain, so that the mesh can follow the original curvature of the surface to within a threshold.

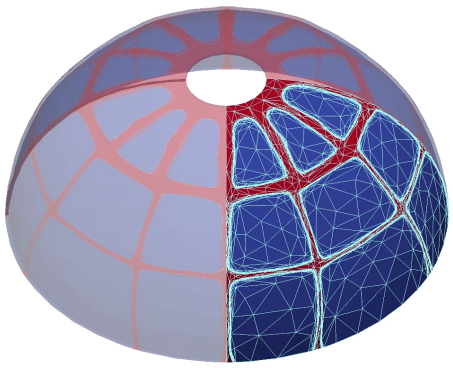

Figure 2.18: The dome test case (TO): adapted mesh superposed to the density for a quarter of the domain.

$\mathcal{G}$ before TO	7.1654	[J]
$\mathcal{G}$ after TO	7.7265	[J]
$\Delta_{\%}\mathcal{G}$	+7.83%	[-]
$\#\mathcal{T}_h$	118435	[-]

Table 2.8: The dome test case (TO): compliance before and after TO, percentage variation of the compliance, cardinality of the final adapted mesh.

A comparison with another approach in the literature.

We compare the performance of SIMPATY algorithm with the anisotropic mesh adaptation proposed in [45]. The main difference in the two algorithms lies in the driving force for the adaptation procedure, namely an actual error estimator in SIMPATY versus a heuristic indicator based on the filtered Hessian of the density and of a filtered sensitivity. In contrast, we essentially do not apply any filtering.

In particular, we consider the same configuration as in Figure 9 of [45]. The structure provided by SIMPATY (see Figure 2.19) is topologically comparable with the one in [45].

From a quantitative viewpoint, the outcome from SIMPATY provides a slightly better performing structure, characterized by a compliance equal to 1.2996 versus a compliance of 1.5529 in [45]. Moreover, SIMPATY converges in 9 iterations after 0.76 [h][1], providing a final mesh with 4205 nodes to be

[1]The computations have been run on a GenuineIntel Pentium(R) Dual-Core CPU

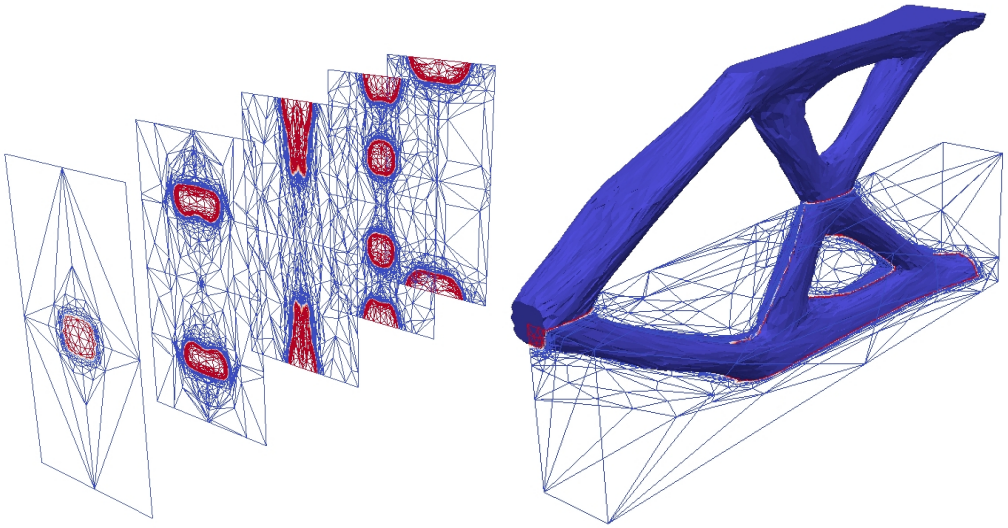

Figure 2.19: Comparison with [45]: slice plot for the density and the adapted mesh (top); whole optimized structure and adapted mesh on the simulated quarter of domain (bottom).

compared with 3.3 [h] and 3121 vertices in [45].

2.4 The coupling of shape and topology optimization

So far, shape and topology optimization have been applied separately. The goal now is to combine them in order to improve the overall performance of the optimization (see, e.g., [28, 41, 44, 57, 71]).

On the one hand, TO delivers light structures with a mass reduction with respect to the initial configuration but with a higher compliance. On the other hand, SO ensures a reduction of the compliance keeping the volume fixed. Hence, the idea here is to sequentially couple the two techniques to take advantage of the benefits of both of them.

In principle, there are at least three possibile combinations of topology and shape optimization: SO first and TO after (STO), TO first and SO after

E6300 2.80 GHz 4GB RAM desktop computer.

(TSO), and SO and TO iteratively intertwined. We pursue the first approach, namely, we first move *out of the box* the boundary of the design domain by means of SO. Then, the resulting structure is topologically optimized by means of the SIMPATY algorithm. The choice for STO instead of TSO is justified by the observation that the shape optimization of an already topologically optimized structure emphasizes the thinning of the thready components, even leading to invalid mesh elements, and, in general, to non-manufacturable layouts. These drawbacks may be amplified by a more tight alternation between SO and TO, while are generally mitigated by a STO approach.

The STO procedure is listed in Algorithm 4.

Algorithm 4 Shape and Topology Optimization (STO)

Input : `CTOL, MTOL, ktmax, ksmax`, Δ_{BEST}, $\mathcal{T}_h^0$, V_0, $\rho_{\min}$

Set: $\mathtt{ks} = 0$, $\mathtt{k}_{BEST} = 0$, $\mathcal{T}_{BEST} = \mathcal{T}_h^0$, $\mathcal{G}_{BEST} = \mathcal{G}(\Omega^0)$;
while $\mathtt{ks} - \mathtt{k}_{BEST} < \Delta_{BEST}$ & $\mathtt{ks} < \mathtt{ksmax}$ **do**
    Solve (2.6);
    Solve (2.7);
    Compute $\phi^{\mathtt{k}}$, $\ell^{\mathtt{k}}$;
    $\mathcal{T}_h^{\mathtt{ks}+1} = \mathtt{movemesh}(\mathcal{T}_h^{\mathtt{ks}}, \mathbf{d}_h^{\mathtt{ks}}, \ell^{\mathtt{ks}})$;
    while $\mathcal{T}_h^{\mathtt{ks}+1}$ has degenerate elements **do**
        Reduce $\ell^{\mathtt{ks}}$;
        $\mathcal{T}_h^{\mathtt{ks}+1} = \mathtt{movemesh}(\mathcal{T}_h^{\mathtt{ks}}, \mathbf{d}_h^{\mathtt{ks}}, \ell^{\mathtt{ks}})$;
    $\mathcal{T}_h^{\mathtt{ks}+1} = \mathtt{regularize}\ (\mathcal{T}_h^{\mathtt{ks}+1})$;
    Compute $\mathcal{G}(\Omega)$;
    if $\mathcal{G}(\Omega) < \mathcal{G}_{BEST}$ **then**
        $\mathcal{G}_{BEST} = \mathcal{G}(\Omega)$;
        $\mathtt{k}_{BEST} = \mathtt{ks} + 1$;
        $\mathcal{T}_{BEST} = \mathcal{T}_h^{\mathtt{ks}+1}$;
    $\mathtt{ks} = \mathtt{ks} + 1$;
Set: $\rho_h^0 = 1$, $\mathtt{kt} = 0$, errM $= 1 +$ `CTOL`, $\mathcal{T}_h^0 = \mathcal{T}_h^{\mathtt{ks}}$
while errM $>$ `CTOL` & $\mathtt{kt} < \mathtt{ktmax}$ **do**
    $\rho_h^{\mathtt{kt}+1} = \mathtt{optimize}\ (\rho_h^{\mathtt{kt}}, \mathtt{Mit}, \mathtt{TOPT}, \nabla_\rho \mathcal{G}, ...)$;
    $\mathcal{T}_h^{\mathtt{kt}+1} = \mathtt{adapt}(\mathcal{T}_h^{\mathtt{kt}}\ , \rho_h^{\mathtt{kt}+1}, \mathtt{MTOL})$;
    errM $= |\#\mathcal{T}_h^{\mathtt{kt}+1} - \#\mathcal{T}_h^{\mathtt{kt}}|/\#\mathcal{T}_h^{\mathtt{kt}}$;
    $\mathtt{kt} = \mathtt{kt} + 1$;

2.4.1 Numerical assessment for STO

We re-run the test cases analyzed for SO and TO. The parameters for SO are the same as those in Section 2.2.3. Instead, the values for TO are listed in Table 2.9, the volume fraction α being the same as in Section 2.3.2.

Test case	`CTOL`	`MTOL`	`ktmax`	$\rho_{\min}$
Bridge	5e-3	0.01	15	0.001
Cantilever	1e-3	0.075	10	0.001
Dome	5e-3	1.00	11	0.001

Table 2.9: Input data to SIMPATY algorithm for STO.

The bridge test case

The STO bridge is shown in Figures 2.20-2.23. It is evident the combined effect of SO with TO. In particular, we recognize as external shape the one delivered by the single SO (compare with Figure 2.2), whereas the two spans of the bridge are yielded by TO similarly to what obtained in Figure 2.8, center. Notice that the final structure is sufficiently symmetric, even though no symmetry condition is enforced in the algorithm. This can be ascribed to the sufficiently fine isotropic grid used as initial mesh $\mathcal{T}_h^0$, consisting of 10477 tetrahedra, so that the results are not biased by a poor discretization.

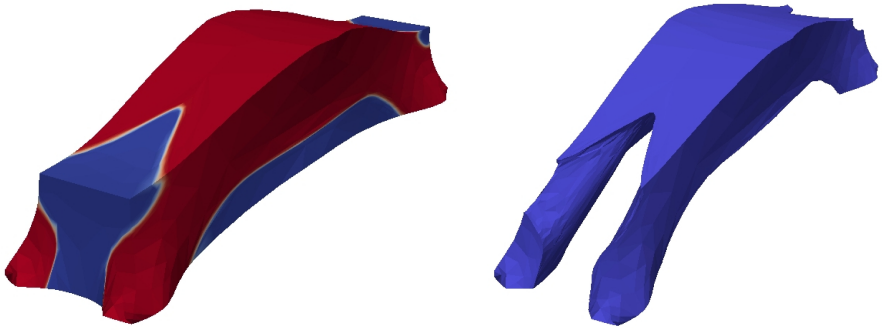

Figure 2.20: The bridge test case (STO): density field (left) and final structure (right).

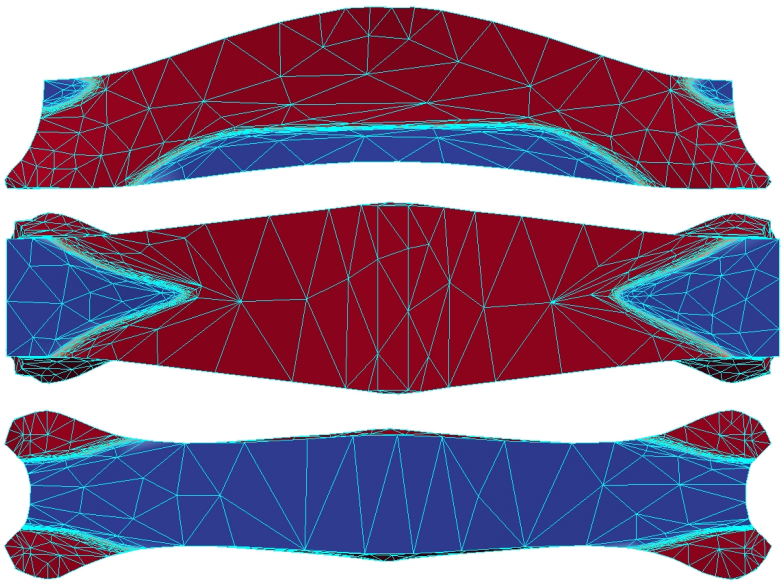

Figure 2.21: The bridge test case (STO): frontal (top), top (center), and bottom (bottom) views of the density superposed to the adapted mesh.

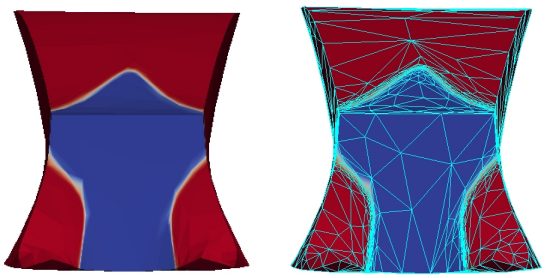

Figure 2.22: The bridge test case (STO): lateral view of the density (left) and of the density superposed to the adapted mesh (right).

Finally, Table 2.10 highlights the reduction of the objective function with respect to the non-optimized case. The benefits due to SO in terms of structure stiffness are not thoroughly compromised by the TO step. Additionally, the number of elements in the final mesh is considerably low for a full 3D simulation.

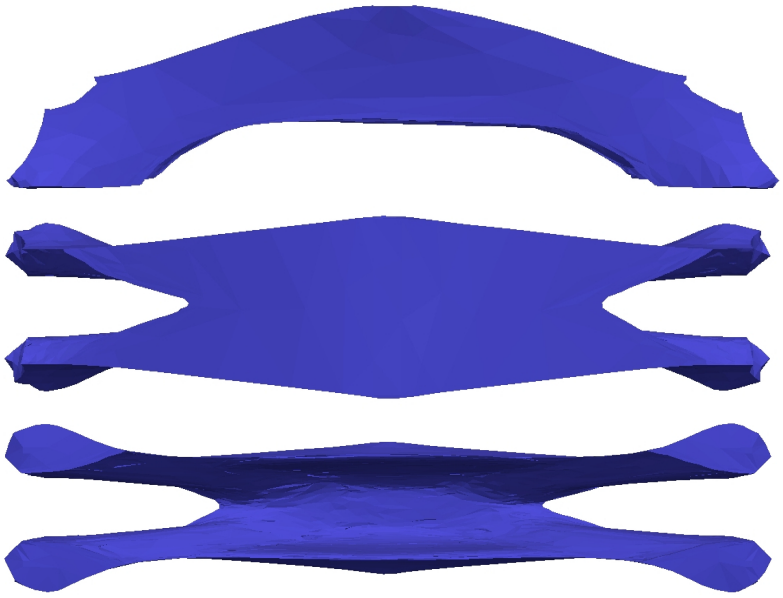

Figure 2.23: The bridge test case (STO): frontal (top), top (center), and bottom (bottom) views of the final structure.

$\mathcal{G}$ before STO	0.0933	[J]
$\mathcal{G}$ after STO	0.0820	[J]
$\Delta_{\%}\mathcal{G}$	-12.12%	[-]
$\#\mathcal{T}_h$	40301	[-]

Table 2.10: The bridge test case (STO): compliance before and after STO, percentage variation of the compliance, cardinality of the final adapted mesh.

The cantilever test case

The cantilever beam yielded by Algorithm 4 starting from an initial mesh comprising 120355 elements, is displayed in Figures 2.24-2.26. The external shape is essentially the same as in Figure 2.4, while the inner topology has considerably changed with respect to that provided by the sole SIMPATY algorithm. Indeed, we recognize the presence of an additional cavity in the frontal part of the cantilever, as clearly highlighted by comparing Figure 2.14 with Figure 2.26. This redistribution of the material makes the structure stiffer in the STO case with respect to the TO case, as confirmed by the

values in Tables 2.7 and 2.11. A slight lack of symmetry can be observed in the final configuration.

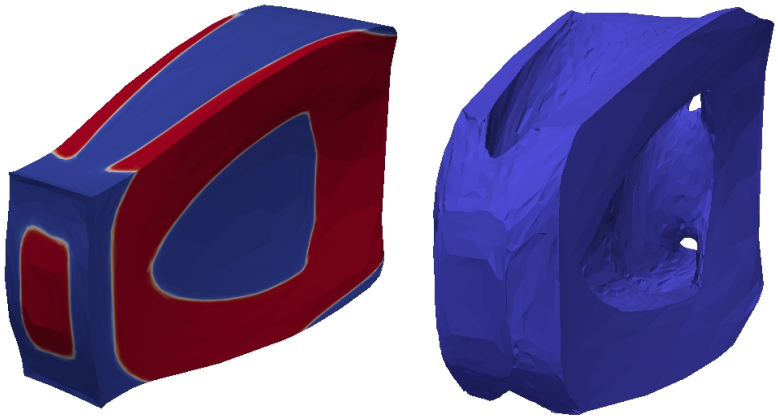

Figure 2.24: The cantilever test case (STO): density field (left) and final structure (right).

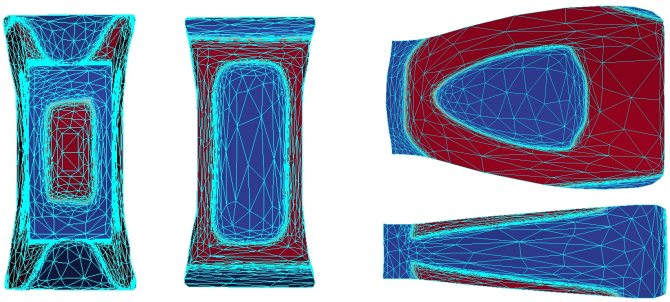

Figure 2.25: The cantilever test case (STO): frontal (left), rear (middle), lateral (right-top), and top (right-bottom) views of the density superposed to the adapted mesh.

The dome test case

The structure obtained for the dome geometry initially tiled by 92964 elements, is completely different from a straightforward merging of the effects

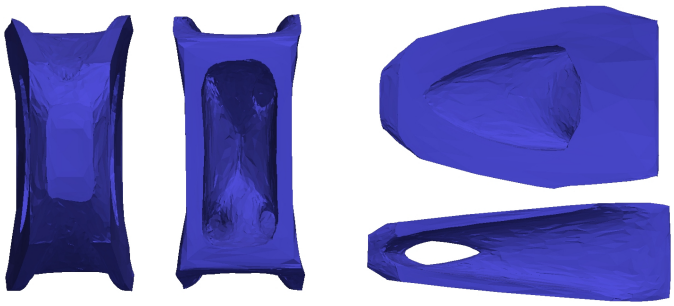

Figure 2.26: The cantilever test case (STO): frontal (left), rear (middle), lateral (right-top), and top (right-bottom) views of the final structure.

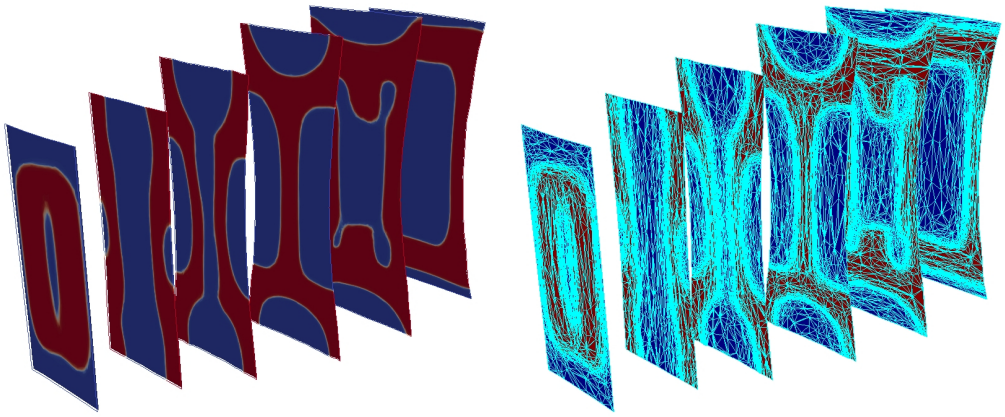

Figure 2.27: The cantilever test case (STO): slices of the density (left) and of the adapted mesh (right).

$\mathcal{G}$ before STO	0.0309	[J]
$\mathcal{G}$ after STO	0.0162	[J]
$\Delta_{\%}\mathcal{G}$	-47.4%	[-]
$\#\mathcal{T}_h$	127513	[-]

Table 2.11: The cantilever test case (STO): compliance before and after STO, percentage variation of the compliance, cardinality of the final adapted mesh.

of SO and TO. A two-story layout for STO replaces the three-story configuration in Figure 2.17. Additionally, we loose the radial symmetry of the TO

case.

Finally, the values in Table 2.12 confirm the trend of the other test cases, with a net decrease of the compliance despite the drastic reduction of the total mass by 80%.

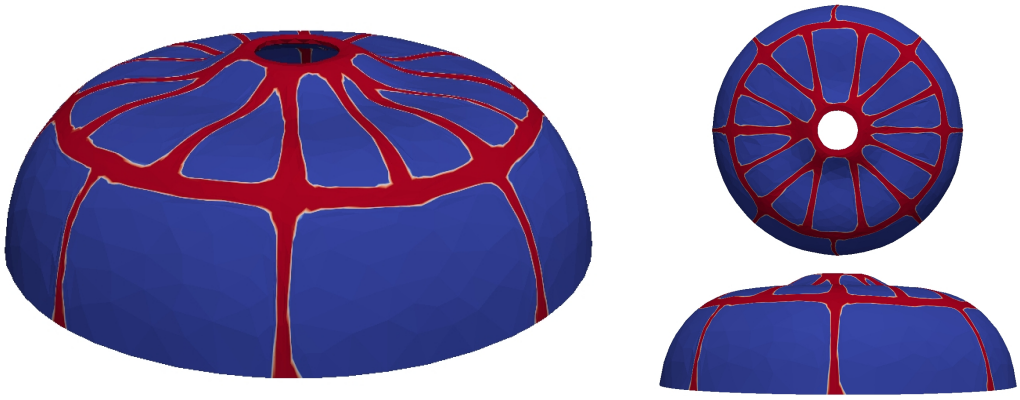

Figure 2.28: The dome test case (STO): frontal (left), top (right-top), and lateral (right-bottom) views of the final density field.

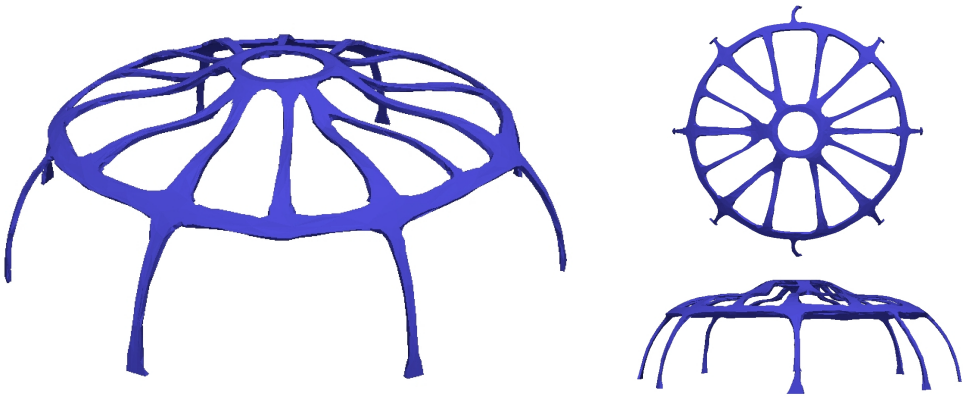

Figure 2.29: The dome test case (STO): frontal (left), top (right-top), and lateral (right-bottom) views of the final structure.

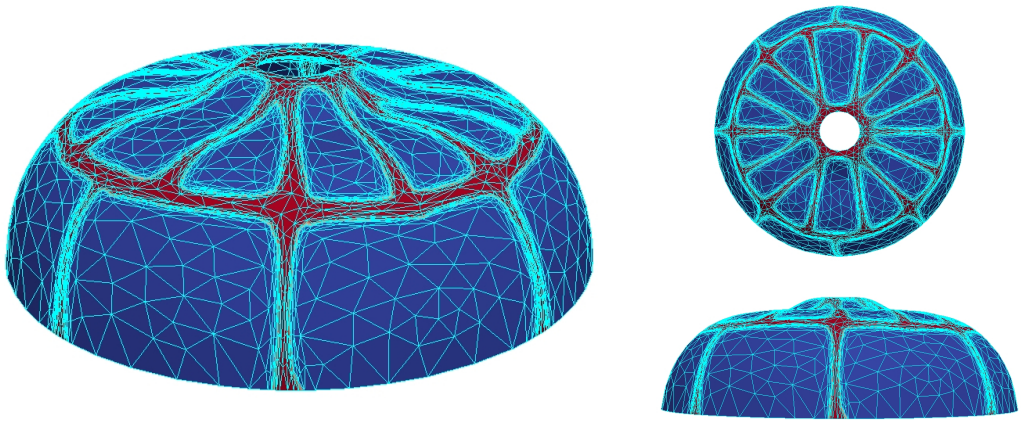

Figure 2.30: The dome test case (STO): frontal (left), top (right-top), and lateral (right-bottom) views of adapted mesh superposed to the density.

$\mathcal{G}$ before STO	7.1654	[J]
$\mathcal{G}$ after STO	6.9127	[J]
$\Delta_{\%}\mathcal{G}$	-3.52%	[-]
$\#\mathcal{T}_h$	37143	[-]

Table 2.12: The dome test case (STO): compliance before and after STO, percentage variation of the compliance, cardinality of the final adapted mesh.

2.5 Conclusions and future developments

We proposed a new technique for structure design, combining shape optimization (SO) with topology optimization (TO) in order to minimize the compliance of the final layout. A sequential coupling of these two procedures is here enriched by the added value of anisotropic mesh adaptation. The merging between SO and TO allows us to take advantage of the benefits of each single technique. In particular, shape optimization moves the optimized structure out of the initial design domain with a reduction in terms of compliance. Successively, topology optimization is applied to reduce the total mass in the final structure with an increment of the compliance. The main advantage of the sequential coupling is that the increase of the compliance due to the TO step in the STO procedure is not sufficient to compromise the compliance reduction provided by the SO phase, thus ensuring a final benefit

in terms of mechanical performance (see Table 2.13).

The introduction of an anisotropic mesh adaptation procedure has proven to be a key feature. In particular, it allows us to obtain very smooth structures, essentially ready to print, thus avoiding any post-processing.

Test case	Initial $\mathcal{G}$	$\mathcal{G}$ after SO	$\Delta_{\%}\mathcal{G}$	$\mathcal{G}$ after TO	$\Delta_{\%}\mathcal{G}$	$\mathcal{G}$ after STO	$\Delta_{\%}\mathcal{G}$
Bridge	0.0933 [J]	0.0796 [J]	-14.68%	0.1009 [J]	+8.15%	0.0820 [J]	-12.12%
Cantilever	0.0309 [J]	0.0104 [J]	-66.34%	0.0867 [J]	+180%	0.0162 [J]	-47.4%
Dome	7.1654 [J]	3.2433 [J]	-54.74%	7.7265 [J]	+7.83%	6.9127 [J]	-3.52%

Table 2.13: Compliance before and after SO, TO and STO and corresponding percentage variation of the compliance for the three test cases.

Possible future developments of this research include the validation of the STO algorithm on more realistic configurations and the generalization of the procedure to a multi-objective context.

Acknowledgments

The authors acknowledge Tommaso Ferri who carried out the first numerical assessments in [34] under the supervision of the last two authors. Furthermore, we acknowledge the research project GNCS-INdAM 2018 “Tecniche di Riduzione di Modello per le Applicazioni Mediche”, which partially supported this research.

Bibliography

[1] M. Ainsworth and J. T. Oden. *A Posteriori Error Estimation in Finite Element Analysis*. John Wiley & Sons, New York, 2000.

[2] G. Allaire, C. Dapogny, and P. Frey. "Shape optimization with a level set based mesh evolution method". In: *Comput. Methods Appl. Mech. Engrg.* 282 (2014), pp. 22–53.

[3] G. Allaire and G. A. Francfort. "A numerical algorithm for topology and shape optimization". In: *Topology design of structures (Sesimbra, 1992)*. Vol. 227. NATO Adv. Sci. Inst. Ser. E Appl. Sci. Kluwer Acad. Publ., Dordrecht, 1993, pp. 239–248.

[4] G. Allaire, F. Jouve, and A. Toader. "Structural optimization using sensitivity analysis and level set-method". In: *J. Comput. Phys.* 194 (2004), pp. 363–393.

[5] G. Allaire and R. V. Kohn. "Optimal design for minimum weight and compliance in plane stress using extremal microstructures". In: *European J. Mech. A Solids* 12.6 (1993), pp. 839–878.

[6] G. Allaire and O. Pantz. "Structural optimization with FreeFem++". In: *Struct. Multidiscip. Optim.* 32.3 (2006), pp. 173–181.

[7] G. Allaire. *Shape Optimization by the Homogenization Method*. Vol. 146. Applied Mathematical Sciences. Springer-Verlag, New York, 2002.

[8] G. Allaire et al. "Structural optimization using topological and shape sensitivity via a level set method". In: *Control Cybernet.* 34.1 (2005), pp. 59–80.

[9] L. Ambrosio and G. Buttazzo. "An optimal design problem with perimeter penalization". In: *Calc. Var. Partial Differential Equations* 1.1 (1993), pp. 55–69.

[10] S. Amstutz. "Connections between topological sensitivity analysis and material interpolation schemes in topology optimization". In: *Struct. Multidiscip. Optim.* 43.6 (2011), pp. 755–765.

[11] U. Ayachit. *The ParaView Guide: A Parallel Visualization Application*. USA: Kitware, Inc., 2015.

[12] W. Bangerth and R. Rannacher. *Adaptive Finite Element Methods for Differential Equations*. Lectures in Mathematics ETH Zürich. Birkhäuser Verlag, Basel, 2003.

[13] N. V. Banichuk. *Introduction to Optimization of Structures*. Springer-Verlag, New York, 1990.

[14] M. P. Bendsøe. "Optimal shape design as a material distribution problem". In: *Struct. Optimization* 1.4 (1989), pp. 193–202.

[15] M. P. Bendsøe. *Optimization of Structural Topology, Shape, and Material*. Springer-Verlag, Berlin, 1995, pp. xii+271.

[16] M. P. Bendsøe and N. Kikuchi. "Generating optimal topologies in structural design using a homogenization method". In: *Comput. Methods Appl. Mech. Engrg.* 71.2 (1988), pp. 197–224.

[17] M. P. Bendsøe and O. Sigmund. "Material interpolation schemes in topology optimization". In: *Arch. Appl. Mech.* 69.9 (1999), pp. 635–654.

[18] M. P. Bendsøe and O. Sigmund. *Topology Optimization: Theory, Methods and Applications*. Springer-Verlag, Berlin Heidelberg, 2003.

[19] B. Bourdin and A. Chambolle. "Design-dependent loads in topology optimization". In: *ESAIM Control. Optim. Calc. Var.* 9 (2003), pp. 19–48.

[20] M. Bruggi and M. Verani. "A fully adaptive topology optimization algorithm with goal-oriented error control". In: *Comput. Struct.* 89 (2011), pp. 1481–1493.

[21] M. Burger and S. J. Osher. "A survey on level set methods for inverse problems and optimal design". In: *European J. Appl. Math.* 16.2 (2005), pp. 263–301.

[22] S. Cai and W. Zhang. "Stress constrained topology optimization with free-form design domains". In: *Comput. Methods Appl. Mech. Engrg.* 289 (2015), pp. 267–290.

[23] V. J. Challis and J. K. Guest. "Level set topology optimization of fluids in Stokes flow". In: *Int. J. Numer. Meth. Engng* 79.10 (2009), pp. 1284–1308.

[24] E. K. Chong and S. H. Zak. *An Introduction to Optimization*. Vol. 76. John Wiley & Sons, 2013.

[25] P. W. Christensen and A. Klarbring. *An Introduction to Structural Optimization*. Vol. 153. Solid Mechanics and its Applications. Springer, New York, 2009.

[26] P. G. Ciarlet. *The Finite Element Method for Elliptic Problems*. North-Holland Publishing Co., Amsterdam-New York-Oxford, 1978, pp. xix+530.

[27] C. Dapogny, C. Dobrzynski, and P. Frey. "Three-dimensional adaptive domain remeshing, implicit domain meshing, and applications to free and moving boundary problems". In: *J. Comput. Phys.* 262 (2014), pp. 358–378.

[28] C. Dapogny et al. "Geometric constraints for shape and topology optimization in architectural design". In: *Comput. Mech.* 59.6 (2017), pp. 933–965.

[29] L. Dedè, M. J. Borden, and T. J. R. Hughes. "Isogeometric analysis for topology optimization with a phase field model". In: *Arch. Comput. Methods Eng.* 19.3 (2012), pp. 427–465.

[30] L. Dedè, S. Micheletti, and S. Perotto. "Anisotropic error control for environmental applications". In: *Appl. Numer. Math.* 58.9 (2008), pp. 1320–1339.

[31] A. Díaz and O. Sigmund. "Checkerboard patterns in layout optimization". In: *Struct. Multidiscip. Optim.* 19 (1995), pp. 89–92.

[32] A. R. Díaz and M. P. Bendsøe. "Shape optimization of structures for multiple loading conditions using a homogenization method". In: *Struct. Optim.* 4.1 (1992), pp. 17–22.

[33] P. E. Farrell, S. Micheletti, and S. Perotto. "An anisotropic Zienkiewicz-Zhu-type error estimator for 3D applications". In: *Int. J. Numer. Meth. Engng* 85.6 (2011), pp. 671–692.

[34] T. Ferri. "Topology and Shape Optimization for Structural Design". MA thesis. Politecnico di Milano, 2017.

[35] L. Formaggia, S. Micheletti, and S. Perotto. "Anisotropic mesh adaption with application to CFD problems". In: *Proceedings of WCCM V, Fifth World Congress on Computational Mechanics*. Ed. by H. Mang, F. Rammerstorfer, and J. Eberhardsteiner. 2002, pp. 1481–1493.

[36] H. Garcke et al. "Numerical approximation of phase field based shape and topology optimization for fluids". In: *SIAM J. Sci. Comput.* 37.4 (2015), A1846–A1871.

[37] P.-L. George and H. Borouchaki. *Delaunay Triangulation and Meshing. Application to Finite Elements*. Editions Hermès, Paris, 1998.

[38] M. Giacomini, O. Pantz, and K. Trabelsi. "Volumetric expressions of the shape gradient of the compliance in structural shape optimization". arXiv:1701.05762. 2017.

[39] A. A. Gomes and A. Suleman. "Application of spectral level set methodology in topology optimization". In: *Struct. Multidiscip. Optim.* 31.6 (2006), pp. 430–443.

[40] P. L. Gould. *Introduction to Linear Elasticity*. Springer–Verlag, New York, 1994.

[41] F. de Gournay, G. Allaire, and F. Jouve. "Shape and topology optimization of the robust compliance via the level set method". In: *ESAIM Control Optim. Calc. Var.* 14.1 (2008), pp. 43–70.

[42] H. Harbrecht. "Analytical and numerical methods in shape optimization". In: *Math. Methods Appl. Sci.* 31.18 (2008), pp. 2095–2114.

[43] F. Hecht. "New development in FreeFem++". In: *J. Numer. Math.* 20.3-4 (2012), pp. 251–265.

[44] N. Jenkins and K. Maute. "An immersed boundary approach for shape and topology optimization of stationary fluid-structure interaction problems". In: *Struct. Multidiscip. Optim.* 54.5 (2016), pp. 1191–1208.

[45] K. E. Jensen. "Anisotropic mesh adaptation and topology optimization in three dimensions". In: *J. Mech. Design* 138.6 (2016), pp. 061401–1–061401–8.

[46] U. Kirsch. *Optimum Structural Design: Concepts, Methods, and Applications*. McGraw-Hill, 1991.

[47] B. S. Lazarov and O. Sigmund. "Filters in topology optimization based on Helmholtz-type differential equations". In: *Int. J. Numer. Meth. Engng* 86.6 (2011), pp. 765–781.

[48] Z. D. Ma, N. Kikuchi, and I. Higiwara. "Structural topology and shape optimization for a frequency response problem". In: *Comput. Mech.* 13.3 (1993), pp. 157–174.

[49] S. Micheletti and S. Perotto. "Anisotropic adaptation via a Zienkiewicz-Zhu error estimator for 2D elliptic problems". In: *Numerical Mathematics and Advanced Applications*. Ed. by G. Kreiss et al. Springer-Verlag Berlin Heidelberg. 2010, pp. 645–653.

[50] S. Micheletti, S. Perotto, and P. E. Farrell. "A recovery-based error estimator for anisotropic mesh adaptation in CFD". In: *Bol. Soc. Esp. Mat. Apl. SeMA* 50 (2010), pp. 115–137.

[51] S. Micheletti, S. Perotto, and L. Soli. *Ottimizzazione topologica adattativa per la fabbricazione stratificata additiva*. Italian patent application No. 102016000118131, filed on November 22, 2016 (extended as *Adaptive topology optimization for additive layer manufacturing*, International patent application PCT No. PCT/IB2017/057323). 2017.

[52] S. Micheletti, S. Perotto, and L. Soli. "Topology optimization driven by anisotropic mesh adaptation: towards free-form design". Submitted.

[53] A. Michell. "The limits of economy of material in frame-structures". In: *Philosophy Magazine* 8 (1904), pp. 589–597.

[54] D. J. Munk, G. A. Vio, and G. P. Steven. "Topology and shape optimization methods using evolutionary algorithms: a review". In: *Struct. Multidiscip. Optim.* 52.3 (2015), pp. 613–631.

[55] J. Nocedal and S. J. Wright. *Numerical Optimization*. Springer Series in Operations Research. Springer-Verlag, New York, 1999.

[56] A. Paganini, F. Wechsung, and P. E. Farrell. "Higher-order moving mesh methods for PDE-constrained shape optimization". In: *SIAM J. Sci. Comput.* 40.4 (2018), A2356–A2382.

[57] O. Pantz and K. Trabelsi. "Simultaneous shape, topology, and homogenized properties optimization". In: *Struct. Multidiscip. Optim.* 34.4 (2007), pp. 361–365.

[58] O. Pironneau. *Optimal Shape Design for Elliptic Systems*. Springer Series in Computational Physics. Springer-Verlag, New York, 1984, pp. xii+168.

[59] G. I. N. Rozvany. "A critical review of established methods of structural topology optimization". In: *Struct. Multidiscip. Optim.* 37 (2009), pp. 217–237.

[60] O. Sigmund and J. Petersson. "Numerical instabilities in topology optimization: a survey on procedures dealing with checkerboards, mesh-dependencies and local minima". In: *Struct. Optim.* 16.1 (1998), pp. 68–75.

[61] O. Sigmund. "On the usefulness of non-gradient approaches in topology optimization". In: *Struct. Multidiscip. Optim.* 43.5 (2011), pp. 589–596.

[62] O. Sigmund and K. Maute. "Topology optimization approaches, A comparative review". In: *Struct. Multidiscip. Optim.* 48.6 (2013), pp. 1031–1055.

[63] J. Sokolowski and J.-P. Zolésio. "Introduction to shape optimization". In: *Introduction to Shape Optimization: Shape Sensitivity Analysis*. Berlin, Heidelberg: Springer Berlin Heidelberg, 1992, pp. 5–12.

[64] K. Svanberg. "The method of moving asymptotes-a new method for structural optimization". In: *Int. J. Numer. Meth. Engng* 24.2 (1987), pp. 359–373.

[65] S. I. Valdez et al. "Topology optimization benchmarks in 2D: results for minimum compliance and minimum volume in planar stress problems". In: *Arch. Comput. Methods Eng.* 24.4 (2017), pp. 803–839.

[66] R. Verfürth. *A Review of A Posteriori Error Estimation and Adaptive Mesh-Refinement Techniques*. Wiley & Teubner, 1996.

[67] C. H. Villanueva and K. Maute. "CutFEM topology optimization of 3D laminar incompressible flow problems". In: *Comput. Methods Appl. Mech. Engrg.* 320 (2017), pp. 444–473.

[68] A. Wächter. "An Interior Point Algorithm for Large-Scale Nonlinear Optimization with Applications in Process Engineering". PhD thesis. Carnegie Mellon University, 2002.

[69] A. Wächter and L. T. Biegler. "On the implementation of an interior-point filter line-search algorithm for large-scale nonlinear programming". In: *Math. Program.* 106.1, Ser. A (2006), pp. 25–57.

[70] M. Y Wang, X. Wang, and D. Guo. "A level set method for structural topology optimization". In: *Comput. Methods Appl. Mech. Engrg.* 192.1-2 (2003), pp. 227–246.

[71] Y. Wang and Z. Kang. "A level set method for shape and topology optimization of coated structures". In: *Comput. Methods Appl. Mech. Engrg.* 329 (2018), pp. 553–574.

[72] C. Woodward. "Methods for computer-aided design of free-form objects". In: *Acta Polytech. Scand. Math. Comput. Sci. Ser.* 56 (1990), p. 60.

[73] J. Wu, A. Clausen, and O. Sigmund. "Minimum compliance topology optimization of shell-infill composites for additive manufacturing". In: *Comput. Methods Appl. Mech. Engrg.* 326 (2017), pp. 358–375.

[74] O. C. Zienkiewicz and J. Z. Zhu. "A simple error estimator and adaptive procedure for practical engineering analysis". In: *Int. J. Numer. Meth. Engng* 24 (1987), pp. 337–357.

[75] O. C. Zienkiewicz and J. Z. Zhu. "The superconvergent patch recovery and a posteriori error estimates. I: The recovery technique". In: *Int. J. Numer. Meth. Engng* 33 (1992), pp. 1331–1364.

[76] O. C. Zienkiewicz and J. Z. Zhu. "The superconvergent patch recovery and a posteriori error estimates. II: Error estimates and adaptivity". In: *Int. J. Numer. Meth. Engng* 33 (1992), pp. 1365–1382.

[77] J.-P. Zolésio. "Introduction to shape optimization problems and free boundary problems". In: *Shape Optimization and Free Boundaries (Montreal, PQ, 1990)*. Vol. 380. NATO Adv. Sci. Inst. Ser. C Math. Phys. Sci. Kluwer Acad. Publ., Dordrecht, 1992, pp. 397–457.

3

Density-based inverse homogenization with anisotropically adapted elements

N. Ferro, S. Micheletti, S. Perotto

To appear in Special Issue of the Springer Series "Lecture Notes in Computational Science and Engineering (LNCSE)", Proceedings of the 19th International Conference on Finite Elements in Flow Problems (FEF2017)

3.1 Introduction

The design of performant and light structures has been gaining popularity for the last years thanks to the rise and development of Additive Manufacturing (AM) techniques. Differently from subtractive methods, AM enjoys great versatility in the achievable shapes and presents very few limitations.

In this framework, topology optimization (TO) has proved to be the reference mathematical method suitable for designing innovative and performant structures of engineering interest. Essentially, it consists in the allocation

of material in the so-called design domain, ensuring the optimization of a given functional and, at the same time, the satisfaction of design requirements. The final result of TO is an optimized structure, where areas of full material and void alternate so that the new topology guarantees the desired production specifications.

With a particular focus on the linear elastic problem, it is observed that the stiffness of an optimal designed structure, subject to given loads and constraints, is increased by inserting small substructures [2]. Consequently, different authors have investigated the possibility of employing topology optimization at a microscale as well, aiming at yielding optimized microstructures (metamaterials) [24, 26]. The ultimate goal is to combine the microscopic optimized structures with a standard TO performed at the macroscale. This link is made possible by employing homogenization techniques, which are widely used to incorporate the information provided by the microscale into macroscale models [1, 3, 19].

In this work, we enrich such an approach by resorting to a numerical discretization of the linear elastic problem based on a standard finite element solver combined with a mesh adaptation procedure. In particular, in Section 3.2, we briefly present a density-based approach for a generic topology optimization problem. In Section 3.3, the homogenization procedure is presented. We distinguish between a direct and an inverse method, consisting in prescribing the desired macroscopic effective values in order to retrieve the optimal microstructure. Section 3.4 is devoted to the numerical approximation and to the anisotropic setting used for the finite element discretization. In particular, we examine the mathematical tool employed to anisotropically adapt a two-dimensional mesh to the problem at hand, coupling such a procedure with the inverse homogenization technique. In Section 3.5, some numerical results are provided in order to assess the proposed algorithm, and finally some conclusions are drawn in Section 3.6.

3.2 A density-based method for topology optimization

We consider the SIMP formulation for topology optimization to address the structural optimization problem [2]. In this context, the optimal layout of a material is determined in terms of an auxiliary scalar field, say ρ, defined over

the domain Ω. In particular, ρ is a relative density belonging to $L^\infty(\Omega, [0,1])$, determining presence of full material ($\rho = 1$) or void ($\rho = 0$). The optimization problem is set once the objective function $\mathcal{C}$ and the design requirements are defined, while a balance equation $\mathcal{S}$ constrains the optimization. Then, in order to account for changes in the topology, the state equation $\mathcal{S}$ is properly modified to include the density variable in the formulation. The final optimization problem thus reads

$$\min_{\rho \in L^\infty(\Omega)} \mathcal{C}(\rho) \ : \begin{cases} \text{State equation } \mathcal{S}(\rho) \text{ is satisfied} \\ \text{Boundary conditions} \\ \int_\Omega \rho \, d\Omega \ \leq \alpha |\Omega| \\ \rho_{\min} \leq \rho \leq 1, \end{cases} \tag{3.1}$$

where α is the maximum volume fraction we wish to ensure in the final configuration, and $\rho_{\min}$ is a lower bound for the density, to avoid the possible ill-posedness of $\mathcal{S}$.

In particular, $\mathcal{S}$ is chosen according to the physical phenomenon under investigation, i.e., to the application at hand. For instance, for the optimization of elastic structures, the state equation can be represented by the linear elastic equation, whereas, when considering the optimization of the energy dissipation of a steady flow, one can identify $\mathcal{S}$ with the Stokes equations. In the specific case of the present work, we deal with the optimization of the design of elastic microstructures. A homogenized version of the elastic equations will represent the reference state equation as detailed in the following section. Concerning the inclusion of the density variable in the state equation, a suitable power law of ρ is usually employed to weigh the main physical constants in $\mathcal{S}$, such as the standard Lamé constants, λ and μ, for the elastic problem or the inverse permeability of the fluid for the Stokes equations.

3.3 The homogenization procedure

The homogenization method is an asymptotic technique whose goal is to assign macroscopic effective properties to microscopic entities, which are arranged periodically. This approach plays a crucial role in multiscale simulations since it allows one to deal with the macroscale only, the effects of the microscale being inherited through homogenization. The technique has been

widely investigated both theoretically [3, 19] and numerically [1], and it is a well-established practice.

In this section, we analyze also the converse technique, known as inverse homogenization [13, 18, 21, 22]. This can be formulated as a control problem or, specifically, as a topology optimization problem. The aim is to find the optimal arrangement of material at the microscale so that desired effective properties are guaranteed at the macroscale. Notice that the flow of information is opposite with respect to the classical homogenization. The macroscale is fixed or prescribed, whereas the microscale is modified to match the desired requirements.

3.3.1 The direct method

Direct homogenization has been employed in different fields of application to modify the macroscale model according to the microscale layout [6, 11, 19]. This technique relies on the periodic arrangement of a microstructure which constitutes the base cell, Y. Such elementary entity represents the domain of interest and it is analyzed in order to retrieve its effect on the macroscale.

Let us consider the linear elasticity equation [10]

$$-\nabla \cdot \sigma(\mathbf{u}) = \mathbf{f} \quad \text{in } \Omega, \tag{3.2}$$

where $\Omega \subset \mathbb{R}^2$ is the domain under investigation at the macroscale, $\mathbf{f}$ is the volumetric forcing term, $\mathbf{u} = [u_1, u_2]^T$ is the displacement field, and σ is the stress tensor. For the sake of generality, we stick to the convention of denoting by E_{ijkl} the fourth-order stiffness tensor, so that the stress tensor has components

$$\sigma_{ij} = E_{ijkl}\varepsilon_{kl} \text{ with } \varepsilon_{kl} = \frac{1}{2}\left(\frac{\partial u_k}{\partial x_l} + \frac{\partial u_l}{\partial x_k}\right),$$

where x_l, with $l = 1, 2$, are the spatial coordinates, ε_{kl} are the components of the strain tensor ε, and we have adopted the Einstein notation to manage index summation.

The homogenization technique relies on the repetition of the base cell Y. In order to preserve this physical feature, we impose periodic boundary conditions. In this way, we enforce that the displacement field $\mathbf{u}$ is equal in correspondence with opposite boundaries [5].

Then, the actual objective becomes to compute the homogenized (or effective) stiffness tensor, E^H, representing a macroscopic mean value of the

tensor E, after neglecting the microscale fluctuations E^*. To this end, we resort to an asymptotic expansion of the displacement field $\mathbf{u}$ with respect to the base cell size, considering only the first two terms. Then, following [3, 21], it can be shown that the homogenized tensor E^H is given by

$$E^H_{ijkl} = \frac{1}{|Y|}\int_Y E_{ijpq}(\varepsilon^{0,kl}_{pq} - \varepsilon^{*,kl}_{pq})\,dY, \tag{3.3}$$

where $|Y|$ is the measure of the cell Y, $\varepsilon^{0,kl}$ identifies a fixed strain field, chosen among the four linearly independent possible fields (k, l being equal to $1, 2$), while $\varepsilon^{*,kl}$ is the Y-periodic fluctuation strain, i.e., the weak solution to the equation

$$\int_Y E_{ijpq}\varepsilon^{*,kl}_{pq}\varepsilon_{ij}(v)\,dY = \int_Y E_{ijpq}\varepsilon^{0,kl}_{pq}\varepsilon_{ij}(v)\,dY, \quad \forall v \in V, \tag{3.4}$$

$V \subset [H^1(Y)]^4$ being a periodic Sobolev function space. Thus, by combining (3.3) and (3.4), we obtain the final form of the effective stiffness tensor [1, 21]

$$E^H_{ijkl} = \frac{1}{|Y|}\int_Y E_{pqrs}(\varepsilon^{0,kl}_{pq} - \varepsilon^{*,kl}_{pq})(\varepsilon^{0,ij}_{rs} - \varepsilon^{*,ij}_{rs})\,dY. \tag{3.5}$$

Equations (3.4) and (3.5) constitute the state equations to be employed in the inverse homogenization technique, as detailed in the following section.

3.3.2 The inverse method

We refer to inverse homogenization as the procedure concerning the design of a base cell, Y, whose contribution to the macroscale, according to the direct homogenization process in the previous section, is prescribed [18, 22]. In order to modify the formulation of the direct method, we have to account for variations in the initial distribution of material in the base cell. This goal can be pursued via topology optimization, yielding optimized structures according to specific, user-defined, constraints and objectives.

The same paradigm as in Section 3.2 is now exploited to incorporate the cell design in the homogenization problem. Let us fix the objective function, $\mathcal{J}$, as a control over the quadratic deviation between the computed value of the homogenized stiffness tensor, E^H, and the requested one, E^W, i.e.,

$$\mathcal{J} = \sum_{ijkl}(E^H_{ijkl}(\rho) - E^W_{ijkl})^2.$$

Hence, the minimization of $\mathcal{J}$ should lead to a micro-design, whose macro-features are the ones desired by the user [22]. Thus, the final system for the micro-optimization is obtained by solving the following problem

$$\min_{\rho \in L^\infty(Y)} \mathcal{J}(\rho) \ : \begin{cases} (3.4)_\rho - (3.5)_\rho \text{ are satisfied} \\ + \text{ Periodicity conditions} \\ \int_Y \rho \, dY \ \leq \alpha |Y| \\ \rho_{\min} \leq \rho \leq 1, \end{cases} \tag{3.6}$$

where $(3.4)_\rho - (3.5)_\rho$ represent equations (3.4) and (3.5) after replacing E_{ijkl} with $\rho^p E_{ijkl}$, in order to include the design variable ρ in the formulation, p being a penalization exponent.

3.4 The numerical discretization

Problem (3.6) can be numerically solved via a finite element discretization [7]. After introducing a conforming tessellation $\mathcal{T}_h = \{K\}$ of Y, with K the generic triangle, we denote by V_h^r the associated finite element spaces of piecewise polynomials of degree $r > 0$, with h the maximum diameter of the mesh elements.

The topology optimization problem discretized via a finite element scheme is known to suffer from several numerical issues [14, 20]. Some of these can be tackled with a suitable choice of the spaces employed to discretize displacement and density or via filtering techniques. Here, we propose to contain any post-processing phase by exploiting the intrinsic smoothness of the optimized density field yielded using ad-hoc meshes. In particular, we choose to discretize problem (3.6) on a sequence of anisotropically adapted grids and, consequently, we modify the optimization algorithm to deliver smooth and, essentially, directly manufacturable structures.

3.4.1 The anisotropic setting

We resort to an anisotropic adaptive procedure driven by the density field ρ, which is expected to sharply change from 0 to 1 in correspondence with the boundaries of the structure. The expected strong gradients across the material-void interface justify the employment of anisotropic meshes as an ideal tool to sharply describe the directional features of the density field.

We follow a metric-based procedure in order to generate the optimal mesh to discretize the problem [9]. Essentially, the adaptation procedure relies on an a posteriori error estimator, merging the error information with the geometric properties of the grid. In particular, we employ an anisotropic variant of the Zienkiewicz-Zhu estimator [25], to evaluate the H^1-seminorm of the discretization error, which is expected to be the most effective measure for detecting the material-void interface. Following [15], the elementwise contribution to the anisotropic error estimator is

$$\eta_K^2 = \frac{1}{\lambda_{1,K}\lambda_{2,K}} \sum_{i=1}^{2} \lambda_{i,K}^2 \left(\mathbf{r}_{i,K}^T \, G_{\Delta_K}\big(E_\nabla\big) \mathbf{r}_{i,K} \right), \tag{3.7}$$

where $\lambda_{1,K}$ and $\lambda_{2,K}$ are the lengths of the semi-axes of the ellipse circumscribed to element K, while $\mathbf{r}_{1,K}$ and $\mathbf{r}_{2,K}$ represent the directions of such axes. The quantity $E_\nabla = \big[P(\nabla\rho_h) - \nabla\rho_h\big]_{\Delta_K}$ is the recovered error associated with the density ρ, where $P(\nabla\rho_h)|_{\Delta_K} = |\Delta_K|^{-1} \sum_{T\in\Delta_K} |T| \nabla\rho_h|_T$ denotes the recovered gradient computed on the patch Δ_K of the elements sharing at least a vertex with K, $|\cdot|$ being the measure operator, and $\nabla\rho_h$ is the gradient of the discrete density [8, 16]. Finally, $G_{\Delta_K}(\cdot) \in \mathbb{R}^{2\times 2}$ is the symmetric positive semidefinite matrix with entries

$$[G_{\Delta_K}(\mathbf{w})]_{i,j} = \sum_{T\in\Delta_K} \int_T w_i \, w_j \, dT \quad \text{with } i,j = 1,2, \tag{3.8}$$

for any vector-valued function $\mathbf{w} = (w_1, w_2)^T \in [L^2(\Omega)]^2$. Then, the global error estimator is given by $\eta^2 = \sum_{K\in\mathcal{T}_h} \eta_K^2$.

The mesh adaptation is carried out by minimizing the number of elements of the adapted mesh, while requiring an upper bound `TOLAD` to the global error estimator η together with an error equidistribution criterion. This gives rise to an elementwise constrained optimization problem which admits a unique analytic solution. Specifically, by introducing the aspect ratio $s_K = \lambda_{1,K}/\lambda_{2,K} \geq 1$ measuring the deformation of element K, the adapted grid is characterized by the following quantities

$$s_K^{adapt} = \sqrt{g_1/g_2}, \quad \mathbf{r}_{1,K}^{adapt} = \mathbf{g}_2, \quad \mathbf{r}_{2,K}^{adapt} = \mathbf{g}_1,$$

where $\{g_i, \mathbf{g}_i\}_{i=1,2}$ are the eigen-pairs associated with the scaled matrix $\widehat{G}_{\Delta_K}(E_\nabla) = G_{\Delta_K}(E_\nabla)/|\Delta_K|$, with $g_1 \geq g_2 > 0$, $\{\mathbf{g}_i\}_{i=1,2}$ orthonormal vectors.

Finally, imposing the equidistribution, i.e., $\eta_K^2 = \texttt{TOLAD}^2/\#\mathcal{T}_h$, with $\#\mathcal{T}_h$ the mesh cardinality, we obtain the geometric information identifying the new adapted mesh, i.e.,

$$\lambda_{1,K}^{adapt} = g_2^{-1/2}\left(\frac{\texttt{TOLAD}^2}{2\#\mathcal{T}_h\,|\widehat{\Delta}_K|}\right)^{1/2}, \quad \lambda_{2,K}^{adapt} = g_1^{-1/2}\left(\frac{\texttt{TOLAD}^2}{2\#\mathcal{T}_h\,|\widehat{\Delta}_K|}\right)^{1/2},$$
$$\mathbf{r}_{1,K}^{adapt} = \mathbf{g}_2, \quad \mathbf{r}_{2,K}^{adapt} = \mathbf{g}_1, \tag{3.9}$$

with $|\widehat{\Delta}_K| = |\Delta_K|/(\lambda_{1,K}\lambda_{2,K})$.

3.4.2 The adaptive algorithm

The algorithm employed to merge the topology optimization of the base cell Y with the mesh adaptation procedure described above is here presented. We name it microSIMPATY algorithm since it is inspired from the algorithm SIMPATY in [17].

Algorithm 5 : microSIMPATY

Input : $\texttt{CTOL}, \texttt{TOLAD}, \texttt{TOPT}, \texttt{kmax}, \rho_{\min}, \mathcal{T}_h^{(0)}$

1: Set: ρ_h^0, k = 0, errC = 1 + CTOL
2: **while** errC > CTOL & k < kmax **do**
3: $\quad \rho_h^{k+1} = \texttt{optimize}(\rho_h^k, \texttt{Mit}, \texttt{TOPT}, \rho_{\min}, \mathcal{J}(\rho), \nabla_\rho \mathcal{J}(\rho), ...)$;
4: $\quad \mathcal{T}_h^{(k+1)} = \texttt{adapt}(\mathcal{T}_h^{(k)}, \rho_h^{k+1}, \texttt{TOLAD})$;
5: $\quad$ errC $= |\#\mathcal{T}_h^{(k+1)} - \#\mathcal{T}_h^{(k)}|/\#\mathcal{T}_h^{(k)}$;

In Algorithm 5, `optimize` is a numerical routine for the inverse topology optimization, which stops whenever the maximum number of iterations, `Mit`, is exceeded, or the prescribed tolerance, `TOPT`, is satisfied. Beside the objective function $\mathcal{J}(\rho)$, the corresponding derivative with respect to ρ is required by the `optimize` algorithm, as well as other possible constraints to be imposed, with the associated derivatives. Such sensitivities are analytically computed following a Lagrangian approach [4]. Function `adapt` is a routine performing the mesh adaptation starting from the metric derived in (3.9). The algorithm is terminated by two stopping criteria, one based on the number of iterations, the other on the stagnation of the number of elements between two consecutive mesh adaptations to within `CTOL`.

3.5 Numerical results

The following numerical verification has been carried out with `FreeFem++` [12], which provides the users with built-in functions for both optimization [23] and metric-based mesh adaptation. In both the considered test cases, we deal with the design of a 1[m] $\times$1[m] base cell with negative Poisson ratio $\nu = \lambda/[2(\lambda+\mu)]$, corresponding to E_{1122}. We choose $p = 4$ for the penalization exponent in (3.6). The material employed has Young modulus equal to 0.91[Pa] and Poisson ratio $\nu = 0.3$. Finally, ρ_h^0 is set to $|\sin(2\pi x_1)\sin(2\pi x_2)|$.

Case 1. In Figure 3.1, the results for $E^W_{1122} = -1$ are shown. We require a volume fraction $\alpha = 0.3$, we start with an initial structured mesh consisting of 1800 elements, and we pick `TOLAD` $= 10^{-5}$, `CTOL` $= 10^{-4}$, `TOPT` $= 10^{-3}$, $\rho_{\min} = 10^{-4}$, `kmax` $= 20$, while the maximum number of iterations, `Mit`, is set to 35 for the first three iterations and to 10 for the next ones. The algorithm stops after 20 iterations, delivering a structure with $E^H_{1122} = -0.65$. The final

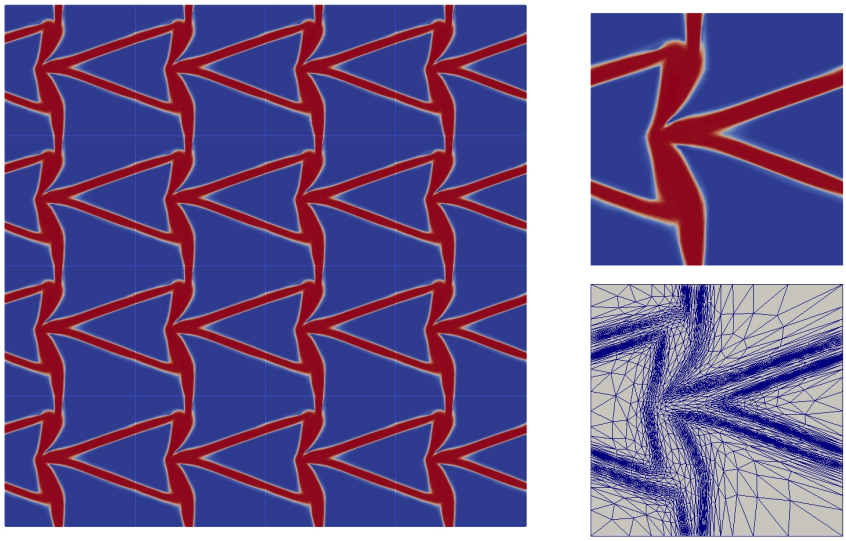

Figure 3.1: Optimized microstructure for $E^W_{1122} = -1$: 4×4 periodic arrangement of the base cell (left), base cell (top-right) and corresponding adapted mesh (bottom-right).

design thus obtained is comparable with the one in [13], Figure 3, while the

quality of the solution is increased when resorting to the microSIMPATY algorithm, no filtering techniques being required. In Figure 3.1, bottom-right, we show the last adapted grid. Notice that the elements are highly stretched and concentrated in correspondence with the void-solid interface. The cardinality of such final mesh is 2620 and its maximum aspect ratio is 97.76.

Case 2. The second case concerns the optimization of a micro-design with $E^W_{1122} = -0.7$ and $\alpha = 0.5$ (see [21], Figure 2.17). As for the previous test, we perform 20 iterations, starting from a structured mesh of 1800 elements and picking the same parameters as in the previous case, except for `Mit`, which is now set to 35 at the first iteration, to 25 until the fifth one, and to 15 for the later iterations. The results in Figure 3.2 show a very smooth solution, where intermediate densities are very limited to a thin boundary layer, whose quality is enhanced by the adapted grid. In the final mesh, the directionalities of the density field are properly detected, making 4266 elements enough for a sharply-defined solution, with a maximum value for the aspect ratio equal to 85.58. The final structure delivers an effective Poisson ratio equal to -0.54.

3.6 Conclusions

In this work, we presented an algorithm to optimize microstructures according to user-defined requirements, based on the inverse homogenization method, properly merged with an anisotropic mesh adaptation procedure.

The structures derived in Section 3.5 are consistent with the ones available in the literature and exhibit a remarkable smoothness along structure boundaries, the thin material/void layers being sharply detected by the adapted mesh. This feature confirms the benefits due to microSIMPATY algorithm.

Nevertheless, the optimization process depends on several parameters to be accurately tuned in order to meet user requirements. For this reason, we plan to perform a more rigorous investigation in such a direction, especially to make the homogenized stiffness tensor closer to the requested one.

Finally, with a view to real applications, we are extending the algorithm to a 3D framework.

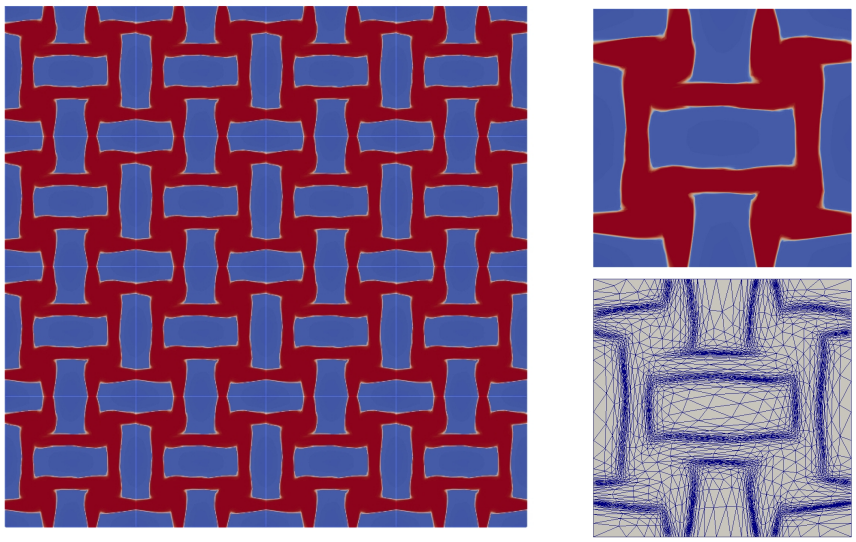

Figure 3.2: Optimized microstructure for $E^W_{1122} = -0.7$: 4×4 periodic arrangement of the base cell (left), base cell (top-right) and corresponding adapted mesh (bottom-right).

Bibliography

[1] E. Andreassen and C. S. Andreasen. "How to determine composite material properties using numerical homogenization". In: *Comp. Mater. Sci.* 83 (2014), pp. 488–495.

[2] M. P. Bendsøe and O. Sigmund. *Topology Optimization: Theory, Methods and Applications*. Springer-Verlag, Berlin Heidelberg, 2003.

[3] A. Bensoussan, J.-L. Lions, and G. Papanicolaou. *Asymptotic Analysis for Periodic Structures*. AMS Chelsea Publishing, Providence, RI, 2011, pp. xii+398.

[4] D. P. Bertsekas. *Constrained optimization and Lagrange multiplier methods*. Computer Science and Applied Mathematics. Academic Press, Inc., New York-London, 1982, pp. xiii+395.

[5] H. Brezis. *Functional Analysis, Sobolev Spaces and Partial Differential Equations*. Universitext. Springer, New York, 2011, pp. xiv+599.

[6] P. W. Chung, K. K. Tamma, and R. R. Namburu. "Homogenization of temperature-dependent thermal conductivity in composite materials". In: *J. Thermophys. Heat Tr.* 15.1 (2001), pp. 10–17.

[7] P. G. Ciarlet. *The Finite Element Method for Elliptic Problems*. North-Holland Publishing Co., Amsterdam-New York-Oxford, 1978, pp. xix+530.

[8] P. E. Farrell, S. Micheletti, and S. Perotto. "An anisotropic Zienkiewicz-Zhu-type error estimator for 3D applications". In: *Int. J. Numer. Meth. Engng* 85.6 (2011), pp. 671–692.

[9] P. J. Frey and P.-L. George. *Mesh generation*. Second. Application to finite elements. ISTE, London; John Wiley & Sons, Inc., Hoboken, NJ, 2008, p. 848.

[10] P. L. Gould. *Introduction to Linear Elasticity*. Springer–Verlag, New York, 1994.

[11] Z. Hashin and S. Shtrikman. "A Variational Approach to the Theory of the Effective Magnetic Permeability of Multiphase Materials". In: *J. Appl. Phys.* 33.10 (1962), pp. 3125–3131.

[12] F. Hecht. "New development in FreeFem++". In: *J. Numer. Math.* 20.3-4 (2012), pp. 251–265.

[13] U. D. Larsen, O. Signund, and S. Bouwsta. "Design and fabrication of compliant micromechanisms and structures with negative Poisson's ratio". In: *J. Microelectromech. S.* 6.2 (1997), pp. 99–106.

[14] B. S. Lazarov and O. Sigmund. "Filters in topology optimization based on Helmholtz-type differential equations". In: *Int. J. Numer. Meth. Engng* 86.6 (2011), pp. 765–781.

[15] S. Micheletti and S. Perotto. "Anisotropic adaptation via a Zienkiewicz-Zhu error estimator for 2D elliptic problems". In: *Numerical Mathematics and Advanced Applications*. Ed. by G. Kreiss et al. Springer-Verlag Berlin Heidelberg. 2010, pp. 645–653.

[16] S. Micheletti, S. Perotto, and P. E. Farrell. "A recovery-based error estimator for anisotropic mesh adaptation in CFD". In: *Bol. Soc. Esp. Mat. Apl. SeMA* 50 (2010), pp. 115–137.

[17] S. Micheletti, S. Perotto, and L. Soli. *Ottimizzazione topologica adattativa per la fabbricazione stratificata additiva*. Italian patent application No. 102016000118131, filed on November 22, 2016 (extended as *Adaptive topology optimization for additive layer manufacturing*, International patent application PCT No. PCT/IB2017/057323). 2017.

[18] M. M. Neves, H. Rodrigues, and J. M. Guedes. "Optimal design of periodic linear elastic microstructures". In: *Comput. Struct.* 76.1-3 (2000), pp. 421–429.

[19] E. Sánchez-Palencia. "Homogenization method for the study of composite media". In: *Asymptotic analysis, II*. Vol. 985. Lecture Notes in Math. Springer, Berlin-New York, 1983, pp. 192–214.

[20] O. Sigmund and J. Petersson. "Numerical instabilities in topology optimization: a survey on procedures dealing with checkerboards, mesh-dependencies and local minima". In: *Struct. Optim.* 16.1 (1998), pp. 68–75.

[21] O. Sigmund. *Design of Material Structures Using Topology Optimization*. Technical University of Denmark, Lyngby, Denmark, Jan. 1994.

[22] O. Sigmund. "Materials with prescribed constitutive parameters: an inverse homogenization problem". In: *Internat. J. Solids Structures* 31.17 (1994), pp. 2313–2329.

[23] A. Wächter. "An Interior Point Algorithm for Large-Scale Nonlinear Optimization with Applications in Process Engineering". PhD thesis. Carnegie Mellon University, 2002.

[24] L. Yin and G. Ananthasuresh. "Topology optimization of compliant mechanisms with multiple materials using a peak function material interpolation scheme". In: *Struct. Multidiscip. O.* 23.1 (2001), pp. 49–62.

[25] O. C. Zienkiewicz and J. Z. Zhu. "A simple error estimator and adaptive procedure for practical engineering analysis". In: *Int. J. Numer. Meth. Engng* 24 (1987), pp. 337–357.

[26] W. Zuo and K. Saitou. "Multi-material topology optimization using ordered SIMP interpolation". In: *Structural and Multidisciplinary Optimization* 55.2 (2017), pp. 477–491.

4

POD-assisted strategies for structural topology optimization

N. Ferro, S. Micheletti, S. Perotto
To appear in Computers & Mathematics with Applications

4.1 Introduction

Topology optimization methods are nowadays popular thanks to recent developments in 3D and rapid prototyping printing techniques [10]. Topology optimization can be demanding in terms of computational resources, especially when complex structures are designed. Due to this issue, several mathematical methods are commonly employed to reduce the complexity of the problem at hand. The purpose of such methods is to find a trade-off between accuracy and efficiency, by devising procedures characterized by a reduced computational burden without waiving the quality of the final manufactured product.

Our interest is in structural optimization among the several fields of application. Different choices are viable to reach the above trade-off. For instance,

in [20, 40] we resort to a customized computational mesh with a contained number of elements, providing smooth and sharp structures almost ready to be printed via additive layer manufacturing. The main idea of this work is to employ a different computational tool to reach the same goal, namely a model reduction procedure based on the Proper Orthogonal Decomposition (POD) [30, 45]. POD is a standard technique to deal with parametric problems, widely employed in engineering applications [28, 32, 34, 43, 49, 54]. POD exploits an offline/online paradigm, when one first samples the parameter space to collect a certain number of high-fidelity scenarios which are successively employed to extract an informative reduced basis for the space of the parametric solutions; then, this basis is used to recover a new scenario with respect to the ones sampled. In general, the dimension of the reduced basis is considerably lower compared with the dimension of the original problem.

As far as we are aware of, few papers address the employment of POD in a structural optimization context. We cite, for instance, [42] where POD is applied to multi-objective shape optimization, [55] combining POD with homogeneization techniques with a view to a multiscale model, and [58] where a frequency response problem is tackled by combining a standard topology optimization method with POD at an algebraic level.

Structural optimization can be pursued by means of different strategies, ranging from size, to shape and topology optimization [8]. In this work, we focus on topology optimization, namely the design tool seeking an optimal material distribution in an initial domain, for assigned loads and boundary conditions, under some constraints (see [6, 8, 15, 44, 48]). Typical optimality criteria are represented by minimum volume, minimum compliance (or maximum stiffness), maximum fundamental frequency in the dynamic case, while constraints can be maximum allowed displacements and stresses, or a given fraction of the initial volume.
Density-based methods are among the widely employed in the engineering community, which offer an alternative to level-set methods [2, 52], topological derivative procedures [50], phase field techniques [9, 16], evolutionary approaches [56], homogenization [1, 6], performance-based optimization [35].

Here we focus on the minimization of the compliance for a fixed volume fraction, by resorting to the density-based SIMP (Solid Isotropic Material with Penalization) method [6, 8, 44]. In practice, it consists of solving a minimization problem for an auxiliary density variable, identifying the material/void distribution, constrained by the linear elasticity equation. In par-

ticular, POD is properly combined with SIMP, by generating a reduced basis for the density only. Extra care will be taken to deal with parameters involving the design constraints. A straightforward combination of POD with SIMP leads to a numerical design process which is efficient but lacks accuracy in some circumstances, in particular when the collected snapshots are excessively either sharp or smooth in correspondence with the material/void boundary. This first merging between POD and SIMP is improved according to a predictor-corrector approach, where the POD prediction is used as an initial guess for the corrector standard SIMP method, further enriched with anisotropic mesh adaptation [39, 40]. We refer to this new method as PC-SIMPOD. It turns out that PC-SIMPOD is robuster than the basic POD approach, providing the desired trade-off between fast simulations and reliable structures, essentially ready-to-print thanks to mesh adaptation.

The paper is organized as follows. In Section 4.2, the basic POD approach for topology optimization is introduced and numerically checked on some benchmark configurations, for different choices of the paramenters. Section 4.3 proposes the PC-SIMPOD method, showing the improvements of this new procedure with respect to the basic POD one. In Section 4.4, PC-SIMPOD is extended to a multi-parameter setting with a view to practical engineering problems. Conclusions are drawn in the last section with perspectives for the future.

4.2 POD for topology optimization

This section focuses on a first attempt to contain the computational cost of SIMP algorithm, by resorting to POD. The assessment in Section 4.2.3 show that we can achieve a considerable gain in terms of computational time even though the predicted layouts are not as performing as expected, in terms of compliance. An additional weak point turns out to be the proper tuning of the procedure used to yield the snapshots for the offline phase.

4.2.1 The topology optimization technique

Structural topology optimization is a mathematical technique whose goal is to provide an optimized structure fulfilling user-defined requirements. In the most general formulation, it consists in redistributing the material inside an initial design domain in order to satisfy mechanical performances combined

with physical constraints. There are several models available in the specialized literature that address the topology optimization problem (see, for instance, [19, 44, 48] for a review on the topic).

Among the several approaches, level set methods and density-based techniques are the most common ones. In both cases, the reference state equation is represented by the linear elasticity problem, suitably incorporating information about the material distribution through an auxiliary function. The level set approach relies on a function χ governed by a time-dependent equation which makes an initial contour propagating towards the optimized final layout [2, 11, 12, 26, 52, 57]. Density-based methods modify the elasticity equation by weighting the Lamé coefficients via a density function, ρ, which identifies the allocation of the material in the structure. In particular, ρ takes values in $[0, 1]$, where $\rho = 0$ means void and $\rho = 1$ material. These methods include phase-field models [9, 16, 23, 53] and the SIMP (Solid Isotropic Material with Penalization) method [3, 4, 5, 7, 8].

In this paper, we focus on the SIMP method. To formalize SIMP method we start from the density-modified elasticity problem

$$\begin{cases} -\nabla \cdot \sigma_\rho(\mathbf{u}) = \mathbf{0} & \text{in } \Omega \\ \mathbf{u} = \mathbf{0} & \text{on } \Gamma_D \\ \sigma_\rho(\mathbf{u})\mathbf{n} = \mathbf{f} & \text{on } \Gamma_N \\ \sigma_\rho(\mathbf{u})\mathbf{n} = \mathbf{0} & \text{on } \Gamma_F, \end{cases} \tag{4.1}$$

where $\Omega \subset \mathbb{R}^2$ defines the design domain with boundary $\partial\Omega$; $\mathbf{u} = [u_1, u_2]^T$ is the displacement field; $\sigma_\rho(\mathbf{u}) = \rho^p \big[2\mu\varepsilon(\mathbf{u}) + \lambda I : \varepsilon(\mathbf{u})\big]$ is the penalized stress tensor, with ρ the density function, p the penalization exponent set to 3 [3, 8], $\varepsilon(\mathbf{u}) = \big(\nabla\mathbf{u} + (\nabla\mathbf{u})^T\big)/2$ the strain tensor,

$$\lambda = \frac{E\nu}{(1+\nu)(1-2\nu)}, \qquad \mu = \frac{E}{2(1+\nu)}$$

the Lamé coefficients, with E the Young modulus, and ν the Poisson ratio, I the identity tensor; $\mathbf{f}$ is a traction applied to a portion Γ_N of $\partial\Omega$; $\Gamma_D \subset \partial\Omega$ and $\Gamma_F = \partial\Omega \backslash (\Gamma_N \cup \Gamma_D)$ denote the portion of the domain where the structure is clamped and stress-free, respectively; $\mathbf{n}$ is the unit outward normal vector to $\partial\Omega$.

With a view to the minimization of the structure compliance, $\mathcal{G}(\mathbf{u}) = \int_{\Gamma_N} \mathbf{f} \cdot \mathbf{u}\, d\gamma$, SIMP formulation becomes

find $\rho \in L^\infty(\Omega)$ such that

$$\min_{\rho \in L^\infty(\Omega)} \mathcal{G}(\mathbf{u}(\rho)) \ : \begin{cases} a_\rho(\mathbf{u}(\rho), \mathbf{v}) = \mathcal{G}(\mathbf{v}) \ \forall \mathbf{v} \in U \\ \mathcal{C}(\rho, \mathbf{u}(\rho)) \leq 0 \end{cases} \tag{4.2}$$

with

$$\mathcal{C}(\rho, \mathbf{u}(\rho)) = \begin{cases} \displaystyle\int_\Omega \rho \, d\Omega - \alpha |\Omega| \\ \rho_{\min} - \rho, \\ \rho - 1, \end{cases}$$

and where $\mathbf{u} \in U = \{\mathbf{v} \in [H^1(\Omega)]^2 \ : \ \mathbf{v} = \mathbf{0} \text{ on } \Gamma_D\}$,

$$a_\rho(\mathbf{u}, \mathbf{v}) = \int_\Omega \sigma_\rho(\mathbf{u}) : \varepsilon(\mathbf{v}) \, d\Omega,$$

is the bilinear form associated with (4.1), $\alpha > 0$ is the maximum volume fraction allowed for the optimized structure, $|\Omega|$ is the measure of the domain, and $\rho_{\min} \in (0, 1)$ is a lower value for the density to ensure the well-posedness of the state equation. Notice that $\rho \mapsto \mathbf{u}(\rho)$ defines the solution operator of the state equation.

The discretization of problem (4.2) is tackled by using standard finite elements [13], yielding

find $\rho_h \in V_h^r$ such that

$$\min_{\rho_h \in V_h^r} \mathcal{G}(\mathbf{u}_h(\rho_h)) \ : \begin{cases} a_\rho(\mathbf{u}_h(\rho_h), \mathbf{v}_h) = \mathcal{G}(\mathbf{v}_h) \ \forall \mathbf{v}_h \in U_h^s \\ \mathcal{C}(\rho_h, \mathbf{u}_h(\rho_h)) \leq 0 \end{cases} \tag{4.3}$$

with

$$\mathcal{C}(\rho_h, \mathbf{u}_h(\rho_h)) = \begin{cases} \displaystyle\int_\Omega \rho_h \, d\Omega - \alpha |\Omega| \\ \rho_{\min} - \rho_h, \\ \rho_h - 1, \end{cases} \tag{4.4}$$

and where $V_h^r \subseteq H^1(\Omega)$ and $U_h^s \subset U$ are the scalar and vector continuous finite element spaces, associated with a triangulation, $\mathcal{T}_h = \{K\}$, of Ω, of degree r and s, respectively and where it is understood that $\mathbf{u}_h(\rho_h) \in U_h^s$.

It is well-known that SIMP suffers from some issues, such as the mesh dependence, the presence of undesired intermediate densities, and checkerboard patterns [8, 18, 47]. In particular, to mitigate the checkerboard effect,

it is advisable choosing $r \leq s$ in (4.3)-(4.4). As an alternative, we follow the approach proposed in [20, 40], by picking $r = s = 1$. For this particular choice, in the sequel we adopt the simplified notation V_h and U_h.

The minimization is performed using a gradient-like method by properly including the constraints [41].

4.2.2 The POD method applied to topology optimization

We now aim at performing a structure optimization driven by SIMP at a contained computational cost. For this purpose, we introduce the parametrized version of (4.3)-(4.4),

find $\rho_h^\mu \in V_h$ such that

$$\min_{\rho_h^\mu \in V_h} \mathcal{G}(\mathbf{u}_h(\rho_h^\mu)) \ : \begin{cases} a_\rho^\mu(\mathbf{u}_h(\rho_h^\mu), \mathbf{v}_h) = \mathcal{G}^\mu(\mathbf{v}_h) \ \forall \mathbf{v}_h \in U_h \\ \mathcal{C}^\mu(\rho_h^\mu, \mathbf{u}_h(\rho_h^\mu)) \leq 0 \end{cases} \tag{4.5}$$

with

$$\mathcal{C}^\mu(\rho_h^\mu, \mathbf{u}_h(\rho_h^\mu)) = \begin{cases} \displaystyle\int_\Omega \rho_h^\mu \, d\Omega - \alpha|\Omega| \\ \rho_{\min} - \rho_h^\mu, \\ \rho_h^\mu - 1, \end{cases} \tag{4.6}$$

with μ a real parameter which may be related to the state equation and/or to the constraint inequality.

Algorithm 6 provides a possible implementation of the computational procedure employed to solve problem (4.5)-(4.6), denoted by SIMP$_\mu$. This version of SIMP algorithm is a variant of the basic approach, due to the enrichment with both filtering and sharpening. This choice is justified with a view to the offline phase of the POD algorithm. In particular, to perform the filtering, we adopt the Helmholtz-type partial differential problem

$$\begin{cases} -\tau^2 \Delta \rho_f + \rho_f = \rho_h & \text{in } \Omega \\ \tau^2 \nabla \rho_f \cdot \mathbf{n} = 0 & \text{on } \partial\Omega, \end{cases} \tag{4.7}$$

with τ a real parameter measuring the thickness of the smoothed density, to be properly tuned [33]. In practice, problem (4.7) is discretized with piecewise linear finite elements.

Algorithm 6 : SIMP_μ

Input : `CTOL, kmax, kmax1, kmax2,` τ_1, τ_2, τ_3, β, $\rho_{\min}$, μ

1: Set: $\rho_h^0 = 1$, $\mathtt{k} = 0$
2: **while** $\mathtt{k} <$ `kmax` **do**
3: $\quad \rho_h^{\mathtt{k+1}} = \mathtt{optimize}(\rho_h^{\mathtt{k}}, \mathtt{kmax1}, \mathtt{CTOL}, \rho_{\min}, \mu)$;
4: $\quad \rho_h^{\mathtt{k+1}} = \mathtt{filter}(\rho_h^{\mathtt{k+1}}, \tau_1)$;
5: $\quad$ `k = k+1`;
6: **endwhile**
7: $\rho_h^{\mathtt{k+1}} = \mathtt{optimize}(\rho_h^{\mathtt{k}}, \mathtt{kmax2}, \mathtt{CTOL}, \rho_{\min}, \mu)$;
8: $\rho_h^{\mathtt{k+1}} = \mathtt{filter}(\rho_h^{\mathtt{k+1}}, \tau_2)$;
9: $\rho_h^{\mathtt{k+1}} = \mathtt{sharpening}(\rho_h^{\mathtt{k+1}}, \beta)$;
10: $\rho_h^{\mathtt{k+1}} = \mathtt{filter}(\rho_h^{\mathtt{k+1}}, \tau_3)$;

Concerning the sharpening, we apply the projection step

$$\rho_S = 0.5 \left(1 + \frac{\tanh(\beta(\rho_h - 0.5))}{\tanh(0.5\,\beta)} \right),$$

with β a parameter tuning sharpening features, to emphasize the density gradient, thus yielding a sharper material-void pattern [27, 33, 46]. We observe that sharpening is, in general, applied to a filtered density. The particular alternation of filtering and sharpening adopted in Algorithm 6 will be more precisely justified later on.

Function `optimize` implements a suitable algorithm for constrained minimization. For this purpose, we adopt function `IPOPT` in FreeFem++ [29, 51]. In particular, `CTOL` is a tolerance for the stopping criterion, `kmax1`, `kmax2` set the maximum number of iterations allowed for the optimizer. Routine `IPOPT` requires also the gradient of $\mathcal{G}$ and of $\mathcal{C}$ with respect to the density. For more details about the computation of these gradients, we refer to [40].

According to an offline/online paradigm typical of a POD approach [30, 45], in the offline phase we collect the solutions to the full-size problem by SIMP_μ, called snapshots, into the response matrix, $\mathcal{S}$, for a sufficiently large set of parameters, $\{\mu_i\}_{i=1}^M$. In particular, we are interested in the output density of Algorithm 6, so that

$$\mathcal{S} = [\boldsymbol{\rho}_{\mu_1}^h, \boldsymbol{\rho}_{\mu_2}^h, ..., \boldsymbol{\rho}_{\mu_M}^h] \in \mathbb{R}^{N \times M},$$

with $\dim(V_h) = N < +\infty$, and where $\boldsymbol{\rho}_\mu^h \in \mathbb{R}^N$ collects the degrees of freedom of ρ_μ^h, solution to (4.5)-(4.6), with respect to the basis $\{\varphi_i\}_{i=1}^N$ of V_h. Then, to identify the POD basis we apply the singular value decomposition (SVD) [25] to $\mathcal{S}$,

$$\mathcal{S} = V \Sigma \Phi^T,$$

with $V \in \mathbb{R}^{N\times N}$ and $\Phi \in \mathbb{R}^{M\times M}$ the orthogonal matrices collecting the left and the right singular vectors of $\mathcal{S}$, respectively, while $\Sigma \in \mathbb{R}^{N\times M}$ is the pseudo-diagonal matrix of the singular values of $\mathcal{S}$. The POD basis is thus identified by the first l columns of V, $\{\mathbf{v}_i\}_{i=1}^l$, with $0 < l \leq M$, so that the reduced space $\mathcal{V}_{\text{POD}}^l = \text{span}\{\mathbf{v}_1, \ldots, \mathbf{v}_l\} \subset \mathbb{R}^N$. By exploiting the bijection between V_h and $\mathbb{R}^N$ [13], we define the subspace $V_{h,\text{POD}}^l$ of V_h associated with the subspace $\mathcal{V}_{\text{POD}}^l$ of $\mathbb{R}^N$. As far as the choice of l is concerned, different criteria can be pursued [30, 45]. The role of SVD is to generate a reduced basis which turns out to be particularly effective, by removing the redundancy in the response matrix.

Remark 4.2.1 *A priori one could build a response matrix also for the displacement. We have decided to work with the density matrix only, to contain the computational cost of the offline phase. Additionally, first numerical checks have highlighted a low accuracy for this double reduction. This topic is currently out of the focus of this paper.*

With a view to the online phase, we introduce matrix $V_l = [\mathbf{v}_1, \ldots, \mathbf{v}_l] \in \mathbb{R}^{N\times l}$ collecting the POD basis vectors, so that, with any vector $\mathbf{w}_l \in \mathbb{R}^l$, we can associate an element $\mathbf{w}_N \in \mathbb{R}^N \cap \mathcal{V}_{\text{POD}}^l$ given by

$$\mathbf{w}_N = V_l \, \mathbf{w}_l. \tag{4.8}$$

For any $w_h \in V_{h,\text{POD}}^l$, by exploiting the standard expansion in terms of the finite element basis, $\{\varphi_i\}_{i=1}^N$, it follows that, for a suitable $\mathbf{w}_N$ satisfying (4.8),

$$\begin{aligned} w_h(\mathbf{x}) = \sum_{i=1}^N w_i \, \varphi_i(\mathbf{x}) = \sum_{i=1}^N \Big(V_l \, \mathbf{w}_l \Big)_i \varphi_i(\mathbf{x}) = \sum_{i=1}^N \Big(\sum_{j=1}^l V_{l_{ij}} w_{l_j} \Big) \varphi_i(\mathbf{x}) \\ = \sum_{j=1}^l w_{l_j} \, \tilde{\varphi}_j(\mathbf{x}), \end{aligned}$$

with $\tilde{\varphi}_j(\mathbf{x}) = \sum_{i=1}^{N} V_{l_{ij}}\, \varphi_i(\mathbf{x})$, i.e., $V^l_{h,\mathrm{POD}} = \mathrm{span}\{\tilde{\varphi}_1, \ldots, \tilde{\varphi}_l\} \subset V_h$, and where we denote by w_i the i-th component of $\mathbf{w}_N$.

We now pick a new value for the parameter μ, say $\mu = \mu^*$, with $\mu^* \neq \mu_i$ with $i = 1 \ldots, M$, and we solve the following $\mathrm{SIMP}_{\mu^*,\mathrm{POD}}$ problem

find $\rho^{\mu^*,l}_{h,\mathrm{POD}} \in V^l_{h,\mathrm{POD}}$ such that

$$\min_{\rho^{\mu^*,l}_{h,\mathrm{POD}} \in V^l_{h,\mathrm{POD}}} \mathcal{G}(\mathbf{u}_h(\rho^{\mu^*,l}_{h,\mathrm{POD}})) \; : \begin{cases} a^{\mu^*}_{\rho}(\mathbf{u}_h(\rho^{\mu^*,l}_{h,\mathrm{POD}}), \mathbf{v}_h) = \mathcal{G}^{\mu^*}(\mathbf{v}_h) \;\forall \mathbf{v}_h \in U_h \\ \mathcal{C}^{\mu^*}(\rho^{\mu^*,l}_{h,\mathrm{POD}}, \mathbf{u}_h(\rho^{\mu^*,l}_{h,\mathrm{POD}})) \leq 0 \end{cases} \tag{4.9}$$

instead of the SIMP_{μ^*} in (4.5)-(4.6). Solution $\rho^{\mu^*,l}_{h,\mathrm{POD}}$ thus provides an approximation for $\rho^{\mu^*}_h$. The computational benefit expected from this procedure can be ascribed to the fact that (4.9) involves a constrained minimization problem of dimension l instead of N, in general being $l \ll N$. This implies that few iterations are required to converge. The challenge will be to assess also the reliability of the POD solution.

From an implementative viewpoint, $\mathrm{SIMP}_{\mu^*,\mathrm{POD}}$ is described by the following variant of Algorithm 6:

Algorithm 7 : $\mathrm{SIMP}_{\mu^*,\mathrm{POD}}$

Input : `CTOL`, `kmax`, β, $\rho_{\min}$, μ^*

1: Set: $\rho^0_h = 1$;
2: $\rho^1_h = \texttt{optimize}(\rho^0_h, \texttt{kmax}, \texttt{CTOL}, \rho_{\min}, \mu^*)$;
3: $\rho^1_h = \texttt{sharpening}(\rho^1_h, \beta)$;
4: Set: $\rho^{\mu^*,l}_{h,\mathrm{POD}} = \rho^1_h$;

The whole POD procedure, labeled in the sequel by SIMPOD, is itemized in Algorithm 8. We remark that the online phase turns out to be effective if the POD basis does not consist of high-frequency modes. This can be achieved by employing smooth snapshots with a sufficiently sharp interface between void and material. Actually, the optimizer returns jagged boundaries when no filtering and sharpening are adopted, with associated highly oscillating POD modes. This justifies the tight combination of optimization with filtering and sharpening in SIMP_μ algorithm.

The effort performed offline allows us to avoid any filtering in the online phase, while keeping only sharpening.

Algorithm 8 : SIMPOD

Input : M, $\{\mu_{\mathtt{i}}\}_{\mathtt{i=1}}^{\mathtt{M}}$, l, μ^*

Set: $\mathcal{S} = []$;
for i=1:M **do**
    $\rho_h^{\mu_{\mathtt{i}}}$=SIMP$_{\mu_{\mathtt{i}}}$;
    $\mathcal{S} = [\mathcal{S}, \boldsymbol{\rho}_h^{\mu_{\mathtt{i}}}]$;
endfor
$[V, \Sigma, \Phi] =$ svd($\mathcal{S}$);
construct space $V_{h,\mathrm{POD}}^{\mathtt{l}}$;
$\rho_{h,\mathrm{POD}}^{\mu^*,\mathtt{l}}$ = SIMP$_{\mu^*,\mathrm{POD}}$;

4.2.3 Numerical results for SIMPOD

We focus on the topology optimization of two different structures, namely a cantilever beam and a bridge. The parameter μ will assume a different meaning, being associated with either the state equation or the inequality constraint.

Concerning the input values for Algorithms 6-7, we refer to Table 4.1, except for the parameter μ and μ^*, changing through the test-cases.

SIMP$_\mu$	SIMP$_{\mu^*,\mathrm{POD}}$
CTOL= $5 \cdot 10^{-3}$	CTOL= $5 \cdot 10^{-3}$
kmax= 3	kmax= 300
kmax1= 50	$\beta = 7.5$
kmax2= 150	$\rho_{\min} = 0.01$
$\tau_1 = 0.04$	
$\tau_2 = 0.025$	
$\tau_3 = 0.02$	
$\beta = 5$	
$\rho_{\min} = 0.01$	

Table 4.1: Input values for SIMP$_\mu$ and SIMP$_{\mu^*,\mathrm{POD}}$ algorithms.

The SIMPOD cantilever beam

We consider the rectangular domain $\Omega = (0,2) \times (0,1) \subset \mathbb{R}^2$, with $\mathbf{x} = [x,y]^T \in \Omega$. The clamped portion of the boundary is $\Gamma_D = \{(x,y) : x = 0, 0 \leq y \leq 1\}$, the traction $\mathbf{f} = [0,-100]^T$ is imposed on $\Gamma_N = \{(x,y) : x = 2, 0.45 \leq y \leq 0.55\}$, while the material constants are $E = 1000$ and $\nu = 1/3$. A triangular structured mesh consisting of 8100 elements discretizes the domain Ω, N being equal to 4186.

We first choose for parameter μ in (4.5)-(4.6) the volume fraction, α. The response matrix is assembled with $M = 20$ snapshots, uniformly sampled in the interval $\mathcal{I}_\alpha = [0.2, 0.675]$. For the online phase, we select two new values for the volume fraction, namely, $\mu_1^* = \alpha_1^* = 0.222$ and $\mu_2^* = \alpha_2^* = 0.578$.

Figures 4.1 and 4.2, top-left show the full reference solutions, $\rho_h^{0.222}$ and $\rho_h^{0.578}$, respectively, both computed via Algorithm 6 after skipping the last filtering step and with the same inputs as in Table 4.1. The other panels in the same figures provide the POD density for the values of l in Tables 4.2 and 4.3. The main difference between the two cases is that, while 4 POD modes suffice to detect the topology for the structure in Figure 4.1, the more complex layout of the cantilever in Figure 4.2 requires at least 16 modes.

From a quantitative viewpoint, we collect information of interest in Tables 4.2 and 4.3, i.e., the CPU time (in seconds[1]), the compliance, $\mathcal{G}$, and the number of iterations demanded by SIMP_{μ^*} and $\text{SIMP}_{\mu^*,\text{POD}}$ to converge, where, for SIMP_{μ^*}, the sum of the iterations involved in the four runs of `optimize` is understood. The values in the two tables exhibit a different trend. For the smaller volume fraction, a few iterations are demanded by the POD procedure, with a consequent reduced CPU time compared with $\text{SIMP}_{\mu_1^*}$ (by a factor 8 in the worst case and 20 for $l = 4$). Nevertheless, the estimated compliance is more than double compared with the reference value, 15.7588. For the larger value of α^*, the predicted compliance is more reliable (with a mismatch of about 14%). Moreover, few iterations suffice to compute the reference solution.

The numerical verification provides a partial justification to the different behaviour in the tables. Actually, the smaller the volume fraction, the larger the number of iterations required by SIMP_{μ^*} to converge, whereas the time demanded by the POD approach essentially scales in the same way for both the configurations.

[1]The computations have been run on a GenuineIntel Pentium(R) Dual-Core CPU E6300 2.80 GHz 4GB RAM desktop computer.

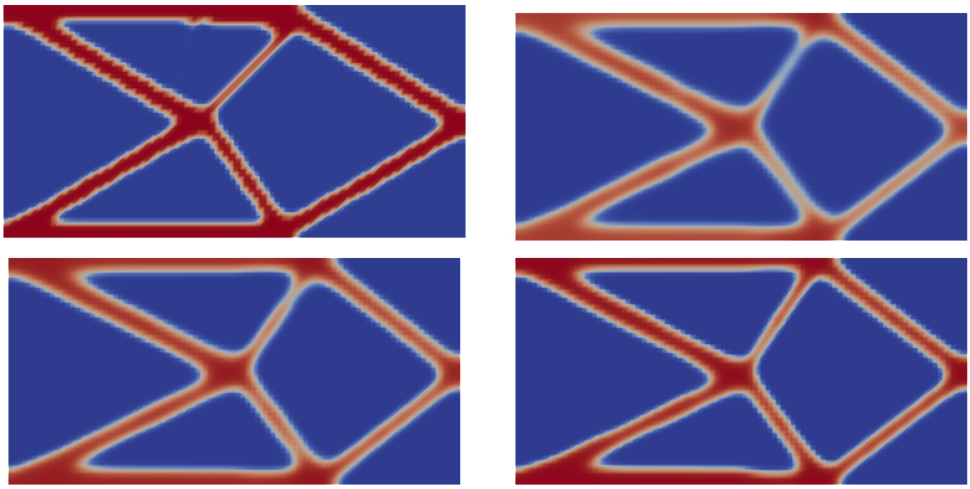

Figure 4.1: SIMPOD cantilever test case - volume fraction α_1^*: reference solution (top-left); POD solution for $l = 4$ (top-right), $l = 7$ (bottom-left) and $l = 13$ (bottom-right).

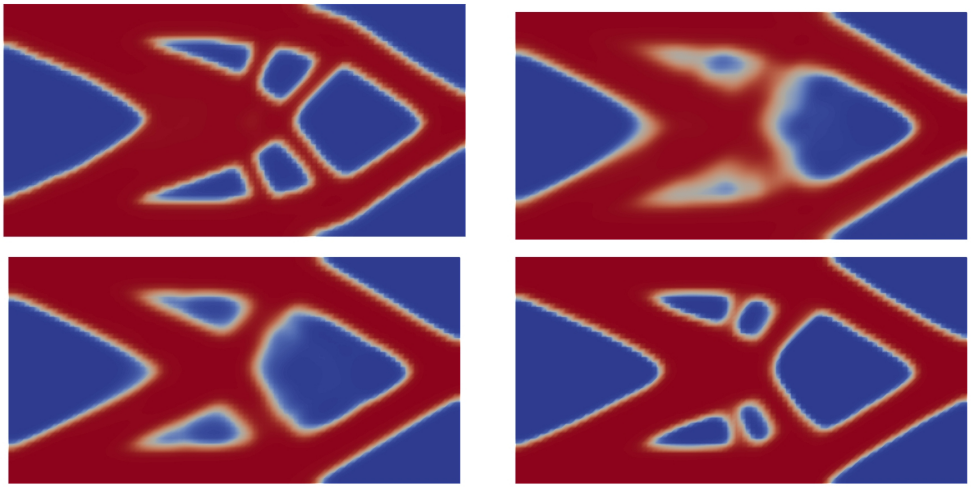

Figure 4.2: SIMPOD cantilever test case - volume fraction α_2^*: reference solution (top-left); POD solution for $l = 1$ (top-right), $l = 5$ (bottom-left) and $l = 16$ (bottom-right).

	CPU time [s]	$\mathcal{G}$	#iterations
$\text{SIMP}_{\mu_1^*}$	140.71	15.7588	198
$l = 4$	7.27	55.3057	14
$l = 7$	11.14	44.1419	20
$l = 13$	16.58	36.0107	28

Table 4.2: SIMPOD cantilever test case - volume fraction α_1^*: quantitative data for $\text{SIMP}_{\mu_1^*}$ and $\text{SIMP}_{\mu_1^*,\text{POD}}$ algorithms.

	CPU time [s]	$\mathcal{G}$	#iterations
$\text{SIMP}_{\mu_2^*}$	41.95	4.9978	59
$l = 1$	4.52	6.8983	9
$l = 5$	10.83	6.1095	20
$l = 16$	27.14	5.7209	28

Table 4.3: SIMPOD cantilever test case - volume fraction α_2^*: quantitative data for $\text{SIMP}_{\mu_2^*}$ and $\text{SIMP}_{\mu_2^*,\text{POD}}$ algorithms.

	CPU time [s]	$\mathcal{G}$	#iterations
SIMP_{μ^*}	56.11	6.5420	79
$l = 1$	3.88	22.0962	8
$l = 2$	5.55	9.5097	11
$l = 3$	14.04	8.4831	27
$l = 5$	10.35	7.6995	18
$l = 8$	16.50	7.5410	16

Table 4.4: SIMPOD cantilever test case - traction position: quantitative data for SIMP_{μ^*} and $\text{SIMP}_{\mu^*,\text{POD}}$ algorithms.

We now make a different choice for parameter μ, namely we pick the position, y_f, where the traction is applied. Consequently, the Neumann boundary becomes $\Gamma_N = \{(x, y) : x = 2, |y - y_f| \leq 0.05\}$ and α is now set to 0.5. Matrix $\mathcal{S}$ is built starting from $M = 11$ snapshots, and selecting y_f uniformly in the interval $[0, 1]$. For the online phase, we choose $\mu^* = y_f^* = 0.111$. The reference topology is shown in Figure 4.3, top-left.

Figure 4.3, top-right, center and bottom, provides the layout predicted by SIMPOD algorithm for the five values of l in Table 4.4. We remark that only two modes provide a layout with the same topology as the reference

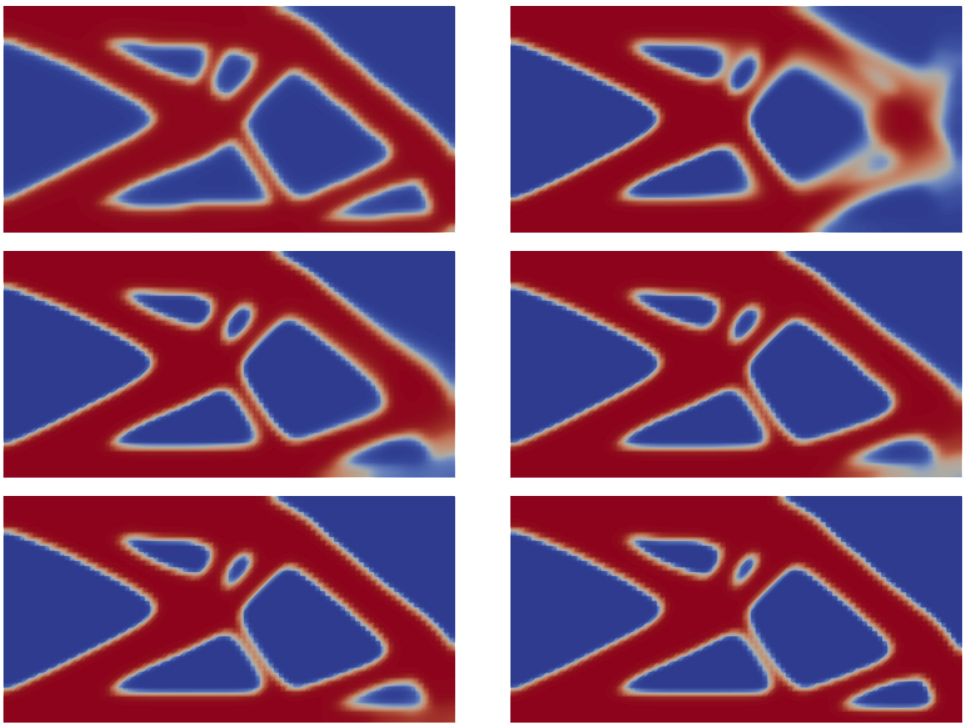

Figure 4.3: SIMPOD cantilever test case - traction position: reference solution (top-left); POD solution for $l = 1$ (top-right), $l = 2$ (center-left), $l = 3$ (center-right), $l = 5$ (bottom-left) and $l = 8$ (bottom-right).

structure, except for some detail in the bottom-right portion of Ω. Eventually, 8 POD modes furnish an accurate prediction for the expected cantilever, as confirmed also by the quantitative analysis in Table 4.4. Actually, the reduction of the computational time amounts to a factor of about 3.4, while the discrepancy on the compliance is about 15%.

The SIMPOD bridge

This second test case deals with the optimization of a bridge. The domain is $\Omega = (0, 6) \times (0, 1)$, discretized with an isotropic triangular mesh consisting of 11260 elements, with $N = 5840$. The traction $\mathbf{f} = [0, -100]^T$ is imposed on the portion $\Gamma_N = \{(x, y) : 2.9 \leq x \leq 3.1, y = 1\}$ of the boundary. On $\Gamma_{D_1} = \{(x, y) : 0 \leq x \leq 0.06, y = 0\}$ we impose that the vertical displacement

is null to model a roller, whereas on $\Gamma_{D_2} = \{(x, y) : 5.94 \leq x \leq 6\}$ both the components of the displacements are set to zero. Finally, the material constants are $E = 1000$ and $\nu = 1/3$ as for the cantilever test case.

The parameter adopted for the POD analysis is the volume fraction, α. The offline phase is performed with SIMP$_\mu$ algorithm with the same input values as in Table 4.1, except for τ_3 which is now set to 0.05, and choosing $M = 20$ values of μ evenly distributed in $\mathcal{I}_\alpha = [0.2, 0.675]$. The parameter selected for the online phase is $\alpha^* = 0.362$.

Figure 4.4, top-left exhibits the reference solution together with three predictions corresponding to an increasing number of POD modes. At least, 12 modes have to be employed to obtain a somewhat accurate prediction, as shown in Figure 4.4, top-right and bottom.

Concerning the data in Table 4.5, the computational saving provided by SIMPOD is about eight times in the worst case, even though the predicted compliance is not so accurate, differing from the reference one of about 19% for the largest value of l ($l = 12$).

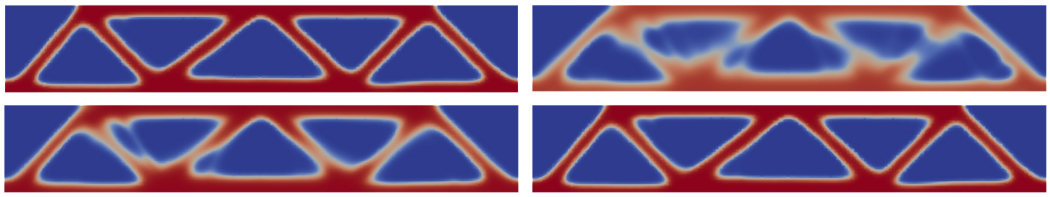

Figure 4.4: SIMPOD bridge test case - volume fraction: reference solution (top-left); POD solution for $l = 1$ (top-right), $l = 2$ (bottom-left), $l = 12$ (bottom-right).

	CPU time [s]	$\mathcal{G}$	#iterations
SIMP$_{\mu^*}$	227.53	63.6929	273
$l = 1$	5.4	158.1365	8
$l = 2$	10.23	107.4605	14
$l = 12$	28.57	75.7358	35

Table 4.5: SIMPOD bridge test case - volume fraction: quantitative data for SIMP$_{\mu^*}$ and SIMP$_{\mu^*,\text{POD}}$ algorithms.

4.3 An enhanced approach

In the previous section, a basic-POD approach for topology optimization has been proposed and verified. As the numerical experiments show, the algorithm succeeds in remarkably reducing the computational time, delivering a reliable result, yet rough and, in general, less performing with respect to the reference solution if the number of POD modes is not sufficiently large. To overcome this limit, it is standard to resort to a larger number of snapshots. This option can be prohibitive in terms of memory usage, since the number of entries in $\mathcal{S}$ linearly depends on the number of snapshots, and the optimal value for both M and l is, in general, not known a priori.

As an alternative, we here propose a new approach, where the output of SIMPOD is used as the initial guess, cheap and rough, for a new run of a topology optimization procedure, in the spirit of a predictor-corrector method, named PC-SIMPOD.

4.3.1 A predictor-corrector SIMPOD (PC-SIMPOD) technique enriched with mesh adaptation

The scheme here proposed exploits the advantages of SIMPOD (predictor) to quickly obtain an initial guess (more accurate than a dummy choice) for the optimization of the structure, so that the topology optimizer (corrector) can be initialized in a neighbourhood of the solution. The expected result of such a combination is that a few optimization iterations in the correction step suffice to deliver a solution that is competitive with the one directly produced by the SIMP method on a generic initial guess.

In particular, for the correction step, we adopt the adaptive version of SIMP algorithm, namely SIMPATY, proposed in [39, 40], where the employment of a fixed mesh as in Section 4.2.3 is replaced by a grid which sharply follows the boundaries of the structure to be optimized. As shown in [20, 40], the main benefit of SIMPATY is to yield sharp layouts characterized by smooth material/void boundaries, almost ready for the 3D printing process. This is achievable using an anisotropic mesh adaptation procedure driven by a sound mathematical tool, namely an a posteriori error estimator.

Anisotropic meshes allow us to properly tune the size of mesh elements together with the corresponding shape and orientation. To get all this information, we resort to the setting used in [17, 21, 22, 38], based on the affine

transformation $T_K : \hat{K} \to K$, mapping the equilateral reference element $\hat{K}$ inscribed in the unit circle, into a generic element K of $\mathcal{T}_h$,

$$\mathbf{x} = T_K(\hat{\mathbf{x}}) = M_K \hat{\mathbf{x}} + \mathbf{b}_K \quad \forall \hat{\mathbf{x}} \in \hat{K},$$

where $M_K \in \mathbb{R}^{2\times 2}$ deforms and rotates the reference element and $\mathbf{b}_K$ shifts it. The Jacobian M_K can be factorized by successively applying the polar and the spectral decomposition, so that

$$M_K = (R_K^T \Lambda_K R_K) Z_K,$$

where $Z_K \in \mathbb{R}^{2\times 2}$ is a rotation matrix, $\Lambda_K = \mathrm{diag}(\lambda_{1,K}, \lambda_{2,K}) \in \mathbb{R}^{2\times 2}$ collects the eigenvalues of the symmetric positive definite matrix $R_K^T \Lambda_K R_K$, with $\lambda_{1,K} \geq \lambda_{2,K}$, and $R_K^T = [\mathbf{r}_{1,K}, \mathbf{r}_{2,K}] \in \mathbb{R}^{2\times 2}$ is the orthogonal matrix of the corresponding eigenvectors. Matrices Λ_K and R_K contain the geometric features of the element K, namely the length, $\lambda_{i,K}$, of the semi-axes of the ellipse circumscribed to K, and the directions, $\mathbf{r}_{i,K}$, of such axes, with $i = 1, 2$ (see Figure 4.5). Triangle K is thus fully identified by the three quantities $\{\lambda_{1,K}, \lambda_{2,K}, \mathbf{r}_{1,K}\}$. The aspect ratio $s_K = \lambda_{1,K}/\lambda_{2,K} \geq 1$ provides a measure of the deformation of the element, with the understanding that high values for s_K are associated with very stretched elements.

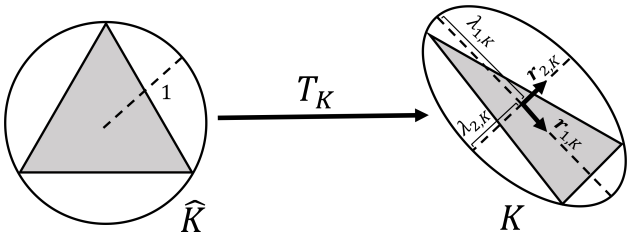

Figure 4.5: Map T_K from the reference element $\hat{K}$ to the generic one K.

SIMPATY algorithm relies on a posteriori error estimator to generate the anisotropic adapted mesh. We resort to an anisotropic variant of the recovery-based error estimator proposed by O.C. Zienkiewicz and J.Z. Zhu in [59, 60, 61], following [36, 38]. In particular, the estimator η for the $H^1(\Omega)$-seminorm of the density discretization error, $|\rho - \rho_h|_{H^1(\Omega)}$, is given by

$$\eta^2 = \sum_{K\in\mathcal{T}_h} \eta_K^2,$$

with

$$\eta_K^2 = \frac{1}{\lambda_{1,K}\lambda_{2,K}} \sum_{i=1}^{2} \lambda_{i,K}^2 \left(\mathbf{r}_{i,K}^T \, G_{\Delta_K}\big(E_\nabla\big) \mathbf{r}_{i,K} \right) \tag{4.10}$$

the element contribution, and where $E_\nabla = [P(\nabla\rho_h) - \nabla\rho_h]_{\Delta_K}$ is the recovered error,

$$P(\nabla\rho_h)|_K = \frac{1}{|\Delta_K|} \sum_{T\in\Delta_K} |T| \, \nabla\rho_h|_T$$

is the recovered gradient associated with K, obtained via an area-weighted average of the gradient of ρ_h computed on the patch Δ_K of the elements sharing at least one vertex with K, $|\Delta_K|$ is the area of Δ_K and $G_{\Delta_K}(\cdot) \in \mathbb{R}^{2\times 2}$ is the symmetric positive semidefinite matrix with entries

$$[G_{\Delta_K}(\mathbf{w})]_{i,j} = \sum_{T\in\Delta_K} \int_T w_i \, w_j \, dT \quad \text{with } i,j = 1,2, \tag{4.11}$$

for any vector-valued function $\mathbf{w} = (w_1, w_2)^T \in [L^2(\Omega)]^2$.

Estimator η is then turned into a practical information to build the new adapted mesh. This is carried out via a metric-based procedure [24], which aims at minimizing the number of elements to ensure a certain accuracy, $\eta \leq \texttt{TOL}$, in combination with an equidistribution of the error over the triangles. This leads to the prediction of the optimal spacing, $\{\lambda_{i,K}^{\text{opt}}\}_{i=1}^2$, and orientation, $\{\mathbf{r}_{i,K}^{\text{opt}}\}_{i=1}^2$, for each element K of the mesh via an iterative procedure. This can be accomplished following [37], so that

$$\lambda_{1,K}^{\text{opt}} = g_2^{-1/2} \left(\frac{\texttt{TOL}^2}{2\#\mathcal{T}_h \, |\widehat{\Delta}_K|} \right)^{1/2}, \quad \lambda_{2,K}^{\text{opt}} = g_1^{-1/2} \left(\frac{\texttt{TOL}^2}{2\#\mathcal{T}_h \, |\widehat{\Delta}_K|} \right)^{1/2}, \tag{4.12}$$
$$\mathbf{r}_{1,K}^{\text{opt}} = \mathbf{g}_2, \quad \mathbf{r}_{2,K}^{\text{opt}} = \mathbf{g}_1,$$

with $|\widehat{\Delta}_K| = |\Delta_K|/(\lambda_{1,K}\lambda_{2,K})$, and where $\{g_i, \mathbf{g}_i\}_{i=1,2}$ are the eigenvalue-eigenvector pairs associated with the scaled matrix $\widehat{G}_{\Delta_K}(E_\nabla) = G_{\Delta_K}(E_\nabla)/|\Delta_K|$, with $g_1 \geq g_2 > 0$, $\{\mathbf{g}_i\}_{i=1,2}$ orthonormal vectors, and $\#\mathcal{T}_h$ denotes the cardinality of the mesh elements.

The spacing and the orientation thus predicted, $\{\lambda_{i,K}^{\text{opt}}, \mathbf{r}_{i,K}^{\text{opt}}\}_{i=1}^2$, become the input to a metric-based mesh generator which produces the new anisotropic adapted mesh. The process is repeated in an iterative loop, until some convergence criterion is met.

The PC-SIMPOD with mesh adaptation procedure is itemized in Algorithm 9.

Algorithm 9 : PC-SIMPOD with anisotropic mesh adaptation

Input : $\texttt{MTOL}, \texttt{CTOL}, \texttt{TOL}, \texttt{kmax}, \rho_{\min}, \mathcal{T}_h^0, \mu^*, \texttt{l}$

1: $\texttt{k} = 0$, errM $= 1 + \texttt{MTOL}$;
2: Compute $\rho_{h,POD}^{\mu^*,\texttt{l}}$ with Algorithm 8;
3: Set $\rho_h^0 = \rho_{h,POD}^{\mu^*,\texttt{l}}$;
4: **while** errM $>$ MTOL & k $<$ kmax **do**
5: kmax1=20-3k;
6: $\rho_h^{\texttt{k}+1} = \texttt{optimize}(\rho_h^{\texttt{k}}, \texttt{kmax1}, \texttt{CTOL}, \rho_{\min}, \mu^*)$;
7: $\mathcal{T}_h^{\texttt{k}+1} = \texttt{adapt}(\mathcal{T}_h^{\texttt{k}}, \rho_h^{\texttt{k}+1}, \texttt{TOL})$;
8: errM $= |\#\mathcal{T}_h^{\texttt{k}+1} - \#\mathcal{T}_h^{\texttt{k}}|/\#\mathcal{T}_h^{\texttt{k}}$;
9: $\texttt{k} = \texttt{k} + 1$;
10: **endwhile**

The routine `adapt` in line 7: generates the new adapted mesh identified by the optimal spacing and orientation in (4.12). Concerning the stopping criterion, we rely on the stagnation of the cardinality of the elements between two consecutive meshes, to within the tolerance `MTOL`. We remark that an interpolation of the density onto the new adapted mesh is understood at each change of the grid before restarting the procedure (see [40] for more details). Moreover, neither filtering nor sharpening are applied in this algorithm, since mesh adaptation automatically provides smooth structures which avoid the employment of these procedures.

4.3.2 Numerical results for PC-SIMPOD

We show here the improvements led by Algorithm 9 in terms of accuracy on the test-cases in Section 4.2.3 and 4.2.3.

The PC-SIMPOD cantilever beam

We adopt as predictor density the output of SIMPOD algorithm for two different values of l.
The scenario to be recovered is the same as in Figure 4.3, where the selected

parameter coincides with the traction position, namely $\mu^* = 0.111$. In more detail, we start from the two less accurate POD approximations in Figure 4.3, namely $\rho_h^0 = \rho_{h,POD}^{\mu^*,1}$ and $\rho_h^0 = \rho_{h,POD}^{\mu^*,2}$. Concerning the input parameters for Algorithm 9, we set

$$\texttt{MTOL} = 0.01, \quad \texttt{CTOL} = 10^{-4}, \quad \texttt{TOL} = 0.125, \quad \texttt{kmax} = 4, \quad \rho_{\min} = 0.01,$$

while $\mathcal{T}_h^0$ coincides with the structured mesh of 8100 triangles in Section 4.2.3.

For the sake of comparison, the new reference solution coincides with the output of Algorithm 9, skipping step 2:, and directly setting ρ_h^0 in 3: as the approximation provided by SIMP_{μ^*} (see Figure 4.6, top).

Figure 4.6, center-bottom shows the output of PC-SIMPOD for $l = 1$ and $l = 2$, respectively. We remark that the PC-SIMPOD approximation for $l = 1$ is very close to the reference structure even though the initial guess, $\rho_{h,POD}^{\mu^*,1}$, is poor. The final topology is slightly different from the expected one because of the presence of an additional hole in the bottom-right corner, and it also exhibits a bent contour in correspondence with the traction application point.

Starting from a barely richer initial guess is enough to obtain a much more accurate layout, as shown in the bottom panel of the figure. Concerning the computational mesh, it is evident that the anisotropic features allow us to detect the void/material interface in a sharp manner and yield a smooth layout.

	CPU time [s]	$\mathcal{G}$	T_C [s]	$\#\texttt{iter}_C$	$\#\mathcal{T}_h$	$\max_K s_K$
SIMP_{μ^*}	113.72	5.1831	59.32	61	5802	564.43
$l = 1$	51.09	6.5215	47.39	45	5920	97.33
$l = 2$	62.36	5.6006	57.06	58	5438	345.58

Table 4.6: PC-SIMPOD cantilever test case - traction position: quantitative data for PC-SIMPOD for different choices of ρ_h^0.

Table 4.6 enriches the quantities in the previous tables with additional information, namely the time, T_C, required by the **while** loop in Algorithm 9, the total number, $\#\texttt{iter}_C$, of iterations of `optimize` in the corrector step, the mesh cardinality, $\#\mathcal{T}_h$, and the maximum aspect ratio, $\max_K s_K$, of the final anisotropic adapted mesh.

The total CPU time demanded by PC-SIMPOD for $l = 1, 2$, is essentially half the time associated with the same procedure starting from $\rho_h^0 = \text{SIMP}_{\mu^*}$.

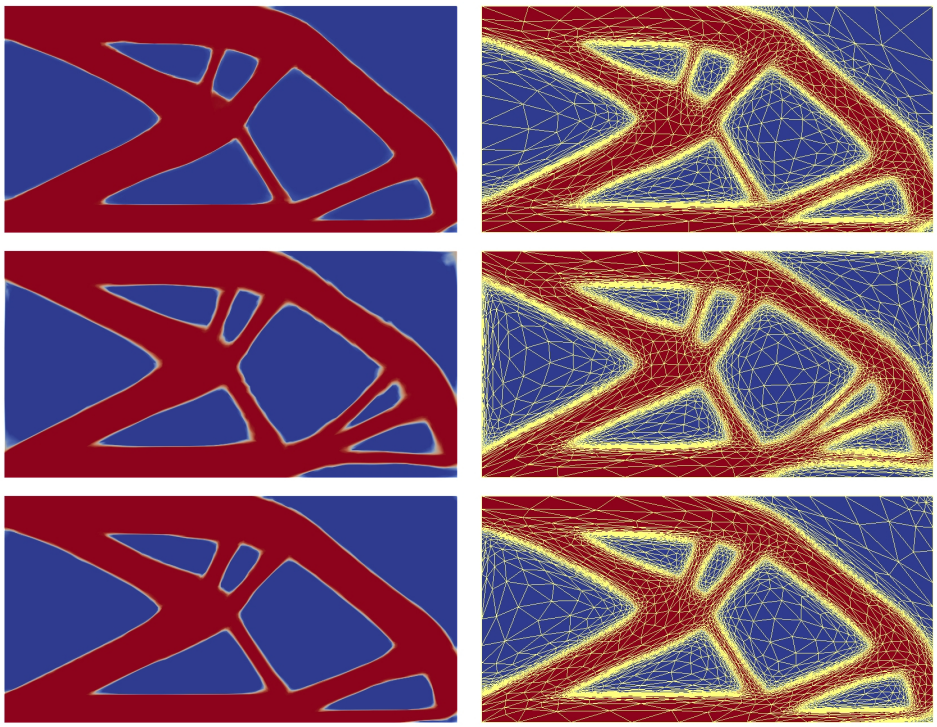

Figure 4.6: PC-SIMPOD cantilever test case - traction position: density (left) and density superposed to the mesh (right) when ρ_h^0 =SIMP$_{\mu^*}$ (top), $\rho_h^0 = \rho_{h,POD}^{\mu^*,1}$ (center), $\rho_h^0 = \rho_{h,POD}^{\mu^*,2}$ (bottom).

As expected, most of the computational time is spent in the **while** loop. The maximum discrepancy in the compliance is of about +10% with respect to the reference configuration. The adaptive procedure delivers in all the three cases meshes with a similar number of triangles, which are, in general, highly stretched.

The PC-SIMPOD bridge

We aim at reconstructing the structure in Figure 4.4, top-left starting from the SIMPOD approximation in the bottom-right panel of the same figure (namely, $\mu^* = 0.362$). Algorithm 9 is slightly modified by setting `kmax1`=15

for all iterations, and choosing as input values

$$\texttt{MTOL} = 0.01, \quad \texttt{CTOL} = 10^{-4}, \quad \texttt{TOL} = 0.1, \quad \texttt{kmax} = 12, \quad \rho_{\min} = 0.01,$$

with $\mathcal{T}_h^0$ the same mesh used for SIMPOD.
The reference solution, shown in Figure 4.7, top, is computed via Algorithm 9 directly setting the initial guess, ρ_h^0, for the density as the approximation delivered by SIMP_{μ^*}.

Figure 4.7 shows the good matching between the reference and the PC-SIMPOD solutions despite some local differences can be detected. However, these heterogeneities do not affect the mechanical performance of the layout yielded by the predictor. Actually, the compliance of the PC-SIMPOD bridge is thoroughly comparable with the reference value, while the gain in terms of computational time is remarkable (the CPU time is, in practice, halved).

Finally, the anisotropic mesh is highly stretched as confirmed by the values of the maximum stretching factors in Table 4.7.

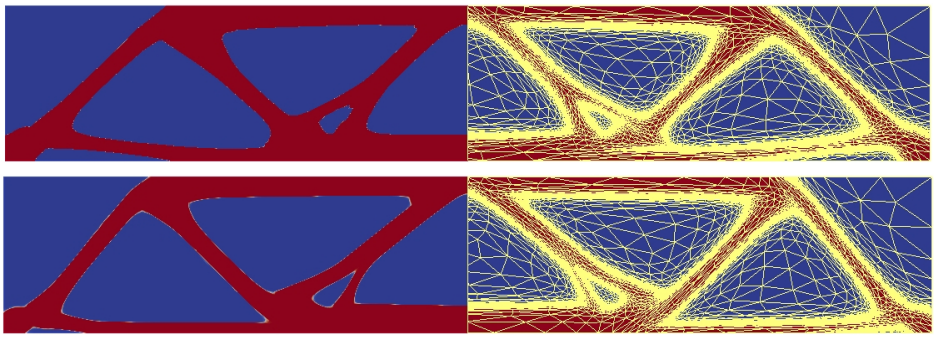

Figure 4.7: PC-SIMPOD bridge test case - volume fraction: density (left) and density superposed to the mesh (right) when $\rho_h^0 = \text{SIMP}_{\mu^*}$ (top), $\rho_h^0 = \rho_{h,POD}^{\mu^*,12}$ (bottom).

	CPU time [s]	$\mathcal{G}$	T_C [s]	$\#\texttt{iter}_C$	$\#\mathcal{T}_h$	$\max_K s_K$
SIMP_{μ^*}	342.67	29.9937	115.02	62	32480	1540.80
$l = 12$	156.49	30.9364	104.66	58	43308	1310.30

Table 4.7: PC-SIMPOD bridge test case - volume fraction: quantitative data for PC-SIMPOD for two choices of ρ_h^0.

4.4 Multi-parameter topology optimization

In Sections 4.2 and 4.3, we have focused on the case where structure optimization depends on just one parameter. Nevertheless, realistic configurations involve more parameters, simultaneously. For instance, with reference to test cases tackled in the previous sections, it could be of interest to identify the optimal configuration for a new pair (α, y_f).

From a formal viewpoint, SIMP$_\mu$ formulation can be rewritten as in (4.5)-(4.6) simply by replacing the scalar parameter μ by the q-dimensional vector of parameters, $\boldsymbol{\mu} = [\mu^1, \mu^2, ..., \mu^q]^T \in \mathbb{R}^q$. In practice, for each parameter μ^j, we consider S_j different values, $\mu^j_{i_j}$, with $i_j = 1, \ldots, S_j$ and $j = 1, \ldots, q$. SIMP$_\mu$ algorithm is then employed to generate a discrete density $\rho_h^{\boldsymbol{\mu}_\mathbf{I}}$ for each parameter $\boldsymbol{\mu}_\mathbf{I} = [\mu^1_{i_1}, \mu^2_{i_2}, \ldots, \mu^q_{i_q}]^T \in \mathbb{R}^q$ where $\mathbf{I} = [i_1, i_2, \ldots, i_q]^T \in \mathbb{N}^q$, with $i_1 = 1, \ldots, S_1$, $i_2 = 1, \ldots, S_2$, $i_q = 1, \ldots, S_q$. The offline phase thus collects a total of $M = S_1\, S_2\, \ldots S_q$ snapshots that have to be properly gathered into a generalization of the standard response matrix usually referred to as atlas, $\mathcal{A}$. With this aim, several approaches can be employed, ranging from an arbitrary organization of the densities $\rho_h^{\boldsymbol{\mu}_\mathbf{I}}$ into a two-dimensional $(N \times M)$ matrix to a q-dimensional array. The first approach is viable if q is small and the standard SVD can be employed to extract the POD basis. In such a case, the ordering of $\rho_h^{\boldsymbol{\mu}_\mathbf{I}}$ in $\mathcal{A}$ is arbitrary. We adopt the index ordering based on the following `for` loops:

```
for i1 = 1:S1
     for i2 = 1:S2
          ...
             for iq = 1:Sq
                  ...
             end
     end
end
```

On the contrary, for large values of q, the approach based on the q-dimensional array turns out to be advisable and a Higher-Order SVD (HOSVD) can be adopted as a more performing procedure to extract the reduced basis [14, 31].

Since we limit the numerical assessment to the case of two parameters,

we define $\mathcal{A}$ as

$$\mathcal{A} = \left[\boldsymbol{\rho}_h^{\mu_1^1\mu_1^2}, ..., \boldsymbol{\rho}_h^{\mu_1^1\mu_{S_2}^2}, \boldsymbol{\rho}_h^{\mu_2^1\mu_1^2}, ..., \boldsymbol{\rho}_h^{\mu_2^1\mu_{S_2}^2}, ..., \boldsymbol{\rho}_h^{\mu_{S_1}^1\mu_1^2}, ..., \boldsymbol{\rho}_h^{\mu_{S_1}^1\mu_{S_2}^2}\right],$$

where the generic density $\boldsymbol{\rho}_h^{\mu_{i_1}^1\mu_{i_2}^2}$ is the output of the multi-parameter version, multi-SIMP$_{\boldsymbol{\mu}}$, of Algorithm 6, with μ replaced by the vector $\boldsymbol{\mu} = [\mu_{i_1}^1, \mu_{i_2}^2]^T$, and we apply the standard SVD to $\mathcal{A}$ to extract the POD basis.

The online phase is started by selecting the new multi-parameter, $\boldsymbol{\mu}^* = [\mu^{*,1}, \mu^{*,2}, ..., \mu^{*,q}]^T \in \mathbb{R}^q$, and by resorting to the multi-parameter version, multi-SIMP$_{\boldsymbol{\mu}^*,\text{POD}}$, of SIMP$_{\mu^*,\text{POD}}$.

We will refer to the whole procedure here described as multi-SIMPOD. In a straightforward way, we can generalize the PC-SIMPOD procedure enriched with anisotropic mesh adaptation to the multi-parameter case, denoting the resulting procedure by multi-PC-SIMPOD.

Goal of the next section is to investigate the performances of both multi-SIMPOD and multi-PC-SIMPOD methods.

4.4.1 Numerical results for multi-SIMPOD and multi-PC-SIMPOD

We first check the performances of multi-SIMPOD algorithm focusing on the cantilever test case in Section 4.2.3, and by choosing as multi-parameter $\boldsymbol{\mu} = [\mu^1, \mu^2]^T = [\alpha, y_f]^T$. We investigate the sensitivity of the predicted layout to two different atlas consisting of 25 and 50 snapshots. For the first atlas, $\mathcal{A}_1$, we set $S_1 = S_2 = 5$ and

$$\mu^1 \in \{0.3, 0.4, 0.5, 0.6, 0.7\}, \quad \mu^2 \in \{0, 0.25, 0.5, 0.75, 1\}.$$

For the second atlas, $\mathcal{A}_2$, $S_1 = 10$ and $S_2 = 5$ corresponding to the following samplings

$$\mu^1 \in \{0.3, 0.325, 0.35, 0.375, 0.4, 0.45, 0.5, 0.55, 0.575, 0.6\},$$
$$\mu^2 \in \{0, 0.25, 0.5, 0.75, 1\}.$$

The input parameters for SIMP$_\mu$ are the same as in Table 4.1, except for τ_3 and β now set to 0.0286 and 10, respectively, while SIMP$_{\mu^*,\text{POD}}$ shares all the input values. The computational mesh is the structured one as in Section 4.2.3. The online multi-parameter is $\boldsymbol{\mu}^* = [\mu^{*,1}, \mu^{*,2}]^T = [0.333, 0.444]^T$. As reference structure, we consider the output provided by multi-SIMP$_{\boldsymbol{\mu}^*}$.

Figure 4.8 and Table 4.8 summarize the output of multi-SIMPOD procedure from a qualitative and quantitative viewpoint, respectively. Entries in Table 4.8 preserve the same meaning as for the previous test cases. At least 5 POD modes have to be adopted to correctly identify the traction area, while almost all of the 25 modes are required to obtain a reliable prediction of the layout.

Similarly to the single-parameter setting, we observe a bad prediction of the mechanical stiffness which is about 140% higher in the multi-SIMPOD case ($l = 22$) with respect to the reference configuration. The computational time reduces, however, by a factor 8.

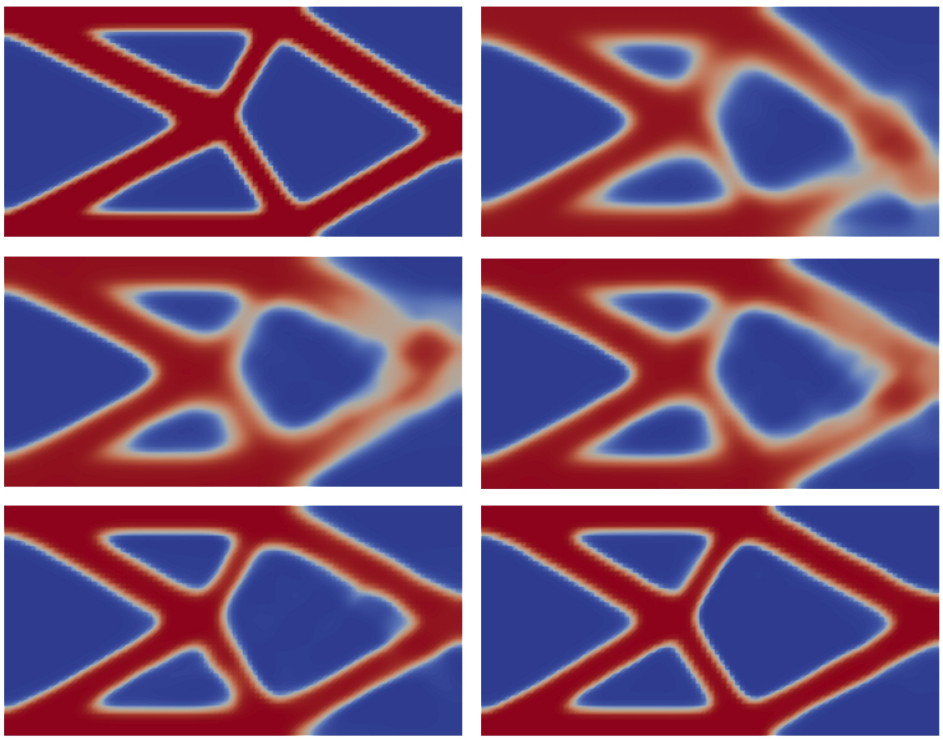

Figure 4.8: multi-SIMPOD cantilever test case for atlas $\mathcal{A}_1$: reference solution (top-left); POD solution for $l = 3$ (top-right), $l = 4$ (center-left), $l = 5$ (center-right), $l = 13$ (bottom-left) and $l = 22$ (bottom-right).

Due to the poor structural performances of multi-SIMPOD for atlas $\mathcal{A}_1$, we investigate if a finer sampling of the possible scenarios improves the quality

	CPU time [s]	$\mathcal{G}$	#iterations
multi-SIMP$_{\boldsymbol{\mu}^*}$	172.08	7.4551	249
$l = 3$	8.68	39.4493	15
$l = 4$	19.33	33.7280	33
$l = 5$	13.92	29.4964	23
$l = 13$	26.38	19.9066	39
$l = 22$	21.56	17.9476	34

Table 4.8: multi-SIMPOD cantilever test case for atlas $\mathcal{A}_1$: quantitative data for multi-SIMP$_{\boldsymbol{\mu}^*}$ and multi-SIMP$_{\boldsymbol{\mu}^*,\mathrm{POD}}$ algorithms.

of the prediction by resorting to atlas $\mathcal{A}_2$.

In Figure 4.9, we compare the density distribution provided by multi-SIMPOD for different choices of l with the reference configuration. At least 22 modes are required to identify the final topology, whereas 41 modes deliver a sharp and smooth structure very close to the reference one. Table 4.9 provides a more quantitative assessment. The performances are still not so satisfactory. Indeed, the mismatch between the two configurations in terms of mechanical stiffness is about 100% higher in the multi-SIMPOD case ($l = 41$) with respect to the reference configuration. The gain in terms of computational time is now of a factor about equal to 4. Moreover, it turns out that there are critical configurations where a large number of iterations is demanded, possibly due to the switching of the solution from two different minima of the compliance functional.

	CPU time [s]	$\mathcal{G}$	#iterations
multi-SIMP$_{\boldsymbol{\mu}^*}$	172.08	7.4551	249
$l = 4$	10.12	31.1832	18
$l = 17$	70.05	20.2008	109
$l = 22$	49.93	18.6441	75
$l = 31$	38.96	15.9707	52
$l = 41$	39.73	14.6244	46

Table 4.9: multi-SIMPOD cantilever test case for atlas $\mathcal{A}_2$: quantitative data for multi-SIMP$_{\boldsymbol{\mu}^*}$ and multi-SIMP$_{\boldsymbol{\mu}^*,\mathrm{POD}}$ algorithms.

Moving from the improvements led by the PC-SIMPOD algorithm in Section 4.3.2, we apply the multi-parameter version of such an algorithm

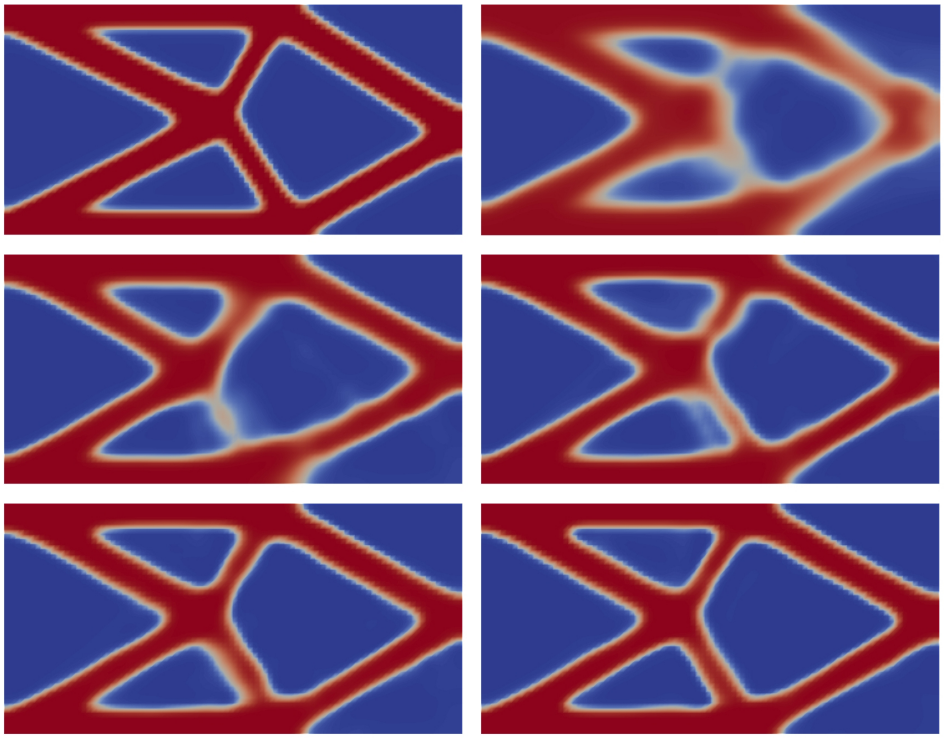

Figure 4.9: multi-SIMPOD cantilever test case for atlas $\mathcal{A}_2$: reference solution (top-left); POD solution for $l = 4$ (top-right), $l = 17$ (center-left), $l = 22$ (center-right), $l = 31$ (bottom-left) and $l = 41$ (bottom-right).

to both atlases. Figure 4.10 compares the reference layout provided by multi-PC-SIMPOD when fed by the output of multi-SIMP$_{\boldsymbol{\mu}^*}$, with the multi-PC-SIMPOD approximation initialized by the structure predicted by multi-SIMPOD algorithm for $l = 4$. There is no striking difference between the two cantilevers, except for a slight discrepancy at the tip, which exhibits a mild bending when starting from the first atlas.

In Table 4.10, we gather the same quantities as in Table 4.6 for $l = 4$ and $l = 22$. These two values for l are the only ones shared by Tables 4.8 and 4.9. Overall, the four configurations do not yield appreciable differences in terms of compliance and of computational time, for the same l. Also the meshes have a similar number of elements as well as maximum aspect ratio. Nevertheless, since the computational gain provided by the choice $l = 4$ is

much higher compared with $l = 22$ (about 3 and 2 times, respectively), we can reasonably assume that the first choice pays off both in terms of accuracy and computational saving.

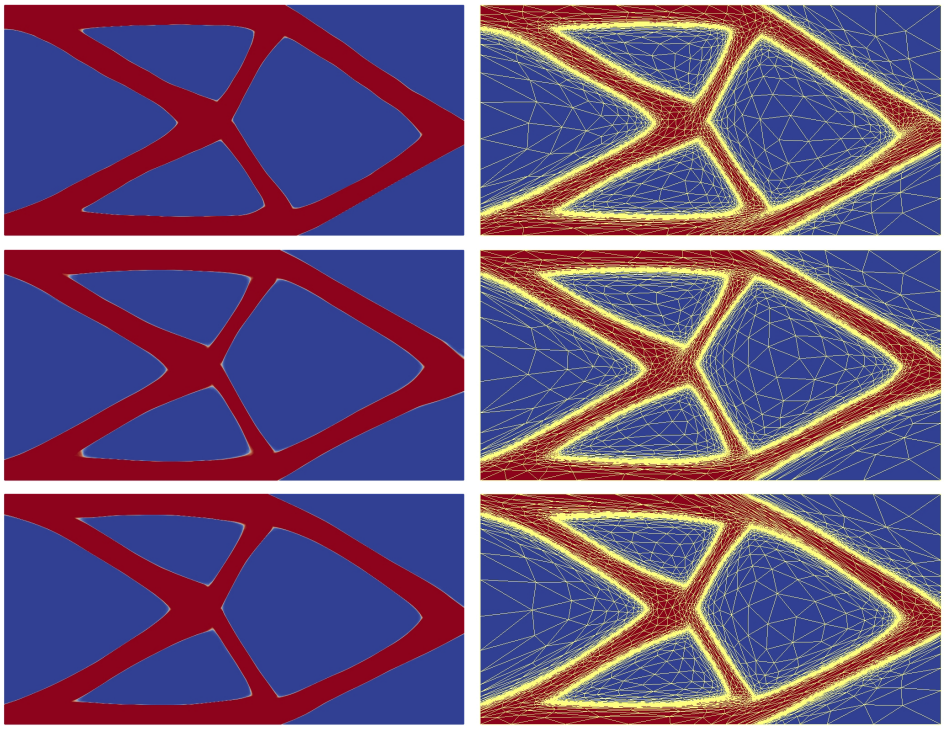

Figure 4.10: multi-PC-SIMPOD cantilever test case: density (left) and density superposed to the mesh (right) when ρ_h^0 =multi-SIMP$_{\boldsymbol{\mu}^*}$ (top), $\rho_h^0 = \rho_{h,POD}^{\boldsymbol{\mu}^*,4}$ for atlas $\mathcal{A}_1$ (center), $\rho_h^0 = \rho_{h,POD}^{\boldsymbol{\mu}^*,4}$ for atlas $\mathcal{A}_2$ (bottom).

		CPU time [s]	$\mathcal{G}$	T_C [s]	$\#\texttt{iter}_C$	$\#\mathcal{T}_h$	$\max_K s_K$
	multi-SIMP$_{\boldsymbol{\mu}^*}$	249.81	7.3418	78.64	105	12770	921.32
$\mathcal{A}_1$	$l = 4$	76.45	7.5701	60.26	85	11146	342.75
	$l = 22$	103.83	7.1408	82.79	110	9178	539.94
$\mathcal{A}_2$	$l = 4$	74.07	7.4773	65.05	90	12068	458.27
	$l = 22$	124.98	7.4173	78.64	105	12914	349.10

Table 4.10: multi-PC-SIMPOD cantilever test case: quantitative data for multi-PC-SIMPOD for different choices of ρ_h^0.

4.5 Conclusions

For the sake of clarity, in Table 4.11 we provide an overview of the methods considered in this paper, by highlighting some of the associated main features, based on the numerical assessment in Sections 4.2.3, 4.3.2, 4.4.1. Namely, we supply a short description of the methods, classified in offline and/or online (`off/on-line`), computationally efficient and/or reliable (E /R) with respect to the standard SIMP algorithm [6, 8, 44], and based on a fixed or adapted (F /A) mesh.

It turns out that three are the methods outperforming the others, namely, SIMPATY and PC-SIMPOD for the single-parameter case, and multi-PC-SIMPOD for the multi-parameter case. Nevertheless, Table 4.11 emphasizes qualitative information only. Thus, to compare more deeply SIMPATY with PC-SIMPOD, we refer to Tables 4.6 and 4.7, while for SIMPATY versus multi-PC-SIMPOD to Table 4.10. In general, it turns out that SIMPATY is slightly more reliable as it provides structures with better mechanical properties, whereas PC-SIMPOD and multi-PC-SIMPOD are more efficient, cutting down the CPU time by a factor 2.

On the contrary, the plain application of POD to SIMP on a fixed mesh leads to very efficient simulations which are, however, not so reliable from the mechanical standpoint. Although there is still some room for improvements by a more careful tuning of filtering and sharpening, we are confident that PC-SIMPOD and multi-PC-SIMPOD methods are the ones to be supported as a robust design tool for structural topology optimization. Moreover, we expect that the advantages observed in the two-dimensional case will be magnified by generalizing these methods to a 3D context, which represents the next step of our research.

4.6 Acknowledgments

The authors acknowledge the research project GNCS-INdAM 2018 “Tecniche di Riduzione di Modello per le Applicazioni Mediche”, which partially supported this research.

		`off/on-line`	E / R	F / A
SIMPATY	SIMP+anisotropic mesh adaption [39, 40]	✗ / ✓	✓ / ✓	✗ / ✓
SIMP_{μ}	SIMP+filtering+sharpening	✓ / ✗	✗ / ✓	✓ / ✗
$\text{SIMP}_{\mu^*,\text{POD}}$	SIMP on the reduced space+sharpening	✗ / ✓	✓ / ✗	✓ / ✗
SIMPOD	SIMP_{μ}+$\text{SIMP}_{\mu^*,\text{POD}}$	✓ / ✓	✓ / ✗	✓ / ✗
PC-SIMPOD	predictor: SIMPOD + corrector: SIMPATY	✗ / ✓	✓ / ✓	✗ / ✓
multi-$\text{SIMP}_{\boldsymbol{\mu}}$	multi-parameter SIMP+filtering+sharpening	✓ / ✗	✗ / ✓	✓ / ✗
multi-$\text{SIMP}_{\boldsymbol{\mu}^*,\text{POD}}$	multi-SIMP on the reduced space+sharpening	✗ / ✓	✓ / ✗	✓ / ✗
multi-SIMPOD	multi-SIMP_{μ}+multi-$\text{SIMP}_{\mu^*,\text{POD}}$	✓ / ✓	✓ / ✗	✓ / ✗
multi-PC-SIMPOD	predictor: multi-SIMPOD + corrector: SIMPATY	✗ / ✓	✓ / ✓	✗ / ✓

Table 4.11: Main features of the methods considered in the paper.

Bibliography

[1] G. Allaire, F. Jouve, and H. Maillot. "Topology optimization for minimum stress design with the homogenization method". In: *Struct. Multidisc. Optim.* 28 (2004), pp. 87–98.

[2] G. Allaire, F. Jouve, and A. Toader. "Structural optimization using sensitivity analysis and level set-method". In: *J. Comput. Phys.* 194 (2004), pp. 363–393.

[3] S. Amstutz. "Connections between topological sensitivity analysis and material interpolation schemes in topology optimization". In: *Struct. Multidiscip. Optim.* 43.6 (2011), pp. 755–765.

[4] M. P. Bendsøe. "Optimal shape design as a material distribution problem". In: *Struct. Optimization* 1.4 (1989), pp. 193–202.

[5] M. P. Bendsøe. *Optimization of Structural Topology, Shape, and Material*. Springer-Verlag, Berlin, 1995, pp. xii+271.

[6] M. P. Bendsøe and N. Kikuchi. "Generating optimal topologies in structural design using a homogeneization method". In: *Comput. Methods Appl. Mech. Eng.* 71.2 (1988), pp. 197–224.

[7] M. P. Bendsøe and O. Sigmund. "Material interpolation schemes in topology optimization". In: *Arch. Appl. Mech.* 69.9 (1999), pp. 635–654.

[8] M. P. Bendsøe and O. Sigmund. *Topology Optimization: Theory, Methods and Applications*. Springer-Verlag, Berlin Heidelberg, 2003.

[9] B. Bourdin and A. Chambolle. "Design-dependent loads in topology optimization". In: *ESAIM Control. Optim. Calc. Var.* 9 (2003), pp. 19–48.

[10] D Brackett, I Ashcroft, and R Hague. "Topology optimization for additive manufacturing". In: *Proceedings of the solid freeform fabrication symposium, Austin, TX*. Vol. 1. S. 2011, pp. 348–362.

[11] M. Burger and S. J. Osher. "A survey on level set methods for inverse problems and optimal design". In: *European J. Appl. Math.* 16.2 (2005), pp. 263–301.

[12] V. J. Challis and J. K. Guest. "Level set topology optimization of fluids in Stokes flow". In: *Int. J. Numer. Meth. Engng* 79.10 (2009), pp. 1284–1308.

[13] P. G. Ciarlet. *The Finite Element Method for Elliptic Problems*. North-Holland Publishing Co., Amsterdam-New York-Oxford, 1978, pp. xix+530.

[14] L. De Lathauwer, B. De Moor, and J. Vandewalle. "A multilinear singular value decomposition". In: *SIAM J. Matrix Anal. Appl.* 21.4 (2000), pp. 1253–1278.

[15] J. D. Deaton and R. V. Grandhi. "A survey of structural and multidisciplinary continuum topology optimization: post 2000". In: *Struct. Multidiscip. Optim.* 49 (2014), pp. 1–38.

[16] L. Dedè, M. J. Borden, and T. J. R. Hughes. "Isogeometric analysis for topology optimization with a phase field model". In: *Arch. Comput. Methods Eng.* 19 (2012), pp. 427–465.

[17] L. Dedè, S. Micheletti, and S. Perotto. "Anisotropic error control for environmental applications". In: *Appl. Numer. Math.* 58.9 (2008), pp. 1320–1339.

[18] A. Díaz and O. Sigmund. "Checkerboard patterns in layout optimization". In: *Struct. Multidiscip. Optim.* 19 (1995), pp. 89–92.

[19] H. Eschenauer and N. Olhoff. "Topology optimization of continuum structures: a review". In: *Appl. Mech. Rev.* 54.4 (2001), pp. 331–390.

[20] N. Ferro, S. Micheletti, and S. Perotto. "A sequential coupling of shape and topology optimization for structural design". Submitted.

[21] L. Formaggia, S. Micheletti, and S. Perotto. "Anisotropic mesh adaption with application to CFD problems". In: *Proceedings of WCCM V, Fifth World Congress on Computational Mechanics*. Ed. by H. Mang, F. Rammerstorfer, and J. Eberhardsteiner. 2002, pp. 1481–1493.

[22] L. Formaggia and S. Perotto. "New anisotropic a priori error estimates". In: *Numer. Math.* 89 (2001), pp. 641–667.

[23] H. Garcke et al. "Numerical approximation of phase field based shape and topology optimization for fluids". In: *SIAM J. Sci. Comput.* 37.4 (2015), A1846–A1871.

[24] P.-L. George and H. Borouchaki. *Delaunay Triangulation and Meshing. Application to Finite Elements*. Editions Hermès, Paris, 1998.

[25] G. H. Golub and C. F. Van Loan. *Matrix computations*. Fourth. Johns Hopkins Studies in the Mathematical Sciences. Johns Hopkins University Press, Baltimore, MD, 2013.

[26] F. de Gournay, G. Allaire, and F. Jouve. "Shape and topology optimization of the robust compliance via the level set method". In: *ESAIM Control Optim. Calc. Var.* 14.1 (2008), pp. 43–70.

[27] J. K Guest, J. H. Prevost, and T. Belytschko. "Achieving minimum length scale in topology optimization using nodal design variables and projection functions". In: *Int. J. Numer. Methods Engng* 61.2 (2004), pp. 238–254.

[28] M. D. Gunzburger. *Perspectives in Flow Control and Optimization*. Vol. 5. Advances in Design and Control. Society for Industrial and Applied Mathematics (SIAM),Philadelphia, PA, 2003.

[29] F. Hecht. "New development in FreeFem++". In: *J. Numer. Math.* 20.3-4 (2012), pp. 251–265.

[30] M. Kahlbacher and S. Volkwein. "Galerkin proper orthogonal decomposition methods for parameter dependent elliptic systems". In: *Discuss. Math. Differ. Incl. Control Optim.* 27.1 (2007), pp. 95–117.

[31] K. Kamalja and N. Khangar. "Singular value decomposition for multidimensional matrices". In: *Int. J. Eng. Res. Appl.* 3.6 (2013), pp. 123–129.

[32] K. Kunisch and S. Volkwein. "Galerkin proper orthogonal decomposition methods for a general equation in fluid dynamics". In: *SIAM J. Numer. Anal.* 40.2 (2002), pp. 492–515.

[33] B. S. Lazarov and O. Sigmund. "Filters in topology optimization based on Helmholtz-type differential equations". In: *Int. J. Numer. Meth. Engng* 86.6 (2011), pp. 765–781.

[34] P. LeGresley and J. Alonso. "Airfoil design optimization using reduced order models based on proper orthogonal decomposition". In: *AIAA Paper* 2000-2545 (2000).

[35] Q. Liang. *Performance-based Optimization of Structures. Theory and Applications*. Spon Press, London, 2005.

[36] S. Micheletti and S. Perotto. "Anisotropic adaptation via a Zienkiewicz-Zhu error estimator for 2D elliptic problems". In: *Numerical Mathematics and Advanced Applications*. Ed. by G. Kreiss et al. Springer-Verlag Berlin Heidelberg. 2010, pp. 645–653.

[37] S. Micheletti and S. Perotto. "Reliability and efficiency of an anisotropic Zienkiewicz-Zhu error estimator". In: *Comput. Methods Appl. Mech. Engrg.* 195.9–12 (2006), pp. 799–835.

[38] S. Micheletti, S. Perotto, and P. E. Farrell. "A recovery-based error estimator for anisotropic mesh adaptation in CFD". In: *Bol. Soc. Esp. Mat. Apl. SeMA* 50 (2010), pp. 115–137.

[39] S. Micheletti, S. Perotto, and L. Soli. *Ottimizzazione topologica adattativa per la fabbricazione stratificata additiva*. Italian patent application No. 102016000118131, filed on November 22, 2016 (extended as *Adaptive topology optimization for additive layer manufacturing*, International patent application PCT No. PCT/IB2017/057323). 2017.

[40] S. Micheletti, S. Perotto, and L. Soli. "Topology optimization driven by anisotropic mesh adaptation: towards free-form design". Submitted.

[41] J. Nocedal and S. J. Wright. *Numerical Optimization*. Springer Series in Operations Research. Springer-Verlag, New York, 1999.

[42] B. Raghavan et al. "A bi-level meta-modeling approach for structural optimization using modified POD bases and Diffuse Approximation". In: *Computers & Structures* 127 (2013), pp. 19 –28.

[43] S. S. Ravindran. "A reduced-order approach for optimal control of fluids using proper orthogonal decomposition". In: *Internat. J. Numer. Methods Fluids* 34.5 (2000), pp. 425–448.

[44] G. I. N. Rozvany. "A critical review of established methods of structural topology optimization". In: *Struct. Multidiscip. Optim.* 37 (2009), pp. 217–237.

[45] E. W. Sachs and S. Volkwein. "POD-Galerkin approximations in PDE-constrained optimization". In: *GAMM-Mitt.* 33.2 (2010), pp. 194–208.

[46] O. Sigmund. "Morphology-based black and white filters for topology optimization". In: *Struct. Multidiscip. Optim.* 33 (2007), pp. 401–424.

[47] O. Sigmund and J. Petersson. "Numerical instabilities in topology optimization: a survey on procedures dealing with checkerboards, mesh-dependencies and local minima". In: *Struct. Optim.* 16.1 (1998), pp. 68–75.

[48] O. Sigmund and K. Maute. "Topology optimization approaches, A comparative review". In: *Struct. Multidiscip. Optim.* 48.6 (2013), pp. 1031–1055.

[49] L. Sirovich. "Turbulence and the dynamics of coherent structures. I. Coherent structures". In: *Quart. Appl. Math.* 45.3 (1987), pp. 561–571.

[50] J. Sokolowski and A. Zochowski. "On the topological derivative in shape optimization". In: *SIAM J. Control. Opt.* 37 (1999), pp. 1251–1272.

[51] A. Wächter and L. T. Biegler. "On the implementation of an interior-point filter line-search algorithm for large-scale nonlinear programming". In: *Math. Program.* 106.1, Ser. A (2006), pp. 25–57.

[52] M. Y Wang, X. Wang, and D. Guo. "A level set method for structural topology optimization". In: *Comput. Methods Appl. Mech. Engrg.* 192.1-2 (2003), pp. 227–246.

[53] M. Y. Wang and S. Zhou. "Phase field: a variational method for structural topology optimization". In: *CMES Comput. Model. Eng. Sci.* 6.6 (2004), pp. 547–566.

[54] K. Willcox and J. Peraire. "Balanced model reduction via the proper orthogonal decomposition". In: *AIAA J.* 40 (2002), pp. 2323–2330.

[55] L. Xia and P. Breitkopf. "A reduced multiscale model for nonlinear structural topology optimization". In: *Comput. Methods Appl. Mech. Engrg.* 280 (2014), pp. 117–134.

[56] Y. Xie and G. Steven. "A simple evolutionary procedure for structural optimization". In: *Comput. Struct.* 49 (1993), pp. 885–896.

[57] K. Yaji et al. “Shape and topology optimization based on the convected level set method”. In: *Struct. Multidiscip. Optim.* 54.3 (2016), pp. 659–672.

[58] G. H. Yoon. “Structural topology optimization for frequency response problem using model reduction schemes”. In: *Comput. Methods Appl. Mech. Engrg.* 199.25-28 (2010), pp. 1744–1763.

[59] O. C. Zienkiewicz and J. Z. Zhu. “A simple error estimator and adaptive procedure for practical engineering analysis”. In: *Int. J. Numer. Meth. Engng* 24 (1987), pp. 337–357.

[60] O. C. Zienkiewicz and J. Z. Zhu. “The superconvergent patch recovery and a posteriori error estimates. I: The recovery technique”. In: *Int. J. Numer. Meth. Engng* 33 (1992), pp. 1331–1364.

[61] O. C. Zienkiewicz and J. Z. Zhu. “The superconvergent patch recovery and a posteriori error estimates. II: Error estimates and adaptivity”. In: *Int. J. Numer. Meth. Engng* 33 (1992), pp. 1365–1382.

Conclusions

In this thesis, the structural optimization problem has been investigated from a methodological and numerical viewpoint, mainly in terms of topology optimization. The standard formulation has been enriched with advanced mathematical procedures. The goal of the proposed methods is twofold. On the one hand, we enhance the mechanical performances of given structures by means of shape and topology optimization. On the other hand, we improve the standard SIMP method for topology optimization by resorting to anisotropic mesh adaptation and the POD model order reduction technique.

In Chapter 2, the mechanical performance, represented by the static compliance, has been improved by proposing a sequential coupling between shape and topology optimization. The results highlight that the structure predicted by the coupled shape-topology optimization algorithm is lighter compared with the result of the shape optimization only, as well as stiffer than the layout provided by the single topology optimization. The additional benefit due to anisotropic mesh adaptation is the creation of very smooth structures characterized by sharp solid/void interfaces. This makes the new designs almost ready to be 3D-printed.

Chapter 3 concerns the application of SIMPATY algorithm to the design of metamaterials. The mathematical framework is the inverse homogenization theory and the objective is to devise new micro-cells ensuring desired mechanical properties at the macro-scale. The proposed method delivers innovative cell designs as well as standard micro-cells as present in the literature. In all cases, the micro-cells have sharp contours and exhibit the desired effective macroscale properties.

Chapter 4 is focused on the reduction of the computational burden involved in topology optimization. For this goal, we adopted a POD approach, properly intertwined with SIMPATY algorithm. The main idea is to use the POD prediction as the initial guess for SIMP enriched with anisotropic mesh

adaptation, in the spirit of a predictor/corrector method. This idea considerably reduced the number of iterations for SIMPATY to converge also ensuring similar mechanical performances.

Concerning possible future developments for this work, we list the application of the advanced techniques proposed in this thesis to real-life problems, such as the design of satellite components or prosthetic devices, and the design of new metamaterials enjoying both mechanical and thermal properties. For instance, we aim at enhancing catalytic capabilities for strongly exothermic chemical processes. From a modeling viewpoint, an extension of the presented algorithms to a more general framework characterized by uncertainty is mandatory with a view to complex applications. We also plan to enrich the formulation of the topology optimization problem with design constraints, to include the manufacturing phase. For instance, in a 3D printing-based design, it is highly desirable to identify the best orientation of the printing plate or the optimal location of the overhangs. Multi-objective topology optimization and a comparison between the SIMP approach and the level-set method represent another possible issue for future investigations. Finally, we are interested in incorporating the new techniques here proposed in a commercial software for topology optimization.